MECHANICAL CHARACTERIZATION OF CELLS AND TISSUES BY SCANNING ACOUSTIC MICROSCOPY AND OPTICAL TWEEZERS

by

İrem Demirkan

B.S., Physics, Kocaeli University, 2009

M.S., Biomedical Engineering, Boğaziçi University, 2012

Submitted to the Institute for Graduate Studies in
Science and Engineering in partial fulfillment of
the requirements for the degree of
Doctor of Philosophy

Graduate Program in Physics

Boğaziçi University

2020

ACKNOWLEDGEMENTS

Undertaking this Ph.D. has been a truly life-changing experience for me. It is the output of the effort and support of many people to whom I would like to thank.

In the beginning, I would like to thank to my advisor Prof. Mehmet Burçin Ünlü. He has always inspired me to become an independent researcher. He is my mentor and a better advisor beyond the imagination.

Apart from my advisor, I would like to thank to the rest of my thesis committee: Prof Özhan Özatay, Assoc. Prof. Özgür Özdemir, Assist. Prof. Hakan Erkol and Assist. Prof. Murat Tümer, for giving the encouragement and sharing insightful suggestions, contributing to my graduation.

I would like to thank to Istanbul Oncology Hospital, Kartal Doctor Lütfi Kırdar Education and Research Hospital, Ministry of Health and Yeditepe University Faculty of Dentistry Hard Tissue Laboratory for the assistance they all provided. Special thanks to Dr. Cemile Ceylan, Dr. Alper Kiraz, Dr. Gökhan Yaprak, Dr. Ceyda Özçakır and İsmehan Dere who have always been so helpful throughout my dissertation.

I also acknowledge the funding support that made my Ph.D. research possible. I was funded by the Ministry of Development (Project No: 2009K120520), TUBITAK (Project No: 113F047) and Bogazici University Research Fund (Project Number: 11461).

I would like to thank all members of Medical and Biological Physics Laboratory for providing me with a friendly and inspiring environment to work and have fun over many years. Special thanks to Şirin Yonucu, Tuna İnanç, Defne Yılmaz, Mert Tüzer, Melita Parlak and Bükem Tanören.

I would like to say a heartfelt thank to my wonderful dad and beautiful mum for always believing in me and giving me the opportunities and experiences that have made me who I am.

ABSTRACT

MECHANICAL CHARACTERIZATION OF CELLS AND TISSUES BY SCANNING ACOUSTIC MICROSCOPY AND OPTICAL TWEEZERS

Cell and tissue mechanics has a vital role in several pathological and physiological processes. Mechanical perturbations produce numerous biological processes within a cell or a tissue, which can result in mechanical changes. Thus, examination of the underlying mechanical characteristics of biological surroundings is a promising and important research area for the diagnosis and prognosis of diseases, especially in cancer. To delve into this, we first proposed the application of Scanning Acoustic Microscopy (SAM) for monitoring diffusion of sodium ion, which is known to regulate bodily functions and biological processes, by time-dependent acoustic impedance measurements on the soft tissue-mimicking agarose phantom. We established a linear correlation between the alterations in the phantom concentration and its acoustic impedance distribution. The second question in this thesis was to whether establish a correlation between cumulative irradiation doses and the mechanical properties of the human teeth or not. Here, 320 MHz SAM in micrometer resolution was used to characterize the acousto-mechanical effects on human teeth after radiation therapy application, which is applied to cure head and neck cancer patients. Apart from SAM, this thesis introduces a dual-beam optical tweezers study for the quantification of red blood cell deformability as a determinant factor to assess cell reactions to radiotherapy on the cell cortex level. These two imaging techniques were used to understand the mechanical variations in response to exterior stimuli in biological matter. For each experiment, this thesis revealed the advantages and disadvantages of these methods and the reasons behind the findings from the physical and biological points of view.

ÖZET

TARAMALI AKUSTİK MİKROSKOP VE OPTİK CIMBIZ İLE HÜCRELERİN VE DOKULARIN MEKANİK KARAKTERİZASYONU

Hücre ve doku mekaniği çeşitli patolojik ve fizyolojik süreçlerde hayati bir role sahiptir. Mekanik pertürbasyonlar hücre veya doku içinde sayısız biyolojik süreç üretir ve bu da mekanik değişikliklere neden olabilir. Bu nedenle biyolojik çevrenin altında yatan mekanik özelliklerin incelenmesi, özellikle kanserde hastalıkların tanı ve prognozu için umut verici ve önemli bir araştırma alanıdır. Bunu araştırmak için, ilk olarak, vücut fonksiyonlarını ve biyolojik süreçleri düzenlediği bilinen sodyum iyonunun difüzyonunu izlemek için yumuşak dokuyu taklit eden agaroz fantomunda zamana bağlı akustik empedans ölçümü ile Taramalı Akustik Mikroskopi (TAM) uygulamasını önerdik. Fantom konsantrasyonundaki değişiklikler ile akustik empedans dağılımında doğrusal bir korelasyon oluşturduk. Bu tezdeki ikinci soru, kümülatif ışınlama dozları ile insan dişlerinin mekanik özellikleri arasında bir korelasyon olup olmayacağı idi. Burada, kafa ve boyun kanseri hastalarını tedavi etmek için uygulanan radyasyon tedavisi uygulamasından sonra insan dişleri üzerinde akustik-mekanik etkileri karakterize etmek için mikrometre çözünürlüğünde 320 MHz TAM kullanıldı. TAM dışında, tez, hücre korteks seviyesinde radyoterapiye hücre reaksiyonlarını değerlendirmek için belirleyici bir faktör olarak kırmızı kan hücresi deforme edilebilirliğinin ölçülmesi için çift ışınlı bir optik cımbız çalışması sunar. Bu iki görüntüleme tekniği, biyolojik maddede dış uyaranlara yanıt olarak mekanik varyasyonları anlamak için kullanılmıştır. Her deney için bu tez, bu yöntemlerin avantajları ve dezavantajları ile birlikte fiziksel ve biyolojik açıdan bulguların ardındaki nedenleri ortaya koymuştur.

TABLE OF CONTENTS

ACKNOWLEDGEMENTS i
ABSTRACT iii
ÖZET iv
LIST OF FIGURES viii
LIST OF TABLES xiv
LIST OF SYMBOLS xv
LIST OF ACRONYMS/ABBREVIATIONS xx
1. INTRODUCTION 1
1.1. Cell and Tissue Mechanics 1
1.2. Ultrasound Imaging 6
1.2.1. Sound Propagation 10
1.2.2. Reflection and Transmission 12
1.2.3. Absorption and Attenuation 14
1.2.4. Scattering 16
1.3. Scanning Acoustic Microscopy 18
1.3.1. Boundary Conditions at Liquid-Solid and Solid-Solid Interfaces 19
1.3.2. Acoustic Impedance Measurement Mode 26
1.3.3. Sound Speed Measurement Mode 29
1.3.4. 80 MHz and 320 MHz Ultrasonic Transducers 32
1.3.5. Beam Profile for a Single-Element Ultrasonic Transducer 34
1.3.6. Resolution In Ultrasound Images 36
1.4. Physics of Optical Tweezers 38
1.4.1. Ray Optics Regime ($r \gg \lambda$) 40
1.4.2. Rayleigh Regime ($r \ll \lambda$) 41
1.4.3. Dual-Beam Optical Tweezers 42
1.5. Cancer Treatment 42
1.5.1. Ionizing Radiation Interaction With Biological Medium 44
2. ULTRA-HIGH FREQUENCY ACOUSTIC IMAGING OF SODIUM ION DIF-

FUSION 46
2.1. Introduction 46
2.2. Methodology and Analysis 47
2.2.1. Phantom Design and Sample Preparation 47
2.2.2. Theory of Diffusion Process 50
2.2.3. Scanning Acoustic Microscopy 51
2.2.4. Theory of Acoustic Impedance Measurement Mode 54
2.3. Results 56
2.4. Discussion 62
3. ACOUSTIC DIAGNOSIS OF RADIOTHERAPY-INDUCED EFFECTS ON ELASTICITY OF HUMAN TEETH 69
3.1. Introduction 69
3.2. Methodology 70
3.2.1. Tissue Selection and Preparation 70
3.2.2. Irradiation Design 71
3.2.3. Scanning Electron Microscopy (SEM) Analysis 72
3.2.4. Statistical Analysis 73
3.2.5. Ultrasound Data Acquisition by 320MHz SAM and Analysis . . 73
3.3. Results 76
3.3.1. Acoustic Impedance Imaging 76
3.3.2. Scanning Electron Microscopy 81
3.4. Discussion 81
4. QUANTIFYING THE INFLUENCES OF RADIOTHERAPY ON DEFORMABILITY OF HUMAN ERYTHROCYTES BY DUAL-BEAM OPTICAL TWEEZERS 86
4.1. Radiotherapy Treatment and Red Blood Cells 86
4.2. Methods 88
4.2.1. Sample Preparation 90
4.2.2. Irradiation Protocol 90
4.3. Results 91
4.4. Discussion 99

5. CONCLUSION 103
REFERENCES 105

LIST OF FIGURES

Figure 1.1. Cell mechanical architecture consisting of microtubules, the intermediate filaments and the actin filaments (F-actin). Also, the cell mechanics is determined by its cell border (or cell membrane), nucleus and cytoplasm (a colloidal liquid-like region between cell membrane and nucleus). 3

Figure 1.2. Schematic classification of experimental instruments commonly used for mechanical characterization at the cell and tissue levels 4

Figure 1.3. Characteristics of ultrasound waves 7

Figure 1.4. Frequency range of ultrasound and its applications 8

Figure 1.5. When medium 1 and medium 2 have the same acoustic impedance, their interface line will not create a reflection. A weak reflection is obtained when the difference in acoustic impedance is small. A strong reflection is produced when the difference is large. All the ultrasound is totally reflected from the interface line when the difference is considerably large. 12

Figure 1.6. Schematic description of incident, reflection and refraction of ultrasound waves at target boundaries having different acoustic impedance values, Z_1 and Z_2. (a) 90 C° vertical incidence of sound wave, (b) non-vertical incidence ($c_1<c_2$, (c) non-vertical incidence $c_1>c_2$. . . 13

Figure 1.7. Attenuation relation with the type of tissues and ultrasonic frequency 15

Figure 1.8. Wave propagation direction for liquid-solid interface. 22

Figure 1.9. Wave propagation direction for solid-solid interface. 24

Figure 1.10. Signals in acoustic impedance measurement configuration. 26

Figure 1.11. The top side (A): Ultrasound wave traveling in multi-layer media: water, substrate and target, respectively. Blue and yellow arrows illustrate traveling of longitudinal and generated shear waves, respectively. The bottom side (B): Waveform and reflection path of waves from the boundary lines resulted from water-substrate and substrate-target 27

Figure 1.12. Signals in sound speed measurement configuration 30

Figure 1.13. 80 MHz ultrasonic transducer and its design with polyvinylidene fluoride (PVDF) thin film, (b) 320 MHz ultrasonic transducer and its design with piezoelectric polymer 34

Figure 1.14. Schematic of near field and far field of the beam pattern formation of (A) high frequency and (B) low frequency ultrasound transducer. (C) Focusing of ultrasound transducer narrows beam width 35

Figure 1.15. Illustration of ultrasound resolution types for a traveling ultrasound wave. 36

Figure 1.16. Illustration of gradient and scattering forces. (a) Axial and (b) Lateral displacements of the particle resulted from the gradient force on it. Intensity of the rays is indicated by different thicknesses. 39

Figure 1.17. An illustration of multidisciplinary cancer treatments that the cancer patients receive during disease management 43

Figure 1.18. The event sequences after radiotherapy exposure in humans can result in multiple reactions in a short or a long term duration . . . 45

Figure 2.1. (a) Lateral and (b) top perspectives of agarose phantom of diameter 4 cm, (c) lateral and (d) top perspectives of agarose phantom of diameter 8 cm. The concentric wells of NaCl solutions are 7 mm (a) and 14 mm (c). 49

Figure 2.2. Scanning acoustic microscopy system in our laboratory. (a) Top view of the agarose phantom and the well used for monitoring NaCl diffusion, (b) 80 MHz transducer (PVDF-TrFE), (c) X-Y stage and (d) computer display. 52

Figure 2.3. Schematic diagram of SAM consisting of five parts: Transducer, X-Y scanning machine, signal processor, digitizer and display unit for monitoring. (a) Acoustic Impedance measurement mode and (b) Sound Speed measurement Mode. 53

Figure 2.4. Illustration of acoustic impedance measurement mode. S_0 is the transmitted signal, S_{object} is the signal reflected from the object, $S_{reference}$ is the signal reflected from the reference and Z_{object}, $Z_{substrate}$, $Z_{reference}$ are the acoustic impedances of the object, substrate and reference, respectively 55

Figure 2.5. Acoustic impedance values of NaCl solutions as a function of sodium content. 57

Figure 2.6. Successively obtained acoustic impedance maps of the 2% agarose phantom with diffusing NaCl solutions of concentrations of (a) 1%, (b) 1.5% and (c) 2%, in 14 minutes. The field of view was adjusted to 4.8 mm × 4.8 mm, covered by 300 × 300 pixels. 59

Figure 2.7. Subsequent images of acoustic impedance maps of the 2% agarose phantom with diffusing 10% NaCl solution. The field of view for each image was adjusted to 4.8 mm × 4.8 mm, covered by 300 × 300 pixels. 59

Figure 2.8. Comparison of changes in acoustic impedance values of the 2% phantom resulting from 10% NaCl solution diffusion for selected time points. Initial data points correspond to the acoustic impedance values at the well-phantom border. Acoustic impedance values inside the well, at the well-phantom border and within the phantom are demonstrated in figure inset. 61

Figure 2.9. Decay trends of the maximum acoustic impedance values for 10% NaCl diffusion in the 2% agarose phantom. Experimentally obtained values illustrated by the green squares were fitted to Equation 2.5 producing solid line. 61

Figure 3.1. Details of the irradiation procedure for the polystyrene petri dish located within the rice phantom. 72

Figure 3.2. (A) Scanning Acoustic Microscopy (SAM) System (B) Schematic representation of tissue sectioning (cutting points from enamel and longutidunal direction) and localization for the measurement. (C) Schematic representation of acoustic impedance measurement mode. In this case, water is used as substrate. Tooth sample is not necessarily thin sliced. Just front surface must be polished to be very flat for the acoustic impedance measurement of the tooth sample . 75

Figure 3.3. Two-dimensional acoustic impedance images of human tooth pre- and post-radiation therapy application recorded by 320 MHz Scanning Acoustic Microscopy. The resolution was defined through the field of view of 4.8 mm × 4.8 mm for each image with a 300 × 300 scanning points with a scan size of 16 μm. All image were determined to visualize both enamel and dentin within a signal scan. Gradation in color bar (red to yellow) represent the variation after subjection to radiation doses which are clinically used to cure head and neck cancers. Sound dentin shows up higher acoustic impedance (orange to yellow) than the softened dentin through radiotherapy. 77

Figure 3.4. Distribution of acoustic impedance values for enamel (A) and dentin (B) for non-irradiated and irradiated groups (control, 2 Gy, 8 Gy, 20 Gy, 30 Gy and 60 Gy). Stars above the scatter plots show a statistically significant difference in mean acoustic impedance relative to non-irradiated group (*) ($p < 0.05$). 79

Figure 3.5. Electron micrographs of the enamel and dentin of the human molar teeth. The images were obtained by Scanning Electron Microscopy (SEM) at 50000x. Left-hand side images represent enamel, while right-hand side show dentin. (A) No irradiation (B) 2 Gy, (C) 8 Gy, (D) 20 Gy, (E) 30 Gy and (F) 60 Gy, respectively. 82

Figure 4.1. (A) Dual-beam Optical Tweezers Set-up used to quantify deformability of red blood cells (RBCs) after radiotherapy treatment, (B) Initial positioning of the traps on a RBC in stretching mode. . . . 89

Figure 4.2. Blood sample + Bovine serum albumin (BSA) + Phosphate-buffered saline (PBS) solution on a glass slide with a well at the center. . . 90

Figure 4.3. Stretching of a RBC by dual-optical traps, (A) The traps were positioned on the two ends of the RBC with the trap separation of 5μm, corresponding the starting point of the stretching, (B) Just before escaping from one of the traps, RBC was reached to the maximum length, showing the peak of the Maximum Feret Diameter (MFD) vs time graph, (C) Contracted RBC after escaping from the traps. 92

Figure 4.4. (A) Change in the mean DI of the control group with respect to the laser trap power operating at 40%, 60%, 80% and 100%, (B) The scatter plot of DI vs. unstretched RBC size with the corresponding linear fit lines are presented for the four data groups. R-squared values of the linear fit lines: 0.170, 0.235, 0.167, 0.344 for the data sets of 0 Gy, 2Gy, 12 Gy, 25 Gy, respectively. 93

Figure 4.5. Kernel density estimations for pairs of initial and final RBC lengths in the control group, 2 Gy, 12 Gy and 25 Gy groups. 94

Figure 4.6. (A) The box plot shows the summary of the four data sets. The gray dots show the data points, and the gray line in the boxes show the mean values of the corresponding data sets, respectively. (B) Kernel density estimations (kernel=normal) for deformability index are demonstrated for each dose groups. Kernel bandwidths were found as: 0.0362, 0.0278, 0.0379, 0.0518 for the groups 0 Gy, 2 Gy, 12 Gy, 25 Gy, respectively. 96

Figure 4.7. Morphology of red blood cell sample for non-irradiated and irradiated experimental groups at 2 Gy, 12 Gy and 25 Gy, respectively. Yellow arrows indicate morphologically differentiated red blood cells after radiotherapy exposure. 98

LIST OF TABLES

Table 1.1. Properties of 80 MHz and 320 MHz single-element transducers . . 33

Table 3.1. Mean and Standard Deviation of recorded acoustic impedance values for each region and irradiation dose obtained by 320 MHz Scanning Acoustic Microscopy (SAM). The statistically different groups were marked with the stars ($p < .05$.) 78

Table 4.1. Comparisons of the control group and experimental groups in accordance with the one-way ANOVA and Dunnett's test. A $p < 0.05$ value was considered statistically different. ns shows no significant difference among groups. 95

Table 4.2. Number of the RBCs, mean of L_0, L_{max} and DI values for each data set. 95

Table 4.3. Whole blood count comparisons between the non-irradiated group and irradiated groups at 2 Gy, 12 Gy and 25 Gy. WBC: White Blood Cell, RBC: Red Blood Cell, HCT: Hematocrit, MCH: Mean Corpuscular Hemoglobin, RDW: Red Cell Distribution Width, MCHC: Mean Cell Hemoglobin Concentration, MCV: Mean Cell Volume, PLT: Platelet, RDW-CV: Red Blood Cell Distribution Width. . . . 97

LIST OF SYMBOLS

a	Disc radius
a_{sc}	Scatterer source size
A	Reflection coefficient
A_I	Incident pressure wave magnitude
A_r	Amplitude reflected from the reference
A_R	Pressure amplitude reflection coefficient
A_s	Amplitude reflected from the target
A_{SI}	Shear wave incidence
A_{SR}	Shear wave reflection
A_{TR}	Shear wave transmittion
A_T	Pressure amplitude transmission coefficient
b_γ	Correlation coefficient
c	Sound speed
C	Concentration
c_0	Sound speed of the coupling liquid
C_e	Elasticity coefficient
C_i	Initial concentration of the disc
c_1	Sound speed in medium-1
c_2	Sound speed in medium-2
c_{L1}	Sound speed of pressure wave in medium-1
c_{L2}	Sound speed of pressure wave in medium-2
c_p	Heat capacity at a constant volume
c_{S1}	Sound speed of shear wave in medium-1
c_{S2}	Sound speed of shear wave in medium-2
c_v	Heat capacity at a constant volume
d	Thickness of the target
D	Diffusion coefficient
D_a	Aperture diameter

E	Elastic modulus
$\boldsymbol{E}$	Electrical field
E_1	Elastic modulus of medium-1
E_2	Elastic modulus of medium-2
f	Frequency
$\boldsymbol{F}$	Diffusive flux
f_0	Focal length
$F_{gradient}$	Gradient force
$F_{scattering}$	Scattering force
I	Time-averaged incident intensity
I_i	Incident intensity
I_r	Reflected intensity
k	Wave number
$\boldsymbol{K}$	Variation in wave number
k_0	Wave number in liquid
k_1	Wave number in medium-1
k_2	Wave number in medium-2
k_{L1}	Wave number of pressure wave for solid medium-1
k_{L2}	Wave number of pressure wave for solid medium-2
k_{S1}	Wave number of shear wave for solid medium-1
k_{S2}	Wave number of shear wave for solid medium-2
L	Compressional wave
L_0	Initial length of red blood cells
L_{max}	Final length of red blood cells
m	Ratio of refractive indices of particle to medium
n	Number density of scatterers
n_m	Refractive index of surrounding medium
P	Power of incident light
r	Particle diameter
R_{axial}	Axial resolution
R_I	Ratio of reflected intensity to the incident intensity

R_L	Reflection coefficient of pressure wave
$R_{lateral}$	Lateral resolution
S	Shear wave
S_0	Transmitted signal from transducer
$S_{reference}$	Reflected signal from reference
S_{sc}	Time-averaged scattered ultrasound power by the target
S_{target}	Reflected signal from target
T_I	Ratio of transmitted intensity to the incident intensity
T_L	Transmission coefficient of pressure wave
T_L	Transmission coefficient of shear wave
v	Sound velocity
V	Volume of the scatterer
v_I	Velocity of incident sound wave
v_I	Velocity of transmitted sound wave
Z	Acoustic impedance
Z_1	Acoustic impedance of medium-1
Z_2	Acoustic impedance of medium-2
Z_L	Acoustic impedance in liquid medium for pressure wave
$Z_{reference}$	Acoustic impedance of reference
Z_S	Acoustic impedance in solid medium for shear wave
Z_{s_a}	Measured acoustic impedance of the target
Z_{s_t}	Real acoustic impedance of the target
$Z_{substrate}$	Acoustic impedance of substrate
Z_t	Acoustic impedance of tooth
Z_{target}	Acoustic impedance of tooth
Z_w	Acoustic impedance of water
α	Pressure wave incidence angle
β	Pressure wave reflection angle
β_a	Attenuation
ϵ_0	Vacuum dielectric constant

η	Pressure wave transmission angle
η^v	Volumetric viscosity
η_{visc}	Shear viscosity
γ	Shear wave incidence angle
γ_a	Polystyrene attenuation
κ_0	Surrounding medium comressibility
κ_1	Scatterer compressibility
λ	Wavelength
μ	Shear modulus
μ_1	Shear modulus for solid medium-1
μ_2	Shear modulus for solid medium-2
ω	Angular frequency
Ω	Solid angle
ϕ	Plane wave
ϕ_I	Incident pressure wave from a solid onto a solid
ϕ_L	Sound potential for incident pressure wave
$\phi_{\max}$	Phase angle for the maximum point in the normalized intensity spectrum
$\phi_{\min}$	Phase angle for the minimum point in the normalized intensity spectrum
ϕ_R	Reflected pressure wave from a solid onto a solid
ϕ_S	Sound potential for shear wave
ϕ_{SI}	Sound potential for incident shear wave in solid-solid media
ϕ_{SR}	Sound potential for reflected shear wave in solid-solid media
ϕ_{ST}	Sound potential for transmitted shear wave in solid-solid media
ϕ_T	Sound potential for transmitted pressure wave in solid-solid media
ρ	Medium density
ρ_0	Surrounding medium density
ρ_1	Solid medium-1 density
ρ_2	Solid medium-2 density

ρ_{sc}	Scatterer density
σ	Differential scattering cross-section
σ_d	Differential scattering cross-section in inhomogeneous matter
σ_{st}	Stress distortion
τ	Heat conduction
θ	Spherical coordinate angle
θ_a	Half-aperture angle
θ_I	Incidence angle
θ_L	Transmission angle for pressure wave
θ_R	Reflection angle
θ_S	Transmission angle for shear wave
θ_T	Transmission angle
φ	Shear wave transmission angle
φ_{sp}	Spherical coordinate angle
ξ	Shear wave reflection angle

LIST OF ACRONYMS/ABBREVIATIONS

2D	Two Dimensional
3D	Three Dimensional
AFM	Atomic Force Microscopy
AP	Anterior Posterior
B-MODE	Brightness Mode
BSA	Bovine Serum Albumin
C	Compression
CT	Computed Tomography
dB	Decibel
DI	Deformability Index
DNA	Deoxyribonucleic Acid
DRR	Digital Reconstructed Radiography
ECM	Extracellular Matrix
EDTA	Ethylene Diamine Tetra Acetic Acid
F-Actin	Actin Filaments
FOV	Field Of View
GHz	Gigahertz
GTV	Gross Tumor Volume
HCT	Hematocrit
HGB	Hemoglobin
KV	Kilo Voltage
LINAC	Linear Accelerator
ISE	Ion-selective electrode
MCH	Mean Corpuscular Hemoglobin
MCHC	Mean Corpuscular Hemoglobin Concentration
MCV	Mean Corpuscular Volume
MFD	Maximum Feret Diameter
MHz	Megahertz

MMP	Matrix metalloproteinase
MREIT	Magnetic Resonance Electrical Impedance Tomography
MRI	Magnetic Resonance Imaging
MS	Multiple Sclerosis
MU	Motor Unit
NaCl	Sodium Chloride
NDE	Non-destructive Evaluation
PA	Posterior Anterior
PET	Positron Emission Tomography
R	Rarefaction
P	Pressure
PBS	Phosphate-buffered Saline
PLT	Platelet
PVDF	Polyvinylidene Fluoride
PVDF-TrFE	Polyvinylidene Fluoride-Trifluoroethylene
RBC	Red Blood Cell
RDW-SD	Red Blood Cell Distribution Width
RF	Radio-frequency
SAM	Scanning Acoustic Microscopy
SD	Standard Deviation
SEM	Scanning Electron Microscopy
TPS	Treatment Planning System
WBC	White Blood Cell
ZnO	Zinc Oxide

1. INTRODUCTION

1.1. Cell and Tissue Mechanics

A living-cell is a complex biological machine, which can sense and respond to external stimuli resulted from its exterior through triggering mechanical responses consisting of cell differentiation, growth, proliferation, motility, adhesion and apoptosis along with architecture development and cytoplasm dynamics [1–5]. Cells and tissues become reactive when exposed to physical forces by regulating their shape, behavior, and function. This interactive ability of cells is critical for keeping homeostasis of tissues during embryonic development and health. Many normal and abnormal states of cells, tissues and organs are thus influenced by how they mechanically communicate with the surrounding. On the one hand, much of our knowledge about them is biochemical. On the other hand, cell mechanics is of primary importance in controlling a broad range of biological processes on cell and tissue levels [6]. Hence, apart from biochemical investigations, the interpretation of how mechanical characteristics have an impact on the function and behavior of cells and tissues concerning their environment in normal and in abnormal states plays a key role. This necessitates a thorough understanding of physical forces, elasticity or stiffness feature existing within and on the cortex of the cells from micro to the nanoscale [7, 8]. The underlying mechanical characteristics of cells and tissues monitor the regular and unusual health conditions of living-beings, and have been considered to be markers for early identification of diseases. Any alterations in the mechanical characteristics can lead to a disruption in normal physiological functions of cells and tissues (e.g. reorganization of the cytoskeleton), and hence develop diseases such as cancer, heart dysfunction, inflammation and so on [9–13]. Accordingly, the underlying mechanical characteristics of biological matter have originated as a potential way to characterize and identify the diseases. This has led to an introduction of a new research focus, which combines cell biology and mechanics [14]. This focus enables scientists to understand further both how cellular structures develop and how cells communicate with their exterior.

Cell and tissue responses to external inputs can be viscous, elastic, or viscoelastic, along with active or passive. Representative mechanical properties are stretchiness (elasticity), viscoelasticity (viscous dissipation), stiffness and adhesion. Above all, elasticity and stiffness have essential roles in cellular functions [15]. Elasticity is the property of a material to resist deformation caused by an applied force and then return to its original shape after force removal. Stiffness is the extent of a material's rigidity to the external force, that based upon the shape, material mass and the diameter [16,17]. In the human body, mechanical features vary remarkably between organs and tissues, which is quantified on the order of from kPa to GPa (i.e. breast tissue, teeth and bone).

Structural organization of cell interior preserves the mechanical characteristics and integrity of the cell such as cytoskeleton [18]. From the physics point of view, the cell can be considered as a biological machine comprising inhomogeneous materials that accord with the cytoskeleton, nucleus, and other constituents. In the mechanical architecture of the majority of the cells, microtubules, actin filaments (F-actin) and intermediate filaments are the major components of the cytoskeleton, reinforcing the interior of the cell with structure and shape, see Figure 1.1 (Created with BioRender). They are all rigid, and they can vary markedly in the degree of their stiffness. The interior compartment is filled with a vast amount of membrane structures and liquid-like environment, cytoplasm. Elements of cytoskeleton have interactions with organelles and membranes. The cytoskeletal components together with cytoplasmic constituents reflect the viscoelasticity of the cells [19]. Also, the cytoskeleton has a key role in cell movement, intracellular and extracellular transportation, cell division and other physiological processes [3].

Actin filaments are the most prominent cytoskeletal filaments. They can resist both tensile and compressive forces. Through elongating or depolymerizing, actin filaments are able to produce force. Actin polymerization and depolymerization processes also make the cell reactive to external stimuli [20]. Actin-myosin perturbation and damage in cytoskeletal meshwork can be visualized as the stiffness of cells that has a

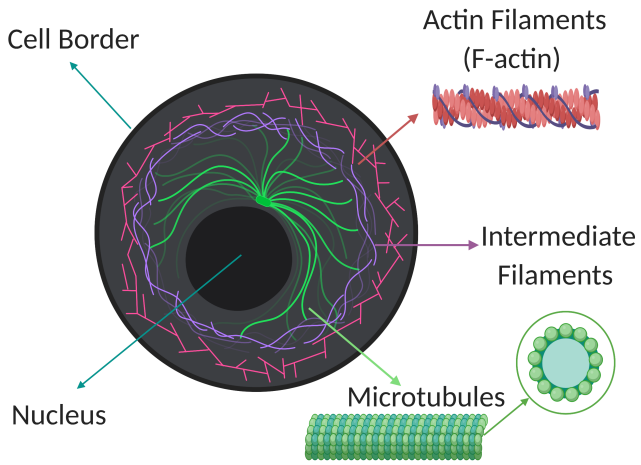


Figure 1.1. Cell mechanical architecture consisting of microtubules, the intermediate filaments and the actin filaments (F-actin). Also, the cell mechanics is determined by its cell border (or cell membrane), nucleus and cytoplasm (a colloidal liquid-like region between cell membrane and nucleus).

key role in cellular functions, and is an extensively quantified mechanical parameter for quantification of cell viscoelasticity.

Diagnosis and/or prognosis of cancer is one of the most important study areas of cell mechanics concerned with determining the intrinsic and extrinsic mechanical properties of cells. The tools developed to measure biomechanical properties of cells and tissues have showed that alterations in cell mechanics are indicators of cancer since a high elasticity may differentiate cancer cells from non-cancerous cells [11, 13]. Intrinsic and extrinsic mechanical responses of cells and tissues to exterior inputs have largely been investigated by four unique methods: optical tweezers, magnetic tweezers, acoustic tweezers and atomic force microscopy (AFM), as shown in Figure 1.2 [18, 21–23]:

AFM uses a tiny cantilever tip application to create a deformation in the cell among the currently used tools to quantify the biomechanical characteristics of biolog-

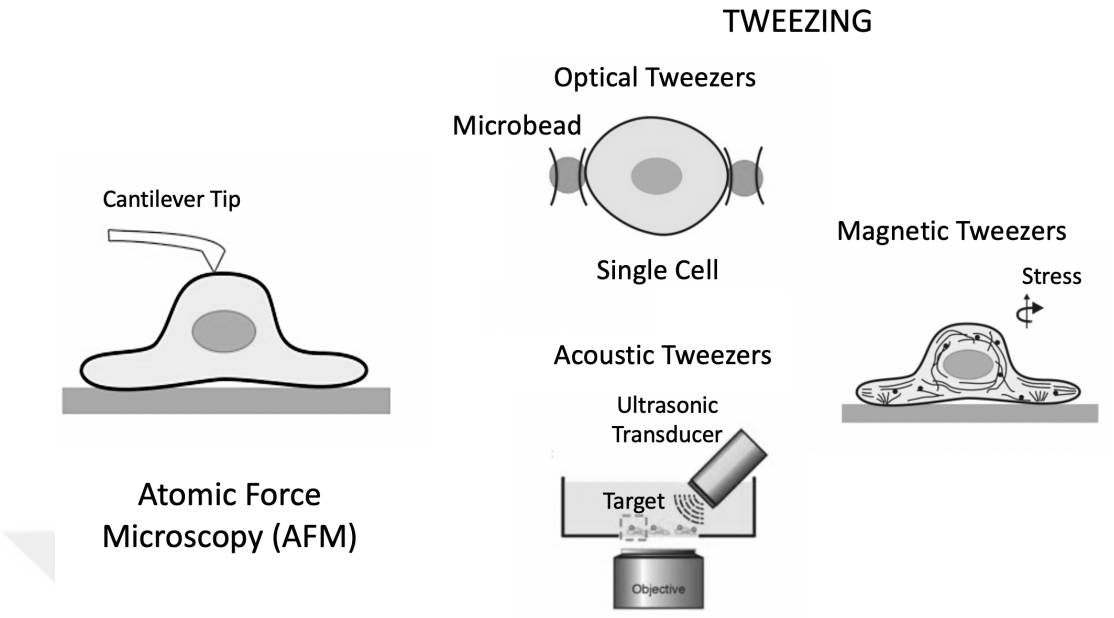


Figure 1.2. Schematic classification of experimental instruments commonly used for mechanical characterization at the cell and tissue levels [3, 24].

ical media. Local mechanical and adhesive characteristics can be scanned along the surface of the single cells by extracting the deflection of the cantilever tip. AFM offers nanometer resolution, which is greater than any light microscope resolution, by a typical force range varying from piconewton (pN) to nanonewton (nN). This force range matches the pathophysiological stiffness range of biological samples. AFM is capable of operating in a liquid-like environment. It also can propose a visualization of biological samples in a real-time manner. However, direct interaction with the target is one of the significant limitations since it may deform the integrity of the target [25, 26].

Mechanical properties related to cell and tissue state can also be obtained by optical tweezers. The working mechanism of optical tweezers is dependent upon a focused laser beam to produce a potential well for trapping of micron or nano sized particles in a region that is close to the beam focus. Mostly, microbeads (e.g. polystyrene or silica) are attached and used as handles during experiment to trap and manipulate cells and organelles. Optical tweezers can also be employed to quantify the interaction force of

a living-single cell to a various kinds of extracellular matrix (ECM) substrates, and to investigate the physical interactions in the cellular and subcellular level [21, 27–31]. However, conventional optical tweezers, which are mostly used to trap and stretch biological samples, encounter major limitations such as a high spring constant relative to the elasticity modulus of the sample. Furthermore, non-physiological handling by surface attached microbeads can also result in measurement artifacts. Although each technique may give similar results, the optical tweezers modality ends up being the preferred application for studying with biological matters.

In cell mechanobiology, magnetic tweezers probe molecular forces, trap and manipulate cells such as single molecule force measurements or extra and intracellular micromanipulation through applying torque using tiny magnetic beads. With high sensitivity, this tool allows measuring forces that change from pN to nN under the effect of a varying magnetic field. Magnetic tweezers lacks experimental resolution because of the visual data recording methods employed during the investigations [32, 33].

Acoustic tweezers allow studying the mechanical properties of biological media through the approach that radiation pressure at the contact point of a sound beam is able to yield a stable potential well. The sound beam in acoustic tweezers has low intensity power and low influence of viability of cells. Hence, this technique is accepted as highly cytocompatible. Using sound waves that are obtained by the incorporation of piezoelectric transducers, manipulation of biological media can be achieved without the requirement of interaction, surface modification of labelling. However, mechanical stress application can be counted as a drawback of this method [24, 34].

This introductory chapter has reviewed the importance of cell mechanics and currently available imaging methods. They have become hot research fields in both pre-clinical and clinical practices since the biomechanical features of biological media are closely related to physiological and pathological states. Nevertheless, the use of biomechanical parameters in clinical settings is at an early stage, and numerous essential problems remain to be addressed. Thus, new methodologies need to be developed,

which are completely non-harmful, easy-to-handle, and measuring mechanical properties at high speed. Further knowledge in cell mechanics will elucidate understanding cells or tissues and their functions broadly, and provide novel perception for diagnosis and prognosis of diseases.

Thus, this thesis intends to highlight the applicability of Scanning Acoustic Microscopy and Dual-Beam Optical Tweezers in cell and tissue mechanics by setting acoustic impedance and deformability as the principal mechanical parameters to further elucidate biological surroundings' mechanical responses to external inputs. Detailed literature review for ultrasound imaging and optical tweezers will be explained in the remainder of Chapter 1.

1.2. Ultrasound Imaging

A mechanical collision produces vibrations on particles within the observed target. The vibration develops a longitudinal wave or compressional wave, where back and forth particle dislocations are parallel to the direction of sound wave travel. Vibrations or waves encountering a vibrating source on-air generate audible sound recognized through the human ear. The frequency interval of human hearing is ranging from 20 Hz to 20 kHz. Almost all types of vibrations are termed as acoustic, while those of too high a tone of sound for the human hearing to notice are also specified as ultrasound. Namely, the sound yielded with a frequency higher than 20 kHz is employed as ultrasound. Ultrasound points out a mechanical pressure wave traveling through a medium. As the wave propagates, alternate compression (C) and rarefaction (R) of pressure (P) lead to oscillations of particles around their equilibrium state. On the one hand, high-pressure defines compression, in which that wave particles are jointly positioned. On the other hand, low pressure defines rarefactions by wave particles thinly positioned within this region, see Figure 1.3. In terms of physical features, ultrasound does not differ from audible sound [2, 35, 36].

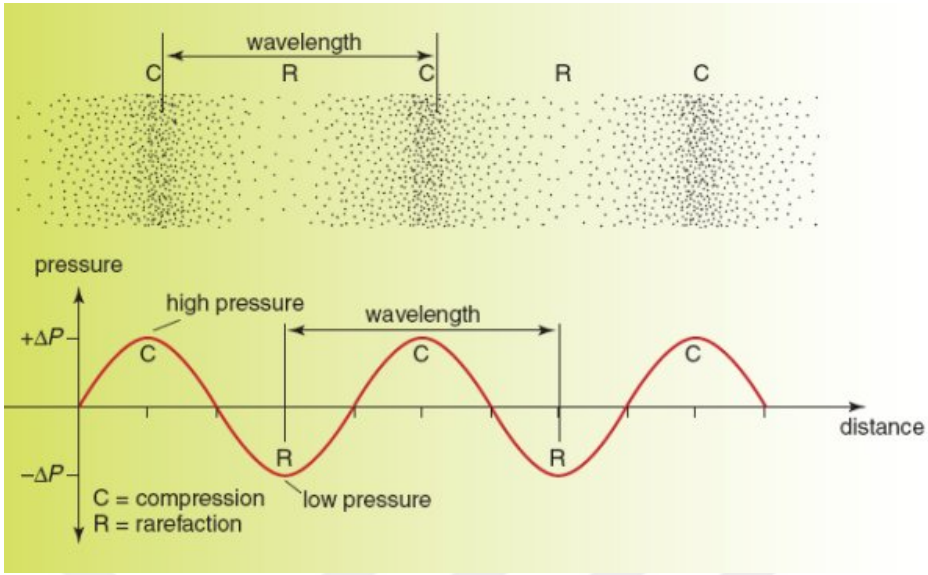


Figure 1.3. Characteristics of ultrasound waves [36].

Figure 1.4 illustrates spectrum of sound and its applications. In the early 1970s, the use of ultrasound technology and its application in medicine became an approved monitoring tool when the first gray-scale ultrasound image together with nonlinear compression dynamic range was introduced [37]. Reducing the dynamic range of the ultrasound image, the compression empowered the imaging methodology to obtain much more detailed information about the structure of the tissue. Later, significant progress was made to understand high-frequency sound wave interaction with biological matter, which in turn permitted the ultrasound technology to mature. A variety of diagnostic tests for diseases such as cancer are available in the market, including Positron Emission Tomography (PET), Magnetic Resonance Imaging (MRI) and Computed Tomography (CT). Ultrasound imaging offers three fundamental benefits over those technologies: real-time monitoring ability, relative low cost and non-ionizing radiation during the measurement [38].

Ultrasound imaging has a key role in cancer diagnosis and prognosis due to its relative low cost, sub-millimeter spatial resolution, easy operation and non-ionizing nature. Cancer monitoring by clinical ultrasound scanners are performed by brightness

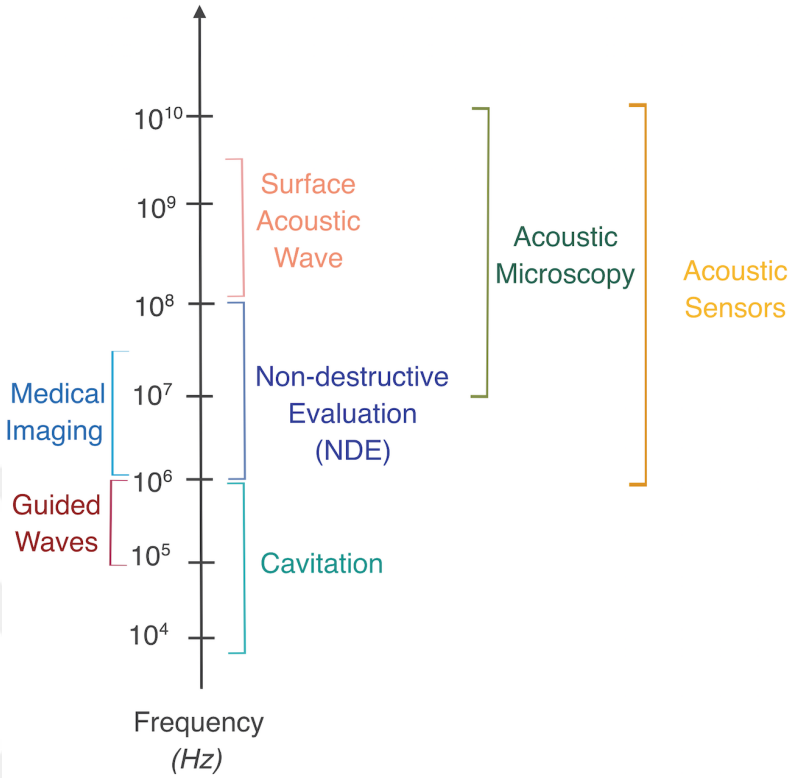


Figure 1.4. Frequency range of ultrasound and its applications (adapted from [2])).

mode (B-mode) ultrasound imaging. Ultrasonic probes are used to convert electric pulses into acoustic waves. They have the capacity to transmit acoustic waves and recognize resulting reflections from ultrasound-biological matter interaction to construct an image in B-mode ultrasound. Acoustic concentration, acoustic impedance, compressibility, scatterer size are the characteristics that lead to a contrast in the ultrasound image of the matter. Ultrasound scattering by a non-cancerous tissue and a cancerous tissue is mostly different because of the numerous mechanical and structural transformations in disease progression. This leads to a detectable contrast difference between the non-cancerous and cancerous tissue. Hence, ultrasound imaging can distinguish cancerous region from its non-cancerous counterpart using the acoustical characteristics of the tissue. Frequencies in medical ultrasound for diagnosis and prognosis vary from 1 to 15 MHz. The optimum ultrasonic frequency is selected considering the

location of tissue in the body, depth penetration and spatial resolution [38, 39].

Frequencies above 20 MHz have been greatly studied to increase the image resolution in skin, ocular, liver and small animal imaging in pre-clinical settings [40]. High-frequency ultrasound imaging (10-60 MHz) offers a micrometer resolution that is able to reflect fine details of the biological media. The ability of high-frequency ultrasound imaging is tested to understand further the mechanism behind tumor growth, angiogenesis and drug influences, and anticancer therapies in preclinical models [41–44]. Generally, in clinical ultrasound imaging, the reflectivity of the tissue as a function of depth is analyzed. However, frequency analysis of the scattered signal is not presently employed in clinical settings. To acquire more information about the micro-environment of the biological matter, backscattered frequency spectrum quantification has been employed in research laboratories [45–49]. However, there are still limitations that require to be addressed to interpret the micromechanical complexity of biological surroundings, and advance the current ultrasound imaging.

As previously mentioned, Chapter 2 and 3 of this thesis will describe micrometer resolution ultrasound application for biomedical requirements in pre-clinical assessments, specifically for cancer and anticancer treatment effects. The fundamental physics behind ultrasound imaging and physical characteristics of the ultrasound probe defining the resolution and depth penetration will be discussed in detail in the remainder of Section 1.2 and Sub-chapter 1.3.

1.2.1. Sound Propagation

Sound is a mechanical energy carried within a continuous, elastic environment through the action of elastic stresses and it contains local compression and expansion of constituent particles. The presence of acoustic waves is directly explicated through the compressibility κ and density ρ of an object jointly the conservation of mass and momentum laws. The wave propagates at a sound speed c, expressed by [50],

$$c = \sqrt{\frac{1}{\kappa\rho}}, \tag{1.1}$$

in which κ refers to the compressibility and ρ is the density of the surrounding. Acoustic waves are described using the wave equation, which is one of the classical partial differential equations of physics. They are three-dimensional (3D) time-dependent waves. In terms of spatial domain, they are expressed by three spatial variables x, y, and z, and time t. When the wave travels inside the matter into x, y and z direction, the particles are moved from their balances, and the plane wave, $\phi(\vec{r}, t)$ is described by the following equation.

$$\phi(\vec{r}, t) = \phi_0 e^{i(\omega.t - \vec{k}\cdot\vec{r})} \tag{1.2}$$

where the parameter r refers to the plane wave propagation into x, y and z direction, and it is defined as $\mathbf{x}_{ax} + \mathbf{y}_{ay} + \mathbf{z}_{az}$, k expresses the wave number, $k = \omega/c$, and ω is the angular frequency.

Besides, the three-dimensional wave equation is given by using Laplacian operator $\nabla^2 = \frac{\partial^2}{\partial x^2} + \frac{\partial^2}{\partial y^2} + \frac{\partial^2}{\partial z^2}$.

$$\left(\frac{\partial^2}{\partial x^2} + \frac{\partial^2}{\partial y^2} + \frac{\partial^2}{\partial z^2}\right)\phi(\vec{r}, t) = \frac{1}{c^2}\frac{\partial^2\phi(\vec{r}, t)}{\partial t^2}. \tag{1.3}$$

When a plane wave propagating through one dimension such as z-direction, the wave

equation is given as follows

$$\frac{\partial^2\phi(z,t)}{\partial z^2} = \frac{1}{c^2}\frac{\partial^2\phi(z,t)}{\partial t^2}. \tag{1.4}$$

Substituting the first and second derivatives of plane wave with respect to time and z-direction, the Laplacian will be equal to

$$\nabla^2\phi = -k^2\phi. \tag{1.5}$$

Using the Laplacian definition above and the time derivation of the plane wave, dispersion relation is obtained, which relates angular frequency ω, wave number k and sound speed c [2, 50] as

$$\omega^2 = c^2k^2. \tag{1.6}$$

The properties of an acoustic wave comply with the characteristics of the material element, where it is travelling through the acoustic impedance, Z, which is defined dividing pressure by particle velocity [51]:

$$Z \equiv \frac{p(z,t)}{v(z,t)}. \tag{1.7}$$

Inserting pressure and velocity into Equation 1.7 and using $k = \omega/c$ and $\kappa = 1/\rho c^2$ one obtains,

$$Z = \rho c. \tag{1.8}$$

The SI unit for acoustic impedance Z is kg$\cdot/$m^2s which is also expressed as Rayleigh (Rayl). Principally, the acoustic impedance can be identified as the rigidity or the flexibility of a compressible medium, and is a measure of how particles within the medium act under the effect of the sound wave pressure.

1.2.2. Reflection and Transmission

Sound wave interaction with the matter is characterized through acoustic properties. When acoustic pressure passes through the medium, variations in the mechanical features lead to the ultrasound waves to experience interactions covering reflection, transmission, refraction, absorption, and scattering. Ultrasound is reflected when it strikes the boundary between two regions where there is a variation in compressibility or density [50, 51]. To be more informative, the reflection of ultrasound energy arises at an interface of two regions in which there is a difference in the neighbor matters' acoustic impedance. When a perpendicular sound wave strikes a medium having an acoustic impedance, Z_1, to a medium of acoustic impedance Z_2, a portion of the sound intensity turns back to the transducer as an echo, and transmitted fraction of the beam follows its initial direction, see Figure 1.5.

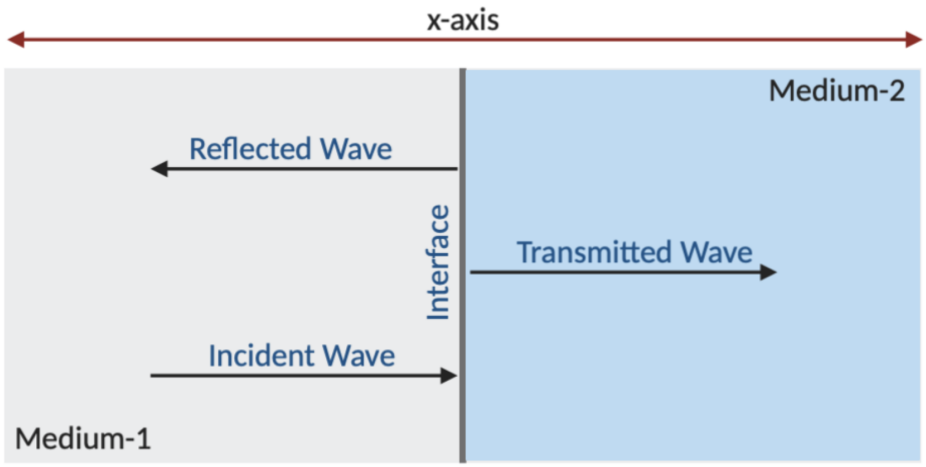


Figure 1.5. When medium 1 and medium 2 have the same acoustic impedance, their interface line will not create a reflection. A weak reflection is obtained when the difference in acoustic impedance is small. A strong reflection is produced when the difference is large. All the ultrasound is totally reflected from the interface line when the difference is considerably large.

The intensity reflection coefficient, R_I illustrates the ratio of reflected intensity to the incident intensity. It is readily figured out from the acoustic impedance of each material as

$$R_I = \frac{I_r}{I_i} = \left(\frac{Z_2 - Z_1}{Z_2 + Z_1}\right)^2. \tag{1.9}$$

The intensity transmission coefficient, T_I illustrates the ratio of the transmitted intensity relative to that of the incident intensity. It is given as

$$T_I = \frac{I_t}{I_i} = \frac{4Z_1Z_2}{(Z_1 + Z_2)^2}. \tag{1.10}$$

The difference in route of a transmitted beam when it crosses a boundary between two media, where the speed of sound are not same, is termed refraction, as can be seen in Figure 1.6.

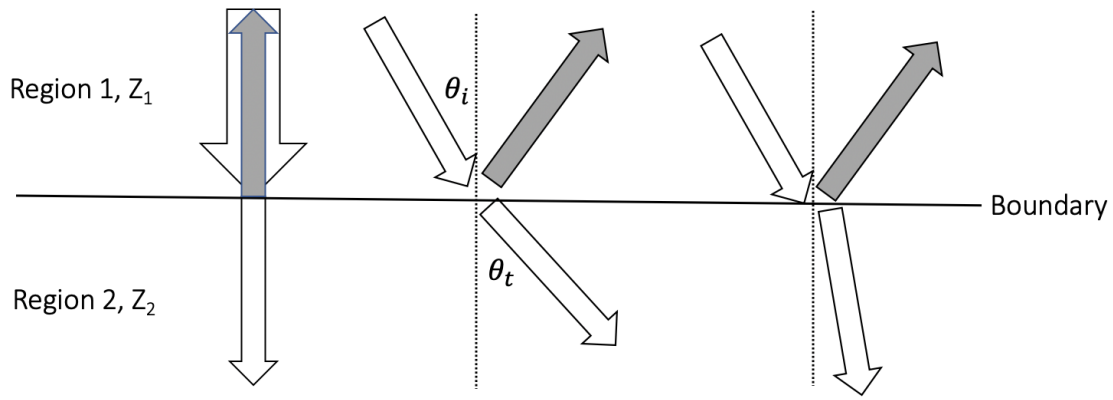


Figure 1.6. Schematic description of incident, reflection and refraction of ultrasound waves at target boundaries having different acoustic impedance values, Z_1 and Z_2. (a) 90 C° vertical incidence of sound wave, (b) non-vertical incidence (c_1<c_2, (c) non-vertical incidence c_1>c_2.

There is no beam bending when the incidence angle is equal to 90°. However, there is a change in the direction for all other angles relative to that of the normal incidence on the boundary. The new angle of the beam, θ_R, bends in accordance with the change in the sound speed occurring at the interface, and is linked with the angle of incidence θ_I. It is readily extracted using Snell's law [50, 51]:

$$\frac{\sin\theta_T}{\sin\theta_I} = \frac{c_2}{c_1} \tag{1.11}$$

in which θ_I and θ_T refer to the incidence and transmitted angles, c_1 and c_2 give the speed of sound in media of 1 and 2, respectively.

1.2.3. Absorption and Attenuation

The interaction of sound waves with the matter is also determined through absorption. As an ultrasound wave travels through the target, ultrasound wave pressure losses its intensity with distance traveled, since the vibrational energy is transformed to random vibrational thermal energy. This situation is termed as absorption. When ultrasound frequency is high enough, the amplitude decreases more rapidly. It also relies on the target involved. Besides absorption, the main elements contribute to the total attenuation of the wave amplitude are reflection, scattering, and divergence of the beam. Scattering and beam divergence are dependent on the frequency used. Thus, attenuation is remarkably based on frequency. When an acoustic pressure or a wave penetrates through a known thickness of target, attenuation can be quantified through recording the reduction in pressure amplitude. The decrease in the pressure amplitude is given in dB/cm (attenuation coefficient) through input and output pressure amplitudes ratio, which is obtained from either side of the target [50, 51]. Attenuation is also based on the type of tissue. In biological tissue or organs, attenuation is greater for denser and harder tissues (e.g. bone) and is lower for liquid-like media (e.g. blood and cysts). With this in mind, for high-frequency ultrasound imaging, the attenuation gets greater values compared to lower frequency ultrasound imaging. Namely, higher frequency ultrasonic probes are used to visualize superficial organs such as skin whereas

lower-frequencies are employed for organs that are located in deeper locations within body. The relation is shown by Figure 1.7.

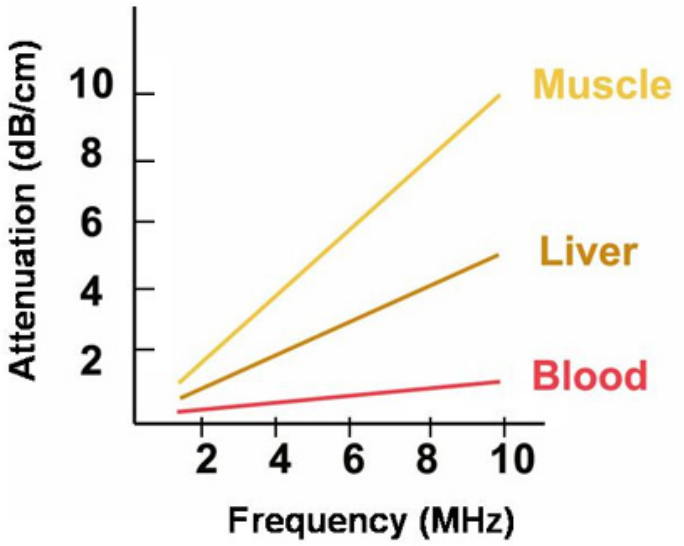


Figure 1.7. Attenuation relation with the type of tissues and ultrasonic frequency [52].

In our SAM system, sound waves pass through three separate media, liquid and two solids. When sound waves travel within liquids, the energy of the waves will be dissipated due to the absorption characteristics of the medium. The equation, which establishes a relation among attenuation β_a, shear viscosity η_{visc}, volume viscosity (η^v) and heat conduction (τ) is given by [53, 54]

$$\beta_a \left[\frac{np}{cm}\right] = \frac{\omega^2}{2\rho c^3}\left[\left(\frac{4}{3}\eta_{visc} + \eta^v\right) + \tau\left(\frac{1}{c_v} - \frac{1}{c_p}\right)\right] \tag{1.12}$$

where ρ, ω and c account for medium density, angular frequency, sound speed in the medium, heat capacity at a constant volume c_v and pressure c_p, respectively.

The attenuation coefficients of pure water and other types of liquids having a low viscosity and low attenuation are expected to have a linear relationship with the sound wave frequency for homogeneous liquid

$$\beta_a(f) = a + bf \tag{1.13}$$

where f is the frequency, $a = -0.001119$ and $b = 0.001877$ [53].

As for solid medium, the relative attenuation is quantified as a function of temperature, magnetic fields or pressure [55]. In our experimental set-up, ultrasound is traveling through sapphire lens of ultrasonic transducer, coupling agent, polystyrene substrate and target. Thus, attenuation of sound within sapphire and polystyrene must be considered. The ultrasonic attenuation of sapphire (dB/μs) can be extracted from the attenuation line graph [56]. For polystyrene, some studies evaluate attenuation for polystyrene material by showing attenuation line as a function of sound frequency. The polystyrene attenuation (γ_a) ranges from 6 to 10 dB/cm for clinical ultrasound frequencies [57, 58].

1.2.4. Scattering

Acoustic scattering occurs when an ultrasound wave interacts with structures within a target, where the size of the wavelength is relatively smaller compared with the structures. Alterations in the acousto-mechanical features of the target lead to the ultrasound waves to scatter. Namely, some of the wave energy is diffused in many directions different than the incident wave. The scattered ultrasound signal at a specific angle is defined through differential scattering cross-section $\sigma(\theta, \varphi_{sp})$ (cm^2/sr) [51]:

$$\sigma(\theta, \varphi_{sp}) = \frac{S_{sc}(\theta, \varphi_{sp})}{I\Omega}, \tag{1.14}$$

where θ, φ_{sp} refers to spherical coordinates angles, S_{sc} is the time-averaged scattered

ultrasound power by the target, I corresponds to the time-averaged incident intensity and Ω is the solid angle.

Variations in the mechanical properties of the target affect the cross-section of differential scattering, which is a function of the ultrasonic wavelength. The ratio of the scatterer source size to the wavelength of the incident ultrasound defines the scattered ultrasound signal. This relationship is expressed by the product of wave number $k = \frac{2\pi}{\lambda}$ and scatterer source size a_{sc} as a parameter ka_{sc}. For a target's theoretical differential cross-section determination, the Helmholtz wave equation is solved for the scattering geometry and boundary conditions. Under the assumption that the scatterer size is much larger than the ultrasound wavelength ($ka_{sc} >> 1$), solely variations in the acousto-mechanical characteristics may be used to estimate the scattered signals. When the scatterer is much smaller than the wavelength, the Rayleigh scattering formula that is valid for ($ka_{sc} << 1$) is given by Equation 1.15 where the scatterer and the surrounding medium have densities of ρ_{sc} and ρ_0, $\langle n \rangle$ is the average number density of scatterers, V volume of scatterer, and compressibilities of κ_1 and κ_0, respectively [51]:

$$\sigma(\theta) = \langle n \rangle \frac{k^4 V^2}{16\pi^2} \left[\frac{\kappa_1 - \kappa_0}{\kappa_0} + \frac{3\left(\rho_1 - \rho_0\right)}{2\rho_1 + \rho_0} \cos\theta \right]^2 . \tag{1.15}$$

Under the case that the wavelength of the sound wave is comparable to the scatterer source size, scattering is more complex. The exact solution for the sound scattering by single cylinders and spheres has been proposed by Faran [59]. The Faran equation anticipates the differential backscattering cross-section from a single scattering source that has a defined shape in a liquid-like medium. However, this equation is not directly used for scattering from biological surroundings. This is because biological surroundings contain different size and shape scatterers and mechanical features.

Biological matter indicates inhomogeneous characteristics with fluctuations in the acoustic impedance distribution. In order to count the presence of inhomogeneties, the wave equation for such matter has been simplified via some approximations. It is

supposed that the amplitude of the scattered wave is much smaller compared to that of the incident wave in the biological matter. This is called Born approximation [60]. With this approximation, the the differential cross-section of inhomogeneous matter (biological soft matter) is simplified to:

$$\sigma_d = \frac{k^4 \langle \gamma^2 \rangle}{16\pi^2} \int_{-\infty}^{\infty} b_\gamma(\Delta r) e^{-iK\cdot\Delta r} d\Delta r \tag{1.16}$$

where $\langle \gamma^2 \rangle$ refers to the mean-square fluctuation in the acoustic impedance, $\boldsymbol{K}$ indicates the variation in wave number, Δr is the position change in the matter and correlation coefficient $b_\gamma(\Delta r)$.

1.3. Scanning Acoustic Microscopy

Ranging from the fundamental optical, electron and scanning probe microscopes, a vast amount of microscopy methods are widely used for the inspection of details in micro, nano and down to molecular and atomic scales. Optical microscopes involving confocal laser scanning microscopy, Raman spectroscopic analysis, phase contrast and dark field illumination have been evolved [61]. The efforts are continuing to increase resolution by breaking the obstacles created by diffraction. All these microscopes have specific features, benefits and drawbacks, and they generally should be regarded as a complementary tool. On the other hand, most optical methods have limitations due to absence of ability in investigation of micro-mechanical features, surface topology and chemical composition. Accordingly, analysis of elasticity of a material under observation using previously mentioned methods is yet an open question.

Scanning Acoustic Microscopy (SAM), in principle resembling to the optical microscopy but using high frequencies rather than light, has been developed to assess the acousto-mechanical properties of objects under investigation to overcome the issues. Application of high-frequency sound waves to distinguish object information dates back to 1936 when S. J. Sokolov introduced that sound waves at a 3 GHz frequency by the wavelength of 500 nm in water might be employed for an ultrasonic microscope [62]. In

1974 at Stanford University, Lemon and Quate developed SAM in transmission mode for the first time. The first SAM was tested for biomedical applications [63]. Then, it was improved both theoretically and experimentally via inspecting different biological specimens by Maev *et al.* [64]. Frequencies of sound waves in acoustic microscopy changes from several mega-Hertz (MHz) to several giga-Hertz (GHz) [64].

Sound waves have the ability to permeate the interior of the objects, which are impenetrable for the electromagnetic waves in the visible spectrum of the electromagnetic waves. This skill offers a non-harmful visualization and the determination of micro-elastic characteristics of structures, and thereby could be applicable to industry and biomedical areas [65]. The non-ionizing nature of ultrasonic radiation possesses an additional benefit as a suitable tool for visualization of live cells and fresh tissues permitting monitoring in a limited life cycle of live cells [66, 67].

SAM offers two different measurement modes, acoustic impedance and sound speed, which correspond to the distinct combinations of software configurations in SAM computer and measurement set-ups. In this section, this thesis will focus on the theory for acoustic wave propagation in the multi-layer media, and thus reflection and transmission ratio dependent on boundary conditions at interfaces. It will also introduce acoustic impedance measurement and sound speed measurement modes.

1.3.1. Boundary Conditions at Liquid-Solid and Solid-Solid Interfaces

A SAM system operates by a source of vibration producing longitudinal waves from the oscillations of the crystal in the source, medium and receptor to catch the sound wave. Sound energy is carried by the medium from one layer to another. In general, it is assumed that sound waves pass through the homogeneous medium. However, an incident longitudinal sound wave, at a flat boundary, which is created by a dissimilar acoustic properties of homogeneous media, is partially reflected and partially transmitted. Acoustic wave is a pressure wave and normal incidence will only result in the pressure wave. Suppose that an acoustic wave passes through medium-1 to

medium-2, so that

$$\phi_I = A_I e^{j(\omega t - k_1 x)} \tag{1.17}$$

where ϕ_I, A_I and ω refer to sound potential magnitude of incident pressure wave and angular frequency of the wave, respectively.

When, incoming wave, which is an undamped and longitidunal wave, approaches the flat interface line, it is partly reflected and partly transmitted. Reflected and transmitted waves can be described by Equation 1.9 when incident wave amplitude is assumed to be equal to unity

$$\begin{aligned} \phi_R &= A_R e^{j(\omega t + k_1 x)} \\ \phi_T &= A_T e^{j(\omega t - k_2 x)} \end{aligned} \tag{1.18}$$

where $k_1 = \omega/c_1$ and $k_2 = \omega/c_2$. When this wave has a particle motion in the xz plane, the boundary is created at z=0. Two boundary conditions at the interface, which are continuity of pressure and displacement, must be fulfilled. Following earlier Equation 1.9, the pressure amplitude reflection coefficient can be given through the acoustic impedance of each medium for normal incidence at an interface between medium 1 and medium 2 [2, 68]

$$A_R = \frac{Z_2 - Z_1}{Z_2 + Z_1}. \tag{1.19}$$

Moreover, the pressure amplitude transmission coefficient can directly be given as

$$A_T = \frac{2Z_2}{Z_2 + Z_1}. \tag{1.20}$$

In acoustic microscopy, when a substrate such as polystyrene or glass is introduced, an interface line will arise at the boundary between the coupling agent and the substrate. An emitted plane wave from the vibration source at a general angle of incidence to the

matter will alter the propagation direction through obeying Snell's law as described in the following equation [2, 68]:

$$\frac{v_I}{v_T} = \frac{\sin\theta_I}{\sin\theta_T}, \tag{1.21}$$

in which v_I and v_T give the velocities of the incident and transmitted sound waves, respectively; and θ_I and θ_T are incidence and transmission angles, respectively.

A sound wave is a collection of many varying angles of plane waves. Snell's law necessitates the wave vector portion to be continuous parallel to the interface line. For oblique incidence analysis of the sound propagation, calculations of the reflection and transmission coefficients get more problematic due to the pressure and shear waves of incident, reflected and transmitted waves. The angles and the velocities of plane mechanical wave propagation for liquid-isotropic solid boundaries, created by two semi-infinite media, play an important role for acoustic microscopy. For this condition, a compressional, L, wave in the liquid, and two transmitted waves in the solid, a compressional wave and a shear wave, S, arise. In liquid-solid boundary, pressure distortion and potential displacements have to be equal to meet the boundary conditions. When the acoustic wave propagates through the liquid medium, shear wave is neglected since such liquid environment cannot support shear-wave propagation due to the absence of shear rigidity. Namely, for liquid medium, only incident and reflected acoustic waves should be considered. Shear wave is disregarded in liquid medium but it must be studied for solid medium. Since the liquid might slip along the interface line, Snell's law for this case [2, 68] becomes

$$k\sin\theta = k_L\sin\theta_L = k_{\mathrm{S}}\sin\theta_{\mathrm{S}}. \tag{1.22}$$

Acoustic impedance for liquid and solid media for pressure and shear waves are given by

$$Z = \frac{\rho_0 v_0}{\cos\theta} \quad Z_L = \frac{\rho_1 v_L}{\cos\theta_L} \quad Z_{\mathrm{S}} = \frac{\rho_1 v_{\mathrm{S}}}{\cos\theta_{\mathrm{S}}}. \tag{1.23}$$

Liquid-solid interface line is composed of medium-1 (liquid) in space z<0 and medium-2 (solid) in space z>0. In medium-1, incident and reflected acoustic waves arise while medium 2 consists of transmitted acoustic and shear waves, as illustrated in Figure 1.8.

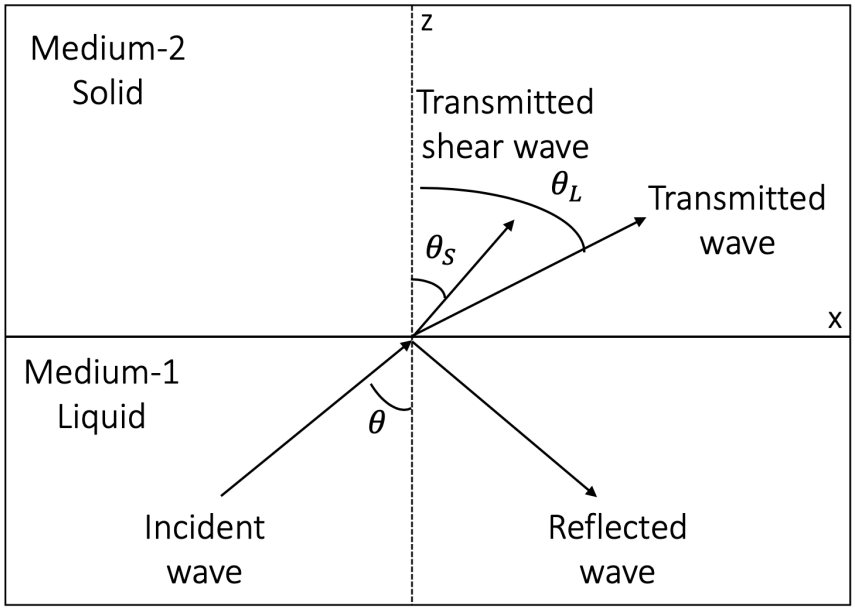


Figure 1.8. Wave propagation direction for liquid-solid interface.

The displacement of particle velocity can be described by pressure L and shear waves S as,

$$U = \text{grad}\,\phi_L + \text{rot}\,\phi_S. \tag{1.24}$$

Stress distortion is figured out from the first derivation of the displacement of particle velocity, and can be expressed by elastic E and shear μ moduli as follows, [2,68]

$$\sigma_{st} = E\left(\frac{\partial u_x}{\partial x} + \frac{\partial u_z}{\partial z}\right) + 2\mu\frac{\partial uz}{\partial z}. \tag{1.25}$$

Within this layer, presuming an ideal non viscous material, three different boundary conditions, continuity of normal velocity, continuity of normal stress and zero tangential stress should be confirmed. Reflection coefficient is

$$A = R_L = \frac{Z_{total} - Z}{Z_{total} + Z}. \tag{1.26}$$

Transmission pressure and transmission shear coefficients for oblique incident wave at the interface line are [2, 68]

$$A_T = T_L = \frac{2Z_L \cos 2\theta_{\mathrm{L}}}{Z_{total} + Z} \tag{1.27}$$

, and

$$A_{ST} = T_{\mathrm{S}} = -\frac{2Z_{\mathrm{S}} \sin 2\theta_{\mathrm{S}}}{Z_{total} + Z} \tag{1.28}$$

where

$$Z_{\mathrm{total}} = Z_L \cos^2 2\theta_{\mathrm{S}} + Z_{\mathrm{S}} \sin^2 2\theta_{\mathrm{S}}. \tag{1.29}$$

Solid-solid interfaces should also be considered carefully to understand working principle of acoustic microscopy. Longitudinal and shear waves arise for both medium-1 (solid) and medium-2 (solid), which is shown in Figure 1.9.

In this case, six types of waves should be taken into account: the incidence of pressure and shear waves, the reflection of pressure and shear waves, and the transmission of pressure and shear waves. Reflection and transmission coefficients at the flat solid-solid interface line can be mathematically given by the four boundary conditions that should be fulfilled along the boundary created by two isotropic solid materials. Particle displacement in the xz plane due to the incident pressure wave from a solid

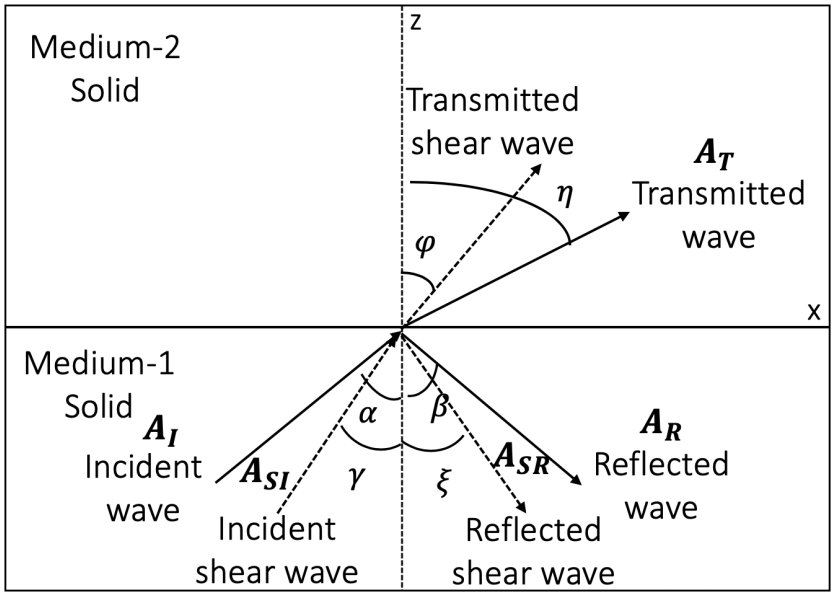


Figure 1.9. Wave propagation direction for solid-solid interface.

onto a solid is given by [2, 68]

$$\phi_I = A_I e^{j(\omega t + k_{x1} \cdot x - k_{z1} z)}. \tag{1.30}$$

Since the incidence angle, which is given as the angle between the direction of wave propagation and the normal line to the interface, is known, the particle displacement can also be described by sine or cosine functions of the incident angle of the wave. Thus, the particle displacement due to pressure and shear waves can be written as follows

$$\begin{aligned} \phi_I &= A_I e^{j(\omega t + k_{L1} \cdot \sin\alpha x + k_{L1} \cos\alpha z)} \\ \phi_{SI} &= A_{SI} e^{j(\omega t + k_{S1} \sin\gamma x + k_{S1} \cdot \cos\gamma z)} \end{aligned} \tag{1.31}$$

For pressure and shear waves, the sound potentials can described together with reflec-

tions,

$$\begin{aligned} \phi_R &= A_R e^{j(\omega t + k_{L1}\sin\beta x - k_{L1}\cos\beta z)} \\ \phi_{SR} &= A_{SR} e^{j(\omega t + k_{S1}\sin\xi x - k_{S1}\cos\xi z)} \end{aligned} \tag{1.32}$$

Also, the sound potentials of pressure and shear waves are given together with transmissions,

$$\begin{aligned} \phi_T &= A_T e^{j(\omega t + k_{L2}\sin\eta\ x + k_{L2}\cos\eta z)} \\ \phi_{ST} &= A_{ST} e^{j(\omega t + k_{S2}\sin\varphi x + k_{S2}\cos\varphi z)} \end{aligned} \tag{1.33}$$

The first continuity requirement refers to the particle's velocity displacement u_x for z=0. In calculation of reflection and transmission coefficients, it is assumed that there is no displacement along the y-axis, and the velocity displacement at the solid-solid boundary is calculated using Equation 1.24. As a second boundary condition, continuity of displacement u_z at z=0 should be established. Stress distortion continuities of σ_x and σ_z at z=0 using Equation 1.25 must also be achieved to define the reflection and transmission coefficients value. The equations of four boundary conditions and the relation among the waves are formulated in matrix form [2, 68, 69]:

$$\begin{aligned} &\begin{pmatrix} k_{S1}\cos\xi & k_{L1}\sin\beta & k_{S2}\cos\varphi & -k_{p2}\sin\eta \\ -k_{S1}\sin\xi & k_{L1}\cos\beta & k_{S2}\sin\varphi & k_{p2}\cos\eta \\ \rho_1\sin 2\eta & -\rho_1\cos 2\eta & \rho_2\sin 2\varphi & \rho_2\cos 2\varphi \\ -\rho_1\cos 2\xi & -\frac{\mu_1\rho_1}{E_1+2\mu_1}\sin 2\beta & \rho_2\cos 2\varphi & -\frac{\mu_2\rho_2}{E_2+2\mu_2}\sin 2\eta \end{pmatrix} \begin{pmatrix} A_{SR} \\ A_R \\ A_{ST} \\ A_T \end{pmatrix} \\ &= \begin{pmatrix} k_{S1}\cos\gamma & -k_{L1}\sin\alpha \\ k_{S1}\sin\gamma & k_{p1}\cos\alpha \\ \rho_1\sin 2\gamma & \rho_1\cos 2\gamma \\ \rho_1\cos 2\gamma & -\frac{\mu_1\rho_1}{E_1+2\mu_1}\sin 2\alpha \end{pmatrix} \begin{pmatrix} A_{SI} \\ A_I \end{pmatrix} \end{aligned} \tag{1.34}$$

In this matrix, the terms A_{SI} and A_I refer to incident shear and pressure sound waves, A_{SR} and A_R are reflection of shear and pressure sound waves, A_{ST} and A_T stand for the shear transmission and pressure transmission waves where α, γ, β, ξ, η, φ are

the angle of incidence, reflection and transmission of the pressure and shear waves for medium-1,2, respectively. c_{S1}, c_{S2}, c_{L1} and c_{L2} are shear waves and pressure waves for medium-1,2, respectively. k_{L1}, k_{L2}, k_{S1}, k_{S2} are wave numbers of pressure and shear waves for each solid medium. ρ_1 and ρ_2 refers to density of isotropic solid medium-1 and isotropic solid medium-2. E_1 and E_2 are the elastic moduli of medium-1 and medium-2 while μ_1 and μ_2 indicate the shear moduli for the media.

1.3.2. Acoustic Impedance Measurement Mode

Acoustic impedance is expressed as "density" × "sound speed", which is the measure of the response of a target reacting to the acoustic flow due to the applied acoustic pressure [2]. In acoustic impedance mode, two-dimensional image of SAM is extracted from the acoustic intensity, which is reflected from the target, as illustrated in Figure 1.10.

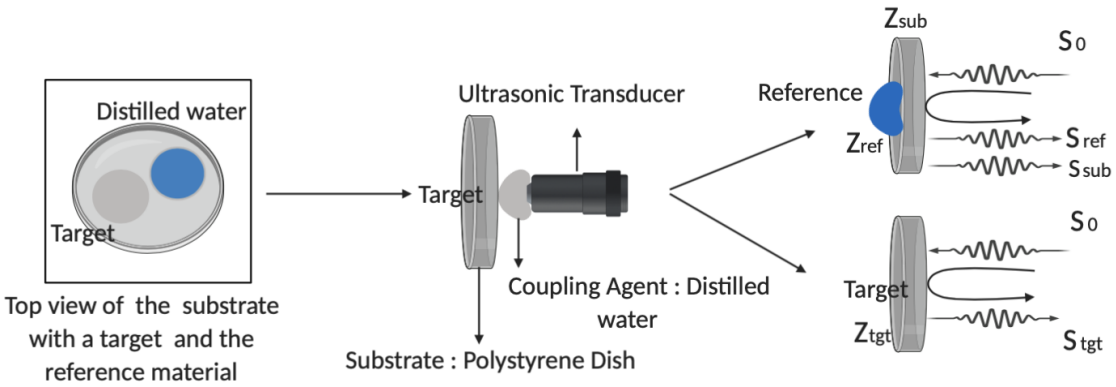


Figure 1.10. Signals in acoustic impedance measurement configuration.

The ultrasonic wave, which is emitted from the ultrasonic transducer, penetrates through several layers such as coupling liquid, polystyrene substrate and target. Then, it reflects at substrate-target interface. Acoustic images emerges at the interface line between the target and the rear surface of the substrate. Ultrasonic beam traveling within multi-layer surroundings is illustrated in Figure 1.11.

When an ultrasound wave penetrates through multi-layer media by a deflection

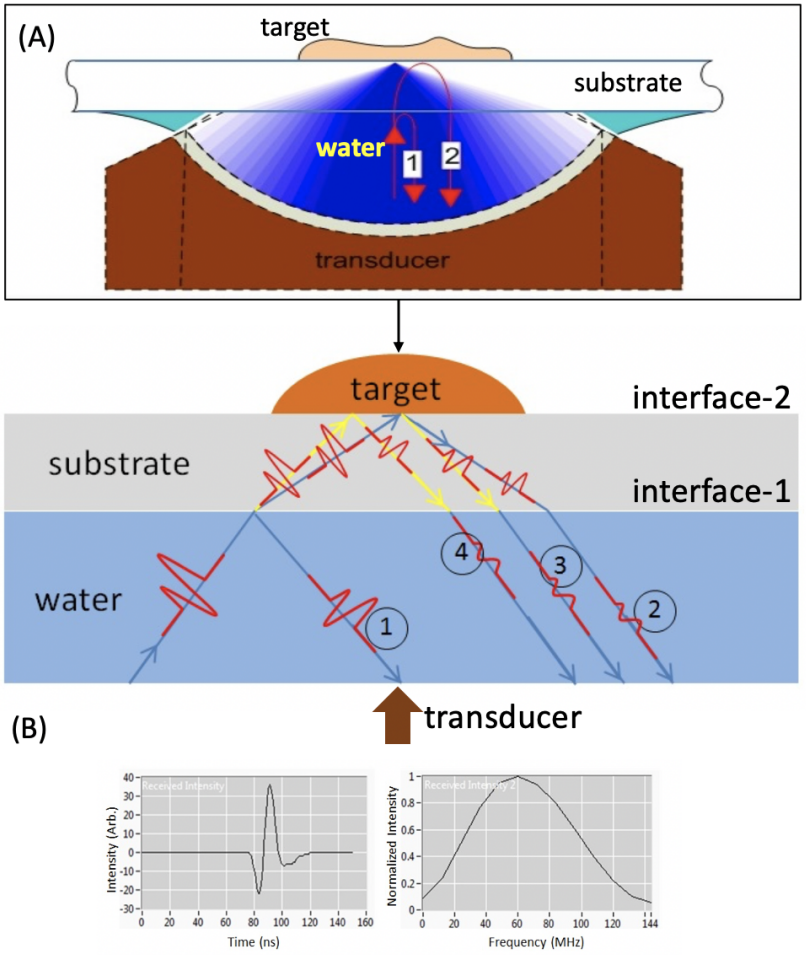


Figure 1.11. The top side (A): Ultrasound wave traveling in multi-layer media: water, substrate and target, respectively. Blue and yellow arrows illustrate traveling of longitudinal and generated shear waves, respectively. The bottom side (B): Waveform and reflection path of waves from the boundary lines resulted from water-substrate and substrate-target [2].

angle, pressure and shear waves are yielded related to the properties of the medium. For water or liquid medium, shear wave presence is disregarded since it could not support static shear stress due to its weak bounding characteristic. Thus, pressure wave solely arises in a liquid layer as illustrated in Figure 1.11. It usually possesses a higher speed in comparison to the shear wave. Shear wave is not considered for liquid but it has to be taken into consideration for solid such as polystyrene substrate. Firstly, when the sound wave hits a boundary of liquid-solid (water-substrate) media, it will partially reflect, as shown by number 1 in the top side of Figure 1.11. Following the propagation in water medium, when the wave impinges on the polystyrene medium, transmitted pressure and shear waves components are present. The waves will transmit as pressure waves within the coupling liquid. In the bottom side of Figure 1.11, typical waveform and frequency spectra of reflected sound wave from the interface line between the rear surface of the substrate-target is illustrated.

In acoustic impedance measurement mode, vertical incidence investigation of the reflected sound waves from the reference material and the target is employed to attain acoustic intensity from a focused ultrasound transducer. Before visualization, the system is calibrated with a signal, which is recorded from the substrate when there is no target. The focused transducer, which transmits and receives echo signals from a very reflecting material, insonates and scans the local area below the polystyrene substrate keeping the focal point on the substrate's rear surface. The target is imaged with the reference material in the same field of view. During the acoustic impedance determination, the ultrasound pulse emitted from the ultrasound transducer or probe is captured by surface of the target such as tissue or cell after traveling through the substrate having a finite attenuation. Then, it is reflected off the surface of the target and substrate to return to the transducer. As a final step, the reflections from the target and the reference material are compared and displayed on a digital oscilloscope as an acoustic impedance map using Fourier Transform for the analysis of the sound field in the frequency domain. To figure out the acoustic impedance, this analysis in the frequency domain is used. The difference of the acoustic impedance of the target located in the substrate results in the difference of intensity of the reflected sound wave.

The reflection coefficient, which is due to a mismatch in acoustic impedance is shown in Equation 1.9. However, the acoustic impedance measured for the target is different from the target's real acoustic impedance. Below is the relation between the measured and actual acoustic impedance [70, 71]

$$Z_{s_a} = \frac{1 + \frac{A_s\left(Z_{S_t}, c_S, \theta_a\right)}{A_r\left(Z_{r_t}, c_r, \theta_a\right)} \frac{Z_r - Z_{o_p}}{Z_r + Z_{o_p}}}{1 - \frac{A_s\left(Z_{s_t}, c_s, \theta_a\right)}{A_r\left(Z_{r_t}, c_r, \theta_a\right)} \frac{Z_r - Z_{o_p}}{Z_r + Z_{o_p}}} Z_{o_p}. \tag{1.35}$$

in which Z_{s_a} accounts for the acoustic impedance measured for the target using Equation 1.9, Z_{s_t} represents the real acoustic impedance of the target, θ_a is the half aperture angle. Also, p, s, r and o mark the pressure wave, sample, reference and substrate, respectively. The ratio of the amplitude reflected from the sample to the amplitude reflected from the reference is given by $\frac{A_s}{A_r}$ assuming liquid-liquid interface with normal incidence.

1.3.3. Sound Speed Measurement Mode

The sound speed of a target is related to its stiffness. High sound speed value correlates to the harder target. Figure 1.12 shows data recording algorithm and reflected signals in sound speed measurement mode.

In this operation mode, the target embedded on a glass substrate is located upside-down on the microscope above the ultrasound probe. Ultrasonic wave transmitted from the probe is used upward towards the glass substrate. Ultrasonic wave first passes through the thin cut target (approximate thickness of 10 μm), which is in direct contact with the ultrasonic transducer via the coupling liquid such as distilled water. The wave reflects at the flat interface between the target-glass substrate and reflects from the front surface of the target. Thus, with this configuration, three separate wave forms emerge: the signal from the front surface of the target, the signal from the flat interface between the glass substrate and the target, and the reference signal from the surface of the glass substrate. However, these wave components cannot be

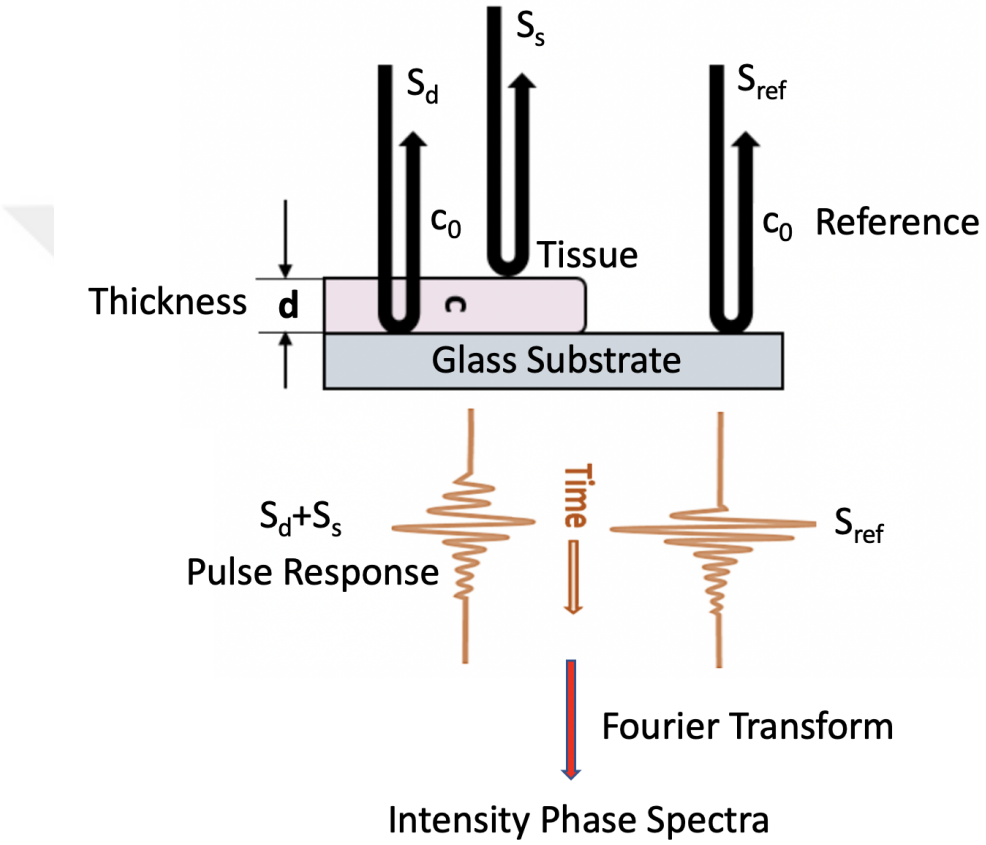


Figure 1.12. Signals in sound speed measurement configuration (reproduced from [72]).

separated into two independent signals in time-domain investigation. Hence, to study the interference between the reflections at the surface and at the boundary of the target and glass substrate, analysis in frequency-domain is conducted. The ultrasonic phases of these signals are then standardized and realized as a reflection wave from the glass substrate in a system computer. The differences in the reflected signals are used to calculate acoustic parameters. Operating SAM in sound speed mode, one can read acoustic intensity, sound speed, attenuation and thickness variables of the target under investigation [73, 74]. Analysis in frequency-domain is done by considering interference of the reflections. Through Fourier transforming the signals, intensity and phase spectra normalized by the reference signal are figured out. This analysis results in the speed of sound at the maximum and minimum points within the intensity spectrum. Assuming that one of the minimum and maximum points in the normalized intensity spectrum by f_{m} with the related phase angle ϕ_{m}, the phase difference between two reflections at the minimum point is given as $(2n-1)\pi$ and generates [73, 74]

$$\phi_{\min} + (2n-1)\pi = 2\pi f_{\min} \times \frac{2d}{c_0}. \tag{1.36}$$

in which d, c_0 and n account for the thickness of the target, speed of sound of the coupling liquid (mostly pure water), and a non-negative integer, respectively.

The phase angle $\phi_{\min}$, which gives the phase difference between the wave propagating the thickness of 2d in the target by sound speed c and the wave propagating within the coupling liquid by the related thickness with sound speed c_0, for minimum point can be described by

$$\phi_{\min} = 2\pi f_{\min} \times 2d \left(\frac{1}{c_o} - \frac{1}{c} \right). \tag{1.37}$$

For the minimum point, the thickness, d, can be calculated by solving Equation

1.36 and Equation 1.37 together,

$$d = \frac{c_0}{4\pi f_{\min}}[\phi_{\min} + (2n-1)\pi]\,. \tag{1.38}$$

The sound speed has the following form,

$$c = \left(\frac{1}{c_0} - \frac{\phi_{\min}}{4\pi f_{\min} d}\right)^{-1}. \tag{1.39}$$

As for the maximum point in the normalized intensity spectrum, the phase difference is $2n\pi$, providing

$$\phi_{\max} + 2n\pi = 2\pi f_{\max} \times \frac{2d}{c_0} \tag{1.40}$$

Changing $f_{\min}$ to $f_{\max}$ in Equation 1.37, and then solving Equation 1.37 and Equation 1.40, the thickness is equated by

$$d = \frac{c_0}{4\pi f_{\max}}\left(\phi_{\max} + 2n\pi\right). \tag{1.41}$$

SAM operating in sound speed measurement mode offers sound speed, thickness and attenuation knowledge. From the calculations above, ultrasound attenuation can be extracted through dividing amplitude by the frequency and the target thickness [75].

1.3.4. 80 MHz and 320 MHz Ultrasonic Transducers

In this dissertation, the SAM system was used with 80 MHz and 320 MHz single-element high-frequency transducers (Table 1.1 and Figure 1.13). The acoustic lens, which is able to transmit and focus the sound wave, and convert the electrical signal into pressure waves, is the heart of the SAM. Spherically focused ultrasound transducer is built by piezoelectric polymer, which is produced from polyvinylidene fluoride triflu-

oroethylene (PVDF-TrFE) thin film, for frequencies lower than 100 MHz since PVDF material are very convenient for high-frequency pulse-echo ultrasound imaging due to their bandwidth range and low mechanical impedance [2, 70, 76]. Moreover, backing application of 80 MHz transducer should possess high attenuation. The radius of the concave cavity gives the focal distance of the transducer.

The second kind of the ultrasonic transducers is designed for higher frequency, which is above 100 MHz. It is manufactured from ZnO piezoelectric material. Here, concave sapphire rod is put into function as a concave acoustic lens and piezoelectric material ZnO adhered to the bottom region. For frequencies above 100 MHz, ZnO piezoelectric polymer is found more suitable compared to PVDF [2]. The piezoelement material in the acoustic lens for both types of the transducers shows a variation in thickness as a respond to a brief electrical pulse. The sound wave transmits through a concave sapphire rod, and then is converted into a spherical wave, and focused on the focal point. Reflected waves are received by the same concave acoustic lens.

Table 1.1. Properties of 80 MHz and 320 MHz single-element transducers.

Transducer details	**80 MHz**	**320 MHz**
Central frequency	80 MHz	320 MHz
Bandwidth	50-105 MHz	200-400 MHz
Membrane type	PVDF	ZnO
Aperture diameter	1.2 mm	2.4 mm
Lateral Resolution	20 μm	4.7 μm

An ultrasound focused beam is yielded through the focused transducer by a specific depth of focus. The spherically curved shape of the piezoelectric material assists in the beam focusing [77, 78].

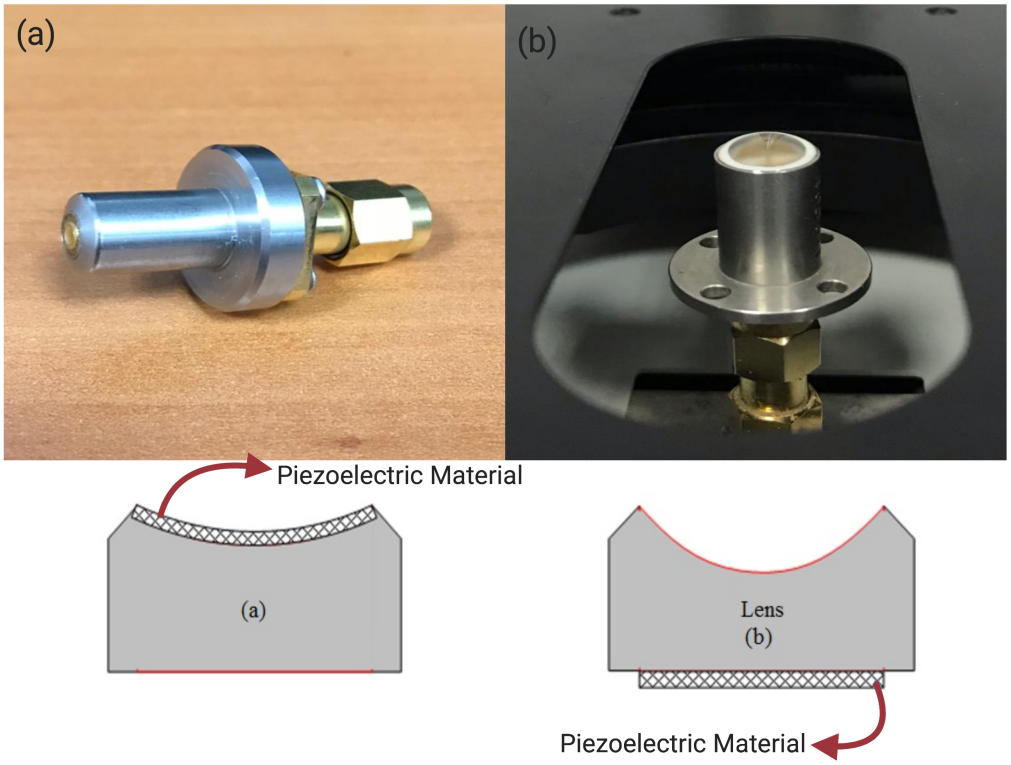


Figure 1.13. (a) 80 MHz ultrasonic transducer and its design with polyvinylidene fluoride (PVDF) thin film, (b) 320 MHz ultrasonic transducer and its design with piezoelectric polymer.

1.3.5. Beam Profile for a Single-Element Ultrasonic Transducer

There are two different zones of the sound field of the ultrasonic transducer for unfocused and focused conditions: near and far zones. As seen from the Figure 1.14, the near field is the region, which is close to the transducer face.

The distance for the transition from near field to far field is given by near zone length, N, and is a function of the frequency f of the transducer, aperture diameter D_a, sound velocity v in the target and wavelength λ. The definition is given by [80]

$$N = \frac{\text{diameter}^2}{4 \times \text{wavelength}} = \frac{D_a^2}{4\lambda} = \frac{D_a^2 f}{4v}. \tag{1.42}$$

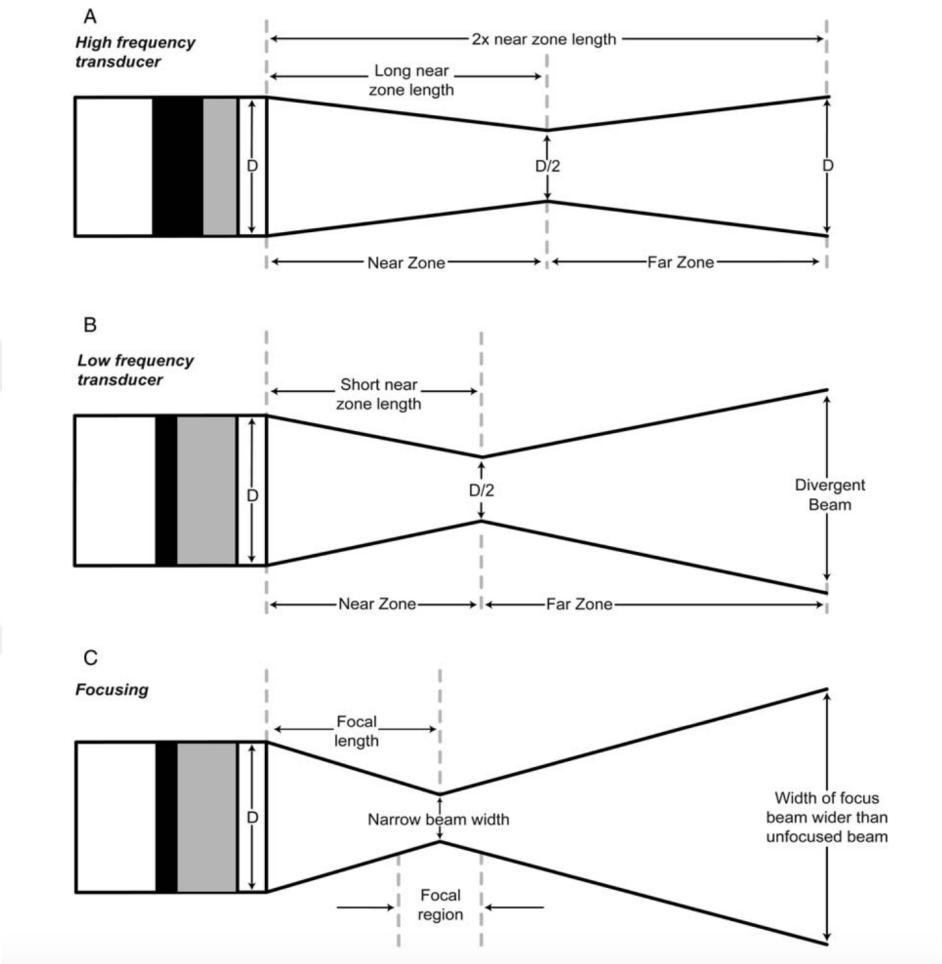


Figure 1.14. Schematic of near field and far field of the beam pattern formation of (A) high and (B) low frequency ultrasound transducer. (C) Focusing of ultrasound transducer narrows beam width [79].

The area outside the near field is named as the far field, in which the ultrasonic beam is more uniform and whole transducer can be considered as a point source. Sound wave is well-behaved with its maximum strength just outside the near field, see Figure 1.14. Beyond that area, the beam diverges, and the pressure starts decaying gradually by $\sim 1/z^2$ as the distance z from the transducer is increased [80].

1.3.6. Resolution In Ultrasound Images

In SAM, resolution has a key role in determining image quality, and it is organized into three classes: spatial, contrast and temporal resolution, see Figure 1.15. Spatial resolution defines the ability of SAM system to discern two designated reflectors in the target. Spatial resolution is divided into two parts: axial and lateral resolutions.

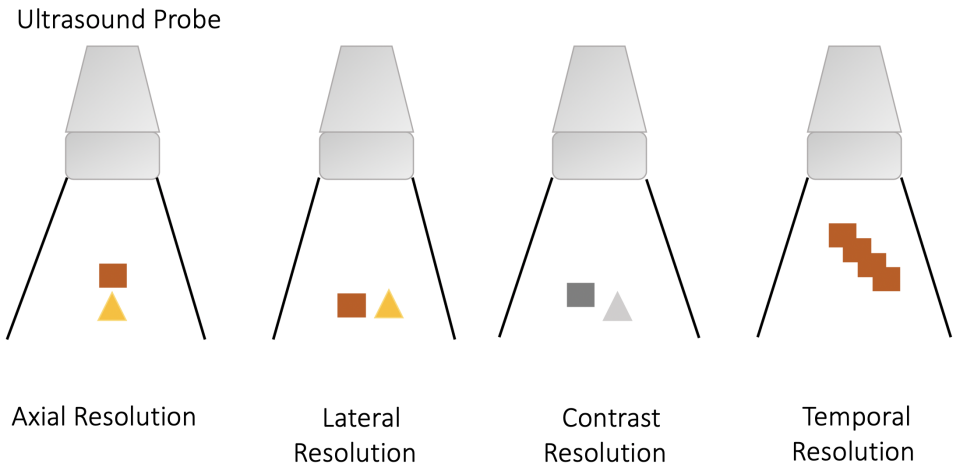


Figure 1.15. Illustration of ultrasound resolution types for a traveling ultrasound wave.

Axial (also named as longitudinal) resolution reflects the capability of SAM to distinguish two reflections in a minimum distance emerging from two points at different depth of fields, which are parallel to the sound beam propagation. Axial resolution is not dependent upon the imaging depth since the resolution is the same along the

beam for any structures. Frequency and wavelength influence the axial resolution. Mathematically, it is half of the spatial pulse length and the corresponding expression is

$$R_{\text{axial}} = \frac{4\lambda f_0^2}{D_a^2} \tag{1.43}$$

where R_{axial} is the axial resolution, f_0 is the focal length of the transducer, D_a is the aperture diameter, and λ is the wavelength.

Lateral resolution reflects the ability to distinguish two points that are located side by side and vertical to the propagation path of the ultrasound wave. It is defined by the focal spot diameter as follows

$$R_{\text{lateral}} = 1.03\lambda F \tag{1.44}$$

where F is the ratio of f_0 is the focal length of the transducer to aperture diameter D_a and specific to the acoustic lens, is the definition for the lateral resolution.

Contrast resolution is described as the capability of an ultrasound system to distinguish between the brightness (intensity) of the points on the image reflecting echoes of various amplitudes. Minor alterations determination in the target is based on the contrast resolution level [81].

Temporal resolution is the ability of the system to precisely follow mobile targets in time. It is also defined as frame rate. Temporal resolution is mathematically expressed as 1/(time to scan one frame). The pulse repetition period multiplied through the number of scan lines for a frame is equal to the scanning time for a frame. Temporal resolution is influenced by depth of field [82].

1.4. Physics of Optical Tweezers

Optical tweezers are scientific modalities that is formed using a highly-focused laser beam in order to non-invasively trap, manipulate (i.e. moving or rotating) and monitor nano and micrometer sized dielectric particles in three dimensions. The focused laser consists of a bundle of rays. Light carries momentum that is proportional to its intensity, and a change takes place due to light refraction and reflection at a particle according to Snell's law, and hence imparts a pressure on any surface when exposed [83]. Optical forces exerted on the designated particle are the consequences of the interaction between the laser and particle's refractive index mismatch with its surrounding. Namely, the optical forces are controlled through sample and surrounding medium refractive indices, laser power and particle diameter. These forces are on the order of piconewton (pN), which is a sufficient magnitude to convey motion on very small volumes such as microscale or nanoscale diameter scatterers. Using light momentum, a single focused laser beam optical trapping of dielectric particles was first introduced by A. Ashkin in 1986 [28]. This realization was the total force exerting on a dielectric particle, which can be used to manipulate the particle in three dimensions. It consists of a scattering and a gradient force. On the one hand, the net momentum variation of rays leads to a gradient force pointing towards the center of the focus. The gradient force moving particles towards the light axis emerged from radiation pressure and directed along the beam propagation. On the other hand, the scattering force arises in the direction of light intensity gradient, leading to a backward force towards the beam waist center. The gradient force (restoring force) functions against the scattering force to optically trap the particle near the tightly focused beam waist [28], as shown in Figure 1.16. From that time, optical tweezers or optical trapping have attracted considerable attention for investigations in biological and physical sciences.

This chapter departs from ultrasound imaging and catalogues the second main subject of the experimental investigation performed during this dissertation. In this chapter of the thesis, the related physics of optical tweezers and a dual-beam optical tweezers set-up that is used for optical stretching will be explained.

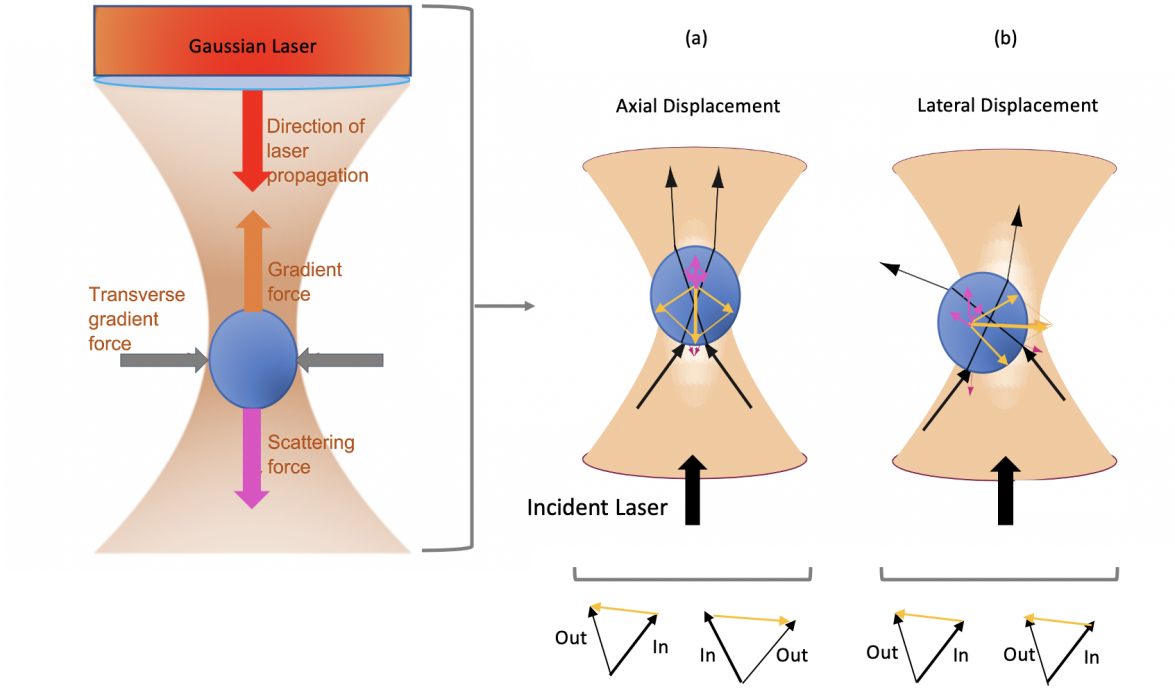


Figure 1.16. Illustration of gradient and scattering forces. (a) Axial and (b) Lateral displacements of the particle resulted from the gradient force on it. Intensity of the rays is indicated by different thicknesses.

In optical tweezers and optical trapping, the trapping force can be defined with different levels based on the size regime occupied. This size regime corresponds to the relative size of the target that is trapped, and the wavelength of the light used for trapping in a vacuum. Accordingly, there are three different approximations based upon the particle diameter to value the gradient and scattering forces on the particle. When the particle diameter is much smaller than the light wavelength ($r \ll \lambda$), Rayleigh scattering can be used, r is the particle radius and λ gives the light wavelength. On the other hand, when the diameter is much larger than the incident light wavelength ($r \gg \lambda$), Ray optics can be applied. When the diameter of the particle is equivalent to the light wavelength, Maxwell's equations must be considered with the appropriate boundary conditions. For this condition, a simplified Mie theory can be used. The intermediate condition, in which $r \approx \lambda$, needs a more complete, complex and common consideration [84–86].

1.4.1. Ray Optics Regime ($r \gg \lambda$)

When the ratio of the dielectric particle diameter to the wavelength is much larger than unity, ray optics regime is applied. In this case, diffraction can be disregarded. Optical forces arises due to the reflection and the refraction resulted from the difference in refractive indices of dielectric particle and its environment. Each time a single light impinging on the particle is diffracted and deflected, intensity hence its momentum will alter. In this alteration, the gradient and scattering forces are described by Fresnel reflection R and transmission T coefficients of the surface at θ_I [84].

$$F_{gradient} = \frac{n_m P}{c}\left[R\sin 2\theta_I - \frac{T^2\left[\sin\left(2\theta_I - 2\theta_R\right) + R\sin 2\theta_I\right]}{1 + R^2 + 2R\cos 2\theta_R}\right] \tag{1.45}$$

,and

$$F_{\text{scattering}} = \frac{n_m P}{c}\left[1 + R\cos 2\theta_I - \frac{T^2\left[\cos\left(2\theta_I - 2\theta_R\right) + R\cos 2\theta_I\right]}{1 + R^2 + 2R\cos 2\theta_R}\right] \tag{1.46}$$

with n_m surrounding medium the refractive index, P incident light power in the focus center, θ_I incidence angle and θ_R refraction angle.

1.4.2. Rayleigh Regime ($r \ll \lambda$)

As previously mentioned, in condition where the particle diameter is very small in comparison to the incident light's wavelength, the electric dipole approximation can be applied, and by that the particle can be supposed as an induced dipole in a heterogeneous electromagnetic field with a dipole moment [85]

$$\alpha = 4\pi n_m^2 \epsilon_0 r^3 \left(\frac{m^2-1}{m^2+2}\right) \mathbf{E} \tag{1.47}$$

where ϵ_0 is the dielectric constant of vacuum, m the ratio of refractive indices of particle to medium $m = \frac{n_p}{n_m}$, and $\mathbf{E}$ the electrical field.

The gradient force is proportional to the laser light intensity gradient ∇I. Using α, it is present as,

$$F_{gradient} = \frac{2\pi n_m r^3}{c} \left(\frac{m^2-1}{m^2+2}\right) \nabla I. \tag{1.48}$$

Apart from the gradient force, the scattering also plays an important role as in the ray optics regime with the wavenumber $k = \frac{2\pi}{\lambda}$ and the laser light intensity I in the focus [85]:

$$F_{\text{scattering}} = \frac{8\pi n_m k^4 r^6}{c} \left(\frac{m^2-1}{m^2+2}\right) I. \tag{1.49}$$

1.4.3. Dual-Beam Optical Tweezers

The efficiency of a single beam trap may only be determined by the objective and the laser power permits. Yet, this condition cannot be sufficient enough to trap a microbead at the balance due to exterior forces. Hence, to further increase trapping forces as well as decreasing the influences of reflection forces together with other exterior forces on the microbead, two tightly focused laser beams can be used. This doubles up the efficacy of the optical trapping. A dual-beam optical tweezers set-up used in this thesis adopts the simple concept of typical optical trapping, which is explained previously, using two optical tweezers. In this configuration, one of the traps is kept stationary while the other is steerable, which enables stretching biological matter by increasing the distance between two traps slowly. The details of the dual-beam optical tweezers will be documented in the study, which takes part in Chapter 4, for the assessment of the red blood cell deformability in radiotherapy treatment test groups.

1.5. Cancer Treatment

Cancer is one of the major health issues the world faces. Surgery, radiotherapy, chemotherapy and other medications (e.g. hormone therapy) are used to cure or shrink or stop a cancer, as shown in Figure 1.17. The combination of these treatment plans increases the effectiveness of the cancer treatment. Among these treatments, surgery has a key role in the cancer management. However, not all individuals are surgical candidates or not all tumors are operable due to their properties and inaccesible location in the body. Surgery is a very effective localized treatment for small-size tumor that have regular boundaries and have not hold the surrounding tissues or organs. Chemotherapy is a treatment using cytotoxic drugs to damage cancerous cells in the tumor and those circulating through the body. Radiotherapy is also a local treatment for tumors, which is not diffused throughout the body. Radiation therapy can be applied as a single treatment or in combination with other curative tools. It can also be used as a palliative treatment for the metastatic cancer patients. An increasing number of individuals having cancers are commonly and successfully treated by radia-

tion therapy, which uses ionizing radiation to kill or shrink the cancerous cells or solid tumors. Cancer radiotherapy delivers 25-40 Gy cumulative radiation doses of 2 Gy daily fractions over 5 to 8 weeks with a break at the weekends [1]. Fractionation of the cumulative radiotherapy doses has been experimentally tested, and it shows a more effective curing in comparison to single radiation doses. This is because such treatment plans offer tumor management by eliminating tissue toxicity. However, radiotherapy may damage normal tissues or organs around when it is applied to the tumor. Thus, novel advancements, such as stereotactic radiotherapy, are proposed and still under investigation to provide a irradiation, in which a tumor gets a high dose of radiation (e.g. 10 Gy in one fraction) and the neighboring tissues around it get a much lower radiation dose. This type of treatment may decrease the risks in the non-cancerous tissues or organs [87, 88].

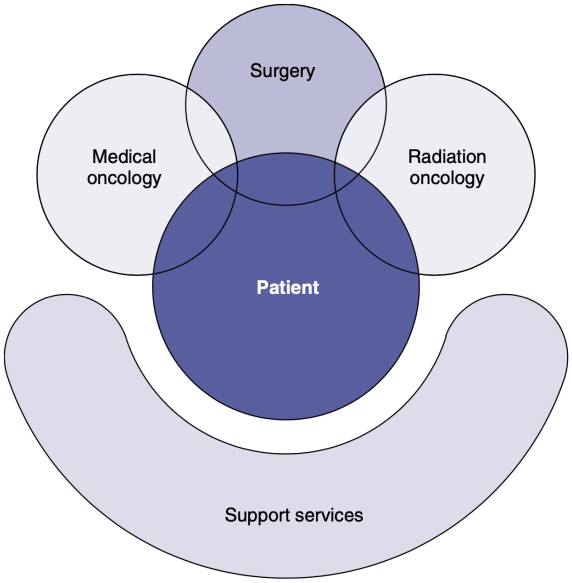


Figure 1.17. An illustration of multidisciplinary cancer treatments that the cancer patients receive during disease management [1].

1.5.1. Ionizing Radiation Interaction With Biological Medium

X-rays have played an important role in modern medicine with their invention by German physicist Wilhelm Conrad Roentgen since 1895. X-ray radiation in cancer treatment was first used on a 55-year old woman having inoperable breast cancer [1,89]. Two terms must be explained when considering radiation interaction with biological tissue: ionization and excitation. The radiation interacts with an atom in both terms. Ionization is defined as the ejection of an electron from its orbit around the nucleus of the interacted atom, which leads to a charged particle or ion. Individuals photons of X-rays having energies greater than 10 ev (electron volt) are defined to be ionizing radiation [1,89]. As for excitation, the electron in the outer shell of the interacted atom is oscillated or vibrated, but does not result in a complete displacement from the shell.

When radiation is incident on a cell, the ionizations can be direct or indirect [1]. The event sequences after radiotherapy exposure in humans can result in multiple reactions in a short or a long term duration, as cartooned in Figure 1.18. Radiation can cause detrimental influences on any molecule in the cellular environment, but damage to deoxyribonucleic acid (DNA) is highly probable due to the relatively densely ionizing nature of direct interaction by direct energy absorption. Moreover, the damage to the DNA molecule can also be resulted from the indirect effects, in which radiation interacts with free-radicals (chemically reactive species with an unpaired valence electron). Free radicals may attach to other free radicals and they constitute a new molecule such as hydrogen peroxide, which is thoroughly toxic to the cell. Indirect ionization can lead to damage to the DNA molecule mostly from radiolysis referring to splitting of H_2O, which is the first impact of any radiation treatment.

Radiobiology has evolved since Roentgen's discovery, and evaluated the biological fate of cells, tissues or organs following the absorption of energy from ionizing radiation. As previously mentioned, DNA in the nucleus has been mostly shown as the

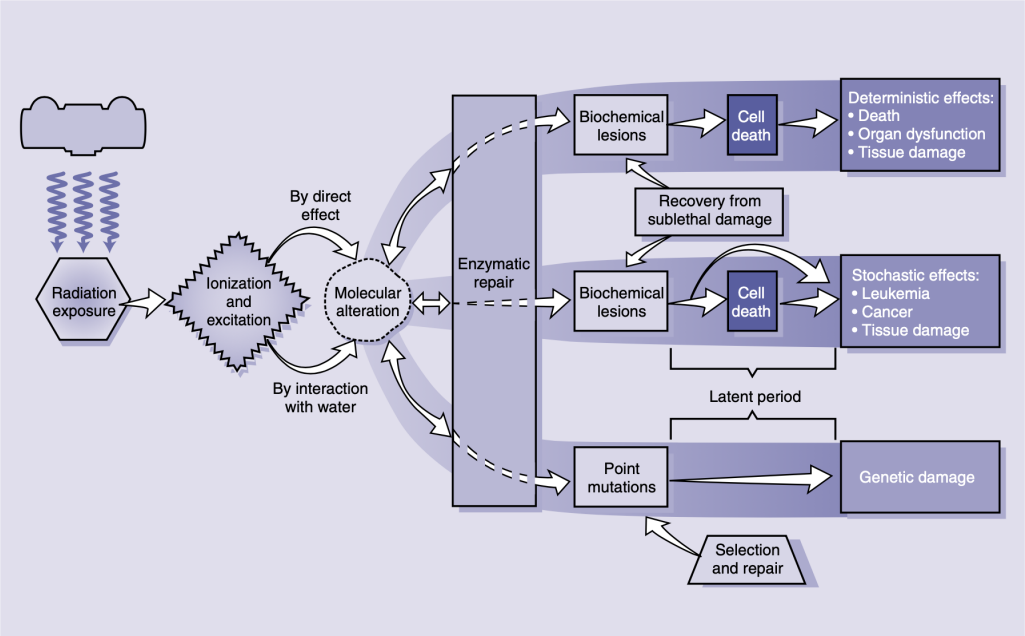


Figure 1.18. The event sequences after radiotherapy exposure in humans can result in multiple reactions in a short or a long term duration [1].

primary target for the ionizing radiation. However, irradiation selectively directed to the cytoplasm causes radiosensitivity in the cell, showing an initiation of cell signaling emerges from other organelles than the nucleus. In fact, radiotherapy operates directly on the membrane and confirms that plasma membrane shows an alternate path to DNA in radiation-modulated cell reactions [1, 90].

2. ULTRA-HIGH FREQUENCY ACOUSTIC IMAGING OF SODIUM ION DIFFUSION

2.1. Introduction

Sodium (Na^+), being the primary cation in extracellular fluids of living beings, is known to regulate bodily functions and biological processes. It also provides vital information about physiological and pathological states. Almost all living organisms could be unified to have the ability in sustaining the difference in sodium amount between the interior and the exterior compartments of their cells. Typically, sodium concentration of the viable cell interior is around 10-15 mmol/L while sodium concentration outside the cell averages to 140-150 mmol/L [91–93]. Organisms divide a considerable portion of the metabolic energy to sustain the sodium gradient. Since, this gradient has a crucial role in nutrient intake, production and transmission of action potentials, regulation of intra- and extracellular ions, and controlling of the cell volume [91–93]. Particularly, disruptions altering the sodium ion homeostasis are known to be major hallmarks of cautious complications in cell integrity and ion homeostasis. Therefore, accurate determination and monitoring of sodium dynamics hold the key to diagnosis and prognosis of many diseases such as cancer, stroke, kidney, heart diseases and multiple sclerosis (MS) [91–93].

A number of analysis and monitoring approaches have been conducted to investigate variations in sodium content. Flame atomic emission spectroscopy, atomic absorption, flow cytometry, ion-selective electrode (ISE) and neutron activation are some of the sodium assay techniques [94–96]. However, these methods may be harmful to biological samples like tissues, cell cultures, serum and urine when time duration is considered. Besides, they are far from being practical because of the fact that they lack actual quantifications, sufficient spatial resolution, interference-free and simple operating principles. Moreover, Sodium Magnetic Resonance Imaging (sodium MRI) offers visualization of the dynamic and static monitoring of sodium [97–99]. However,

although being a non-destructive and reliable method, low sodium concentration of tissues or cell populations (i.e cell interior 10-15 mmol/L and cell exterior 140-150 mmol/L) leads to limitations including low resolution (2-10 mm), low signal-to-noise ratio (around 20-40), long scanning times (10-30 minutes), which impede studies on exact sodium monitoring [99]. Also, this technique necessitates a compact tissue in a magnetic space. The current methods used to image or monitor sodium concentration within the biological surrounding have constraints and improvement is required for precise and reliable quantification. Therefore, further research is necessary to obtain direct, precise, sensitive/specific, simple analysis and monitoring of sodium level as well as improving current techniques. Acoustic measurement by Scanning Acoustic Microscopy (SAM), which uses high-frequency sound waves (80-400 MHz) to map elastic properties of the sample through the measurements of acoustic impedance and sound speed at microscopic levels without adverse mechanical effects [100], may be an alternative to these investigation tools. Since, in comparison to the previously mentioned techniques, it has the benefits of micrometer resolution, direct non-destructive monitoring capability, no requirement of a special sampling process, quick measurement (i.e. 2 minutes for 4.8 mm $\times$ 4.8 mm target) with an easy application [100] and applicability to bulk tissues [70, 101–104] as well as to cell populations [105–109].

2.2. Methodology and Analysis

2.2.1. Phantom Design and Sample Preparation

Agarose phantom is imaging specimen of known acoustic properties such as sound speed and acoustic attenuation coefficient and facilitates and quickens the development of the imaging systems with its easy preparation protocol and reasonable cost [110]. In light of all these, the ability of SAM in sodium content determination and monitoring was first tested in the agarose phantom before investigating the ability of SAM in biological surroundings such as live cell populations or tissues and serum. We prepared an agarose phantom using commercial agar powder and distilled water. We fixed the concentration at 2% (weight of agar powder (g)/100 ml distilled water) (w/v). The

swirled mixture of agar and distilled water was boiled up to a temperature changing between 80-90 °C. When the mixture cooled down to 70 °C, we poured it into the polystyrene petri dishes of diameter 4 cm and 8 cm and let it cool further down to room temperature ($25 \pm 1\text{C}^{\circ}$). The mixture was poured as a thin layer of thickness of 1 cm within the petri dishes for neglecting the effects of gravity. Note that, in the presence of an external force, such as gravitational force, it becomes harder to describe the diffusion of NaCl solution in the agarose phantom by the well-known Fick's law [111].

The range of physiological sodium concentration is limited, but disruptions affecting the ion balance may result in increases in the sodium level within the biological medium. Accordingly, we specified the range, which covers physiologically possible sodium content within biological mediums, between 130 to 350 mmol/L. The values of agarose/saline test phantoms of known sodium concentration were also considered [99]. The NaCl solution concentration C is defined in units of g/100 ml (w/v). In terms of percentages, the biologically possible sodium amounts correspond to the range of 0.8% to 2%. First of all, to get the general trend, we prepared low concentrations NaCl changing from 0.8% to 2% with increments of 0.2% and high concentrations ranging from 2% to 5% with increases of 1%. In the second part, 10% NaCl was prepared to quantify sodium diffusion within the agarose phantom for time durations in the order of hours (i.e. 1-hour) to give a better view of the study. Acoustic impedance values change ranging from 0.8% to 10% were quantified and the acoustic impedance values against previously mentioned sodium concentrations were plotted to illustrate the relationship.

We created a well of diameter of 7 mm in the polystyrene petri dish of diameter 4 cm, to deposit and liberate NaCl solution of a concentration within the biological range (130-350 mmol/L) [99]. The diameter of the dish for biologically possible sodium concentrations was selected because of the reason that the concentration gradient between the phantom (background) and the well leads to diffusion to be observed within a period of time in the order of minutes (i.e. 15 minutes). Then, we prepared another

phantom inside the petri dish of diameter 8 cm with a well of diameter of 14 mm to track very high total sodium content (i.e. 10%), which is not in the possible physiological range but induces diffusion process to be observed for a time span of hours (i.e. 1-hour). For both agarose set-ups, we used a dropper to pour a fixed volume of NaCl solution of any concentration into the well. Side and top views of the agarose phantoms structured for visualizing the sodium motility characteristics are shown in Figure 2.1.

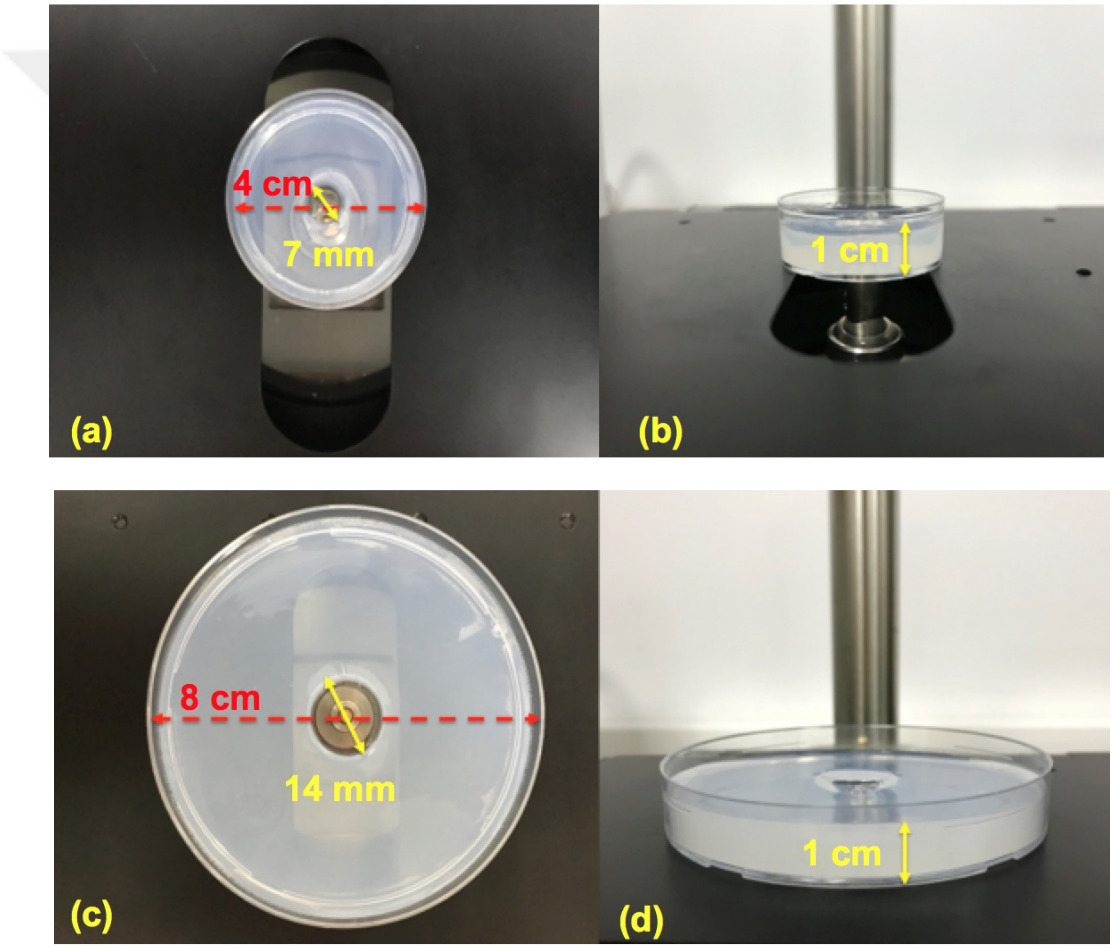


Figure 2.1. (a) Lateral and (b) top perspectives of agarose phantom of diameter 4 cm, (c) lateral and (d) top perspectives of agarose phantom of diameter 8 cm. The concentric wells of NaCl solutions are 7 mm (a) and 14 mm (c).

The total amount of NaCl solutions tested in this study remained constant through diffusion process, as indicated in Equation 2.1

$$\int_{phantom} Cdv = constant. \tag{2.1}$$

where C refers to the NaCl concentration in units of g/100 ml. We used the measurements of acoustic impedance at time intervals of 2 minutes to image and verify the diffusion of sodium ion in the agarose phantom.

2.2.2. Theory of Diffusion Process

Diffusion in a homogeneous medium is defined by Fick's first law, which relates the diffusive flux F to the concentration gradient as

$$\boldsymbol{F} = -D \cdot \nabla C, \tag{2.2}$$

where C is the concentration of the diffusing substance and D is the diffusion coefficient. It describes diffusion as a flow of substance resulting from the concentration gradient between media. As shown in Figure 2.1, the agarose phantoms initially included two concentric regions: A well and the background. The well was filled with NaCl. NaCl diffuses from its nest to the background due to the concentration gradient. The diffusion of NaCl in the agarose phantom follows the Fick's second law which states the change in concentration with time as given

$$\frac{\partial C}{\partial t} = \nabla \cdot (D \nabla C), \tag{2.3}$$

where t refers to time. There was no varying concentration along the z-direction within the agarose phantoms because of its structure. Therefore, we assumed that diffusion could be investigated in 2-dimensions (2D). Equation 2.3 can be solved using the separation of variables method for a disc of radius a on an infinite plane surface.

The corresponding result gives concentration C at radius r and time t as

$$C(r,t) = \frac{C_i}{2Dt} \exp\left(\frac{-r^2}{4Dt}\right) \int_0^a \exp\left(\frac{-r'^2}{4Dt}\right) I_0\left(\frac{rr'}{2Dt}\right) r' dr' \tag{2.4}$$

in which C_i refers to the initial concentration of the disc, t is time and I_0 is the modified Bessel function of the first kind of zeroth order. When $t > 0$, the maximum concentration of NaCl is observed at the disc's center, and this equation can be reduced to [112, 113]

$$C = C_i\Big(1 - \exp\left(\frac{-a^2}{4Dt}\right)\Big). \tag{2.5}$$

with the aim of defining diffusion of substances into large volumes.

2.2.3. Scanning Acoustic Microscopy

Here, we proposed a novel technique to quantify the diffusion of sodium ions into agarose phantom by time-dependent acoustic impedance monitoring at room temperature (25 ± 1C°). All measurements were performed with SAM. A photograph of the SAM system is shown in Figure 2.2.

SAM is a non-invasive and easy-to-operate technique capable of detecting variations in elastic features of samples under investigation. SAM can measure and map microstructure of the sample as alterations in sound speed and acoustic impedance profiles with no requirement of dyeing process. In SAM, an acoustic wave is generated by a piezoelectric transducer and focused onto a sample by a sapphire lens; then it is reflected and received by the same transducer. The intensity image of the reflection, which depends on the features of the sample, is transformed into the acoustic impedance of the sample or the speed of sound passing through the sample. 2D images at the microscopic level are produced by mechanically scanning the transducer along the X-Y axes below the sample. Regarding the characteristics of the sample (tissue or cell), the resolution of the system can be improved by changing the frequency of the

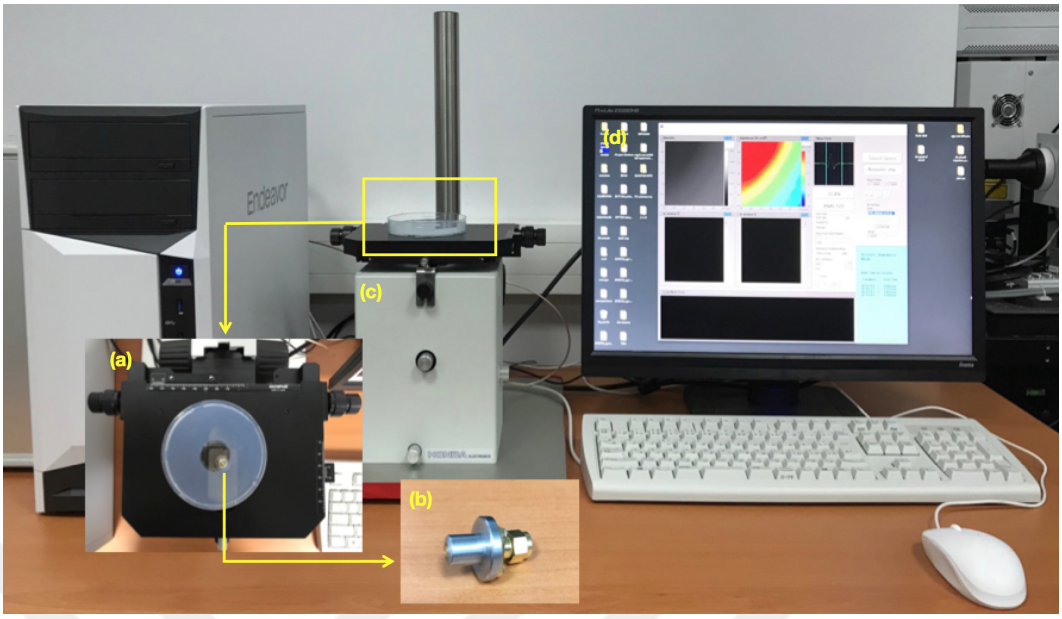


Figure 2.2. Scanning acoustic microscopy system in our laboratory. (a) Top view of the agarose phantom and the well used for monitoring NaCl diffusion, (b) 80 MHz transducer (PVDF-TrFE), (c) X-Y stage and (d) computer display.

transducer. Namely, as the frequency of the transducer increases, the spatial resolution will enhance [64, 100, 114].

Figure 2.3 illustrates a schematic diagram and two different measurement modes of SAM. SAM has two different measurement modes; speed of sound and acoustic impedance. The relationship between the sound speed value and elastic bulk modulus of a fluid-like medium is defined as $c = \sqrt{K/\rho}$, where c is the sound speed, K is the elastic bulk modulus, and ρ is the density [64, 100]. In sound speed mode, an approximately 10 μm thick flat cross-section of a specimen placed on a substrate is in contact with distilled water, which is introduced between the transducer and the sample to improve coupling. Reflections from the substrate and the specimen are collected to plot the speed of sound passing through the specimen. In acoustic impedance measurement mode, cross-sections of samples can be observed without unique slicing and staining processes, but the front surface of the sample must be as flat as possible to retain substrate-surface attachment properly. The acoustic impedance Z is defined as the

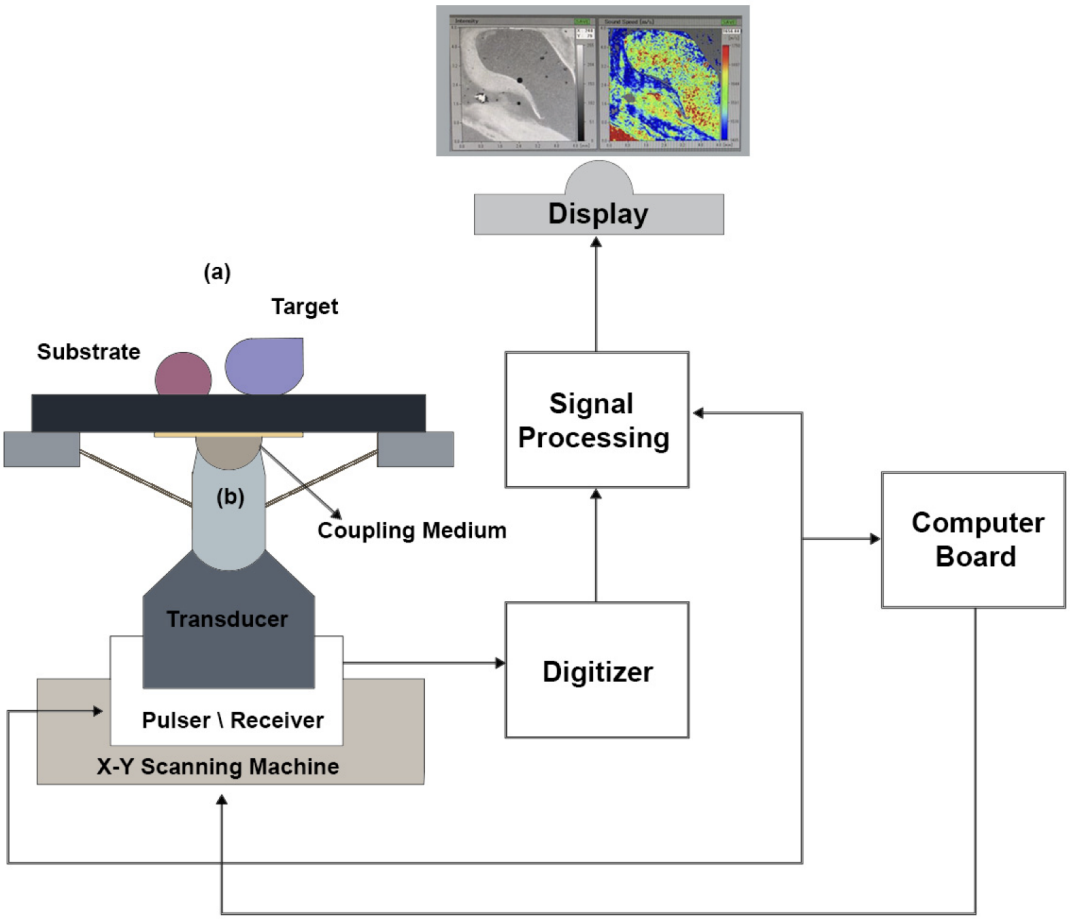


Figure 2.3. Schematic diagram of SAM consisting of five parts: Transducer, X-Y scanning machine, signal processor, digitizer and display unit for monitoring. (a) Acoustic Impedance measurement mode and (b) Sound Speed measurement Mode.

product of the density ρ and sound speed c and reflects the elasticity of the target and is formulated as Z = ρc [64, 100].

In the present study, a SAM system (modified AMS-50SI, Honda Electronics CO., Ltd, Japan), equipped with a transducer having 80 MHz center frequency, was tested in following the acoustic impedance changes induced by sodium ion diffusion within the agarose phantom over time. Accordingly, the system was operated in the acoustic impedance measurement mode. Here, 80 MHz transducer was selected due to the adequate resolution required for monitoring the cumulative motility, namely, displacement of the NaCl solution [69]. The lateral resolution of 80 MHz transducer was 20 μm. 80 MHz transducer, which had a PVDF-TrFE membrane, had a spot size of 17 μm and a focal length of 1.5 mm. 2D maps of samples were obtained by scanning the transducer placed on the X-Y stage. The polystyrene petri-dish filled with agarose phantom was positioned on the X-Y stage for each experiment. To raise impedance matching, we introduced a distilled water droplet (c= 1480 m/s, ρ= 1000 kg/mm^3) as a coupling liquid between the substrate and the transducer. Radio-frequency (RF) echo signals were received by the same transducer and acoustic impedance maps with 300 $\times$ 300 points were formed and plotted. The acoustic impedance data were then processed to analyze the diffusivity of sodium within agarose phantom. The maximum field of view (FOV) of the 2D maps of acoustic impedance was 4.8 mm $\times$ 4.8 mm, which has a scan increment of 16 μm. Scanning of the phantom in all experiments took about 2 minutes.

2.2.4. Theory of Acoustic Impedance Measurement Mode

Figure 2.4 demonstrates the acoustic impedance measurement in SAM. In this study, the acoustic impedance of distilled water and polystyrene substrates were measured as 1.5 $\times$ 10^6 N·s /m^3 and 2.37 $\times$ 10^6 N·s /m^3, respectively.

In the acoustic impedance measurement mode, the signal received from the object is compared with the reference signal. The acoustic impedance image is formed from

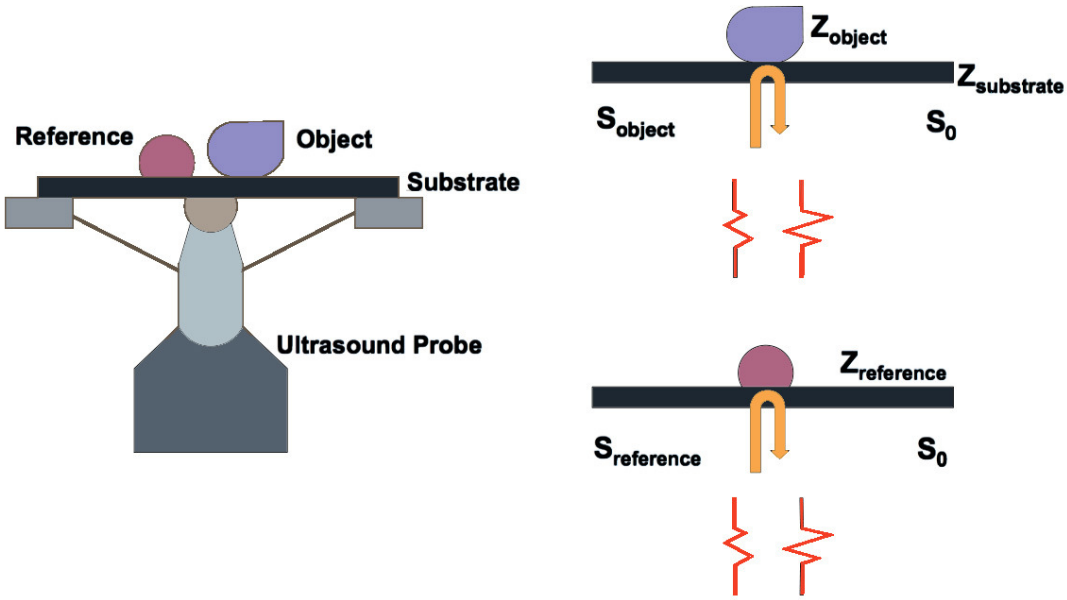


Figure 2.4. Illustration of acoustic impedance measurement mode. S_0 is the transmitted signal, S_{object} is the signal reflected from the object, $S_{reference}$ is the signal reflected from the reference and Z_{object}, $Z_{substrate}$, $Z_{reference}$ are the acoustic impedances of the object, substrate and reference, respectively

the reflected signal intensity map of the sample [115]. The reflected signal amplitude from the object under investigation S_{object} is formulated as

$$S_{object} = \frac{Z_{object} - Z_{substrate}}{Z_{object} + Z_{substrate}} S_0, \tag{2.6}$$

where S_0 is the transmitted signal from the ultrasound probe, Z_{object} is the acoustic impedance of the object, and $Z_{substrate}$ is the acoustic impedance of the substrate. The reference signal amplitude is formulated as in the following

$$S_{reference} = \frac{Z_{reference} - Z_{substrate}}{Z_{reference} + Z_{substrate}} S_0, \tag{2.7}$$

where $Z_{reference}$ accounts for the acoustic impedance of the used reference material. S_{object} and $S_{reference}$ are both directly measurable variables, however, S_0 is not. During data recording, the transmitted signal from ultrasound probe S_0 is accepted to have no alteration, then the acoustic impedance of the object can be written as

$$Z_{object} = \frac{1 - \frac{S_{object}}{S_0}}{1 + \frac{S_{object}}{S_0}} Z_{substrate} = \frac{1 - \frac{S_{object}(Z_{substrate} - Z_{reference})}{S_{reference}(Z_{substrate} + Z_{reference})}}{1 + \frac{S_{object}(Z_{substrate} - Z_{reference})}{S_{reference}(Z_{substrate} + Z_{reference})}} Z_{substrate} \tag{2.8}$$

The acoustic impedance maps of the objects are plotted on a display by applying the before-mentioned theory for each dataset.

2.3. Results

In our study, we showed the suitability of SAM system operating at 80 MHz with a lateral resolution of 20 μm in monitoring sodium ion concentration through time-varying acoustic impedance measurements in the agarose phantom. Before investigating the random behavior of sodium ions within the agarose phantom, we measured acoustic impedance values of the phantom and NaCl solutions separately. The acoustic impedance of the 2% agarose phantom was measured as $(1.52 \pm 0.04) \times 10^6$ N·s /m^3,

which was in agreement with the value obtained in a previous study [116]. We used polystyrene petri-dishes of diameters 4 cm and 8 cm to place agarose phantom for collecting reflected ultrasound signals properly during the measurements. Since, they have good hydrophilic features necessary for substrate-sample attachment.

We prepared the NaCl concentrations in and around the acceptable range of sodium content (130-350 mmol/L) regarding biological surroundings [99], therefore, the detection and monitoring the concentrations of NaCl ranging from 0.8% to 2% (g/100 ml water) were much more meaningful for the aimed study. SAM was able to measure acoustic impedances of NaCl with concentrations varying from 0.8% to 10% (g/100 ml water). Low concentrations ranging from 0.8% to 2% with increments of 0.2%, high concentrations ranging from 2% to 5% with increments of 1% and highest concentration of 10% were chosen to present the ability of SAM in quantification of sodium diffusion. Figure 2.5 illustrates the experimentally recorded acoustic impedance values for the adjusted sodium chloride concentrations.

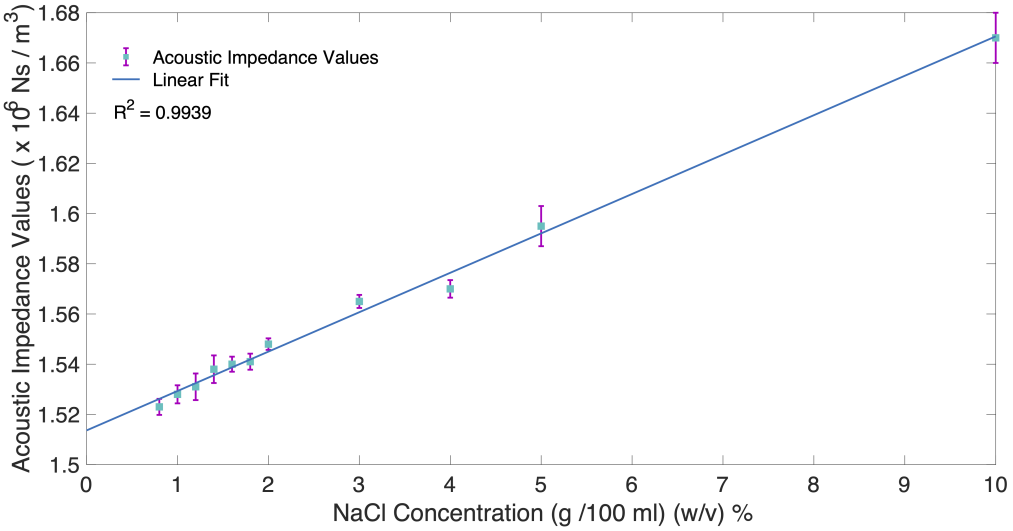


Figure 2.5. Acoustic impedance values of NaCl solutions as a function of sodium content.

A linear relationship between acoustic impedance and concentration of NaCl solutions was extracted within this range as follows

$$Z = AC + B \tag{2.9}$$

in which the acoustic impedance Z is defined in units of N·s /m^3, the NaCl solution concentration C is given in units of g/100 ml water. Constants A and B were found as 0.015 and 1.513, respectively.

In Figure 2.6, we showed acoustic impedance images of the 2% agarose phantom with diffusing NaCl solutions at concentrations of 1%, 1.5% and 2%, respectively. The acoustic impedances of these solutions were measured as (1.528 $\pm$ 0.0036) $\times$ 10^6 N·s /m^3, (1.539 $\pm$ 0.003) $\times$ 10^6 N·s /m^3 and (1.548 $\pm$ 0.0023) $\times$ 10^6 N·s /m^3. The diffusion for 1% NaCl could be monitored for approximately 14 minutes, since, clear contrasts between areas of sodium contents and the background vanished quickly after the diffusion started. Herewith, for the selected concentrations, time period of 14 minutes was chosen for comparing the images. Acquisition of each 2D acoustic impedance microscopic image took about 2 minutes with 300 $\times$ 300 sampling points. FOV was set to 4.8 mm $\times$ 4.8 mm for each image.

In order to see clearly the diffusion mechanics within the agarose phantom and avoid data fluctuations observed in lower concentrations (1% , 1.5% and 2%), we also prepared 10% NaCl solution which is above the biologically relevant range and measured that the acoustic impedance was (1.67 $\pm$ 0.01) $\times$ 10^6 N·s /m^3. Diffusivity of 10% NaCl solution was dynamically resolved by capturing acoustic impedance images every 2 minutes at 25 $\pm$ 1 °C till the agarose phantom and NaCl solution became isotonic, as shown in Figure 2.7. Real-time screening of diffusion by SAM was achieved through observing local variations in the acoustic impedance values in the agarose phantom. As can be realized in subsequent images of the diffusion process in Figure 2.7, the NaCl solution was spreading radially into the agarose phantom.

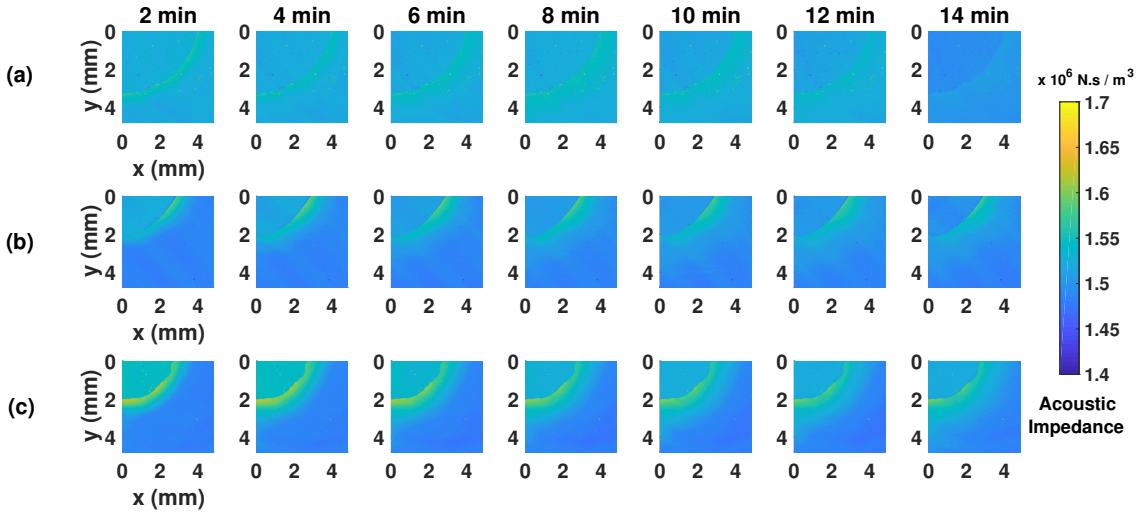


Figure 2.6. Successively obtained acoustic impedance maps of the 2% agarose phantom with diffusing NaCl solutions of concentrations of (a) 1%, (b) 1.5% and (c) 2%, in 14 minutes. The field of view was adjusted to 4.8 mm × 4.8 mm, covered by 300 × 300 pixels.

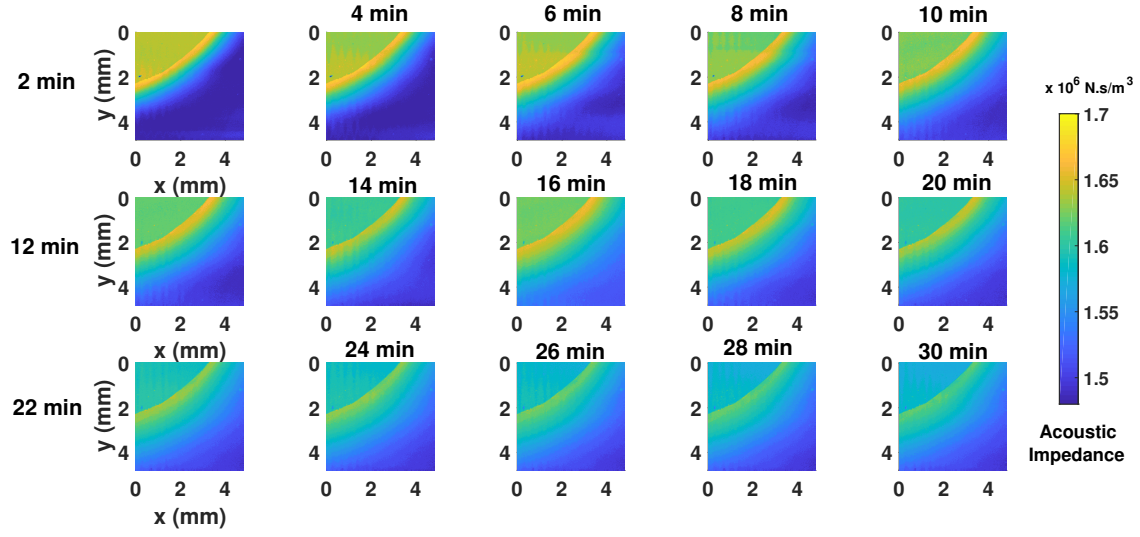


Figure 2.7. Subsequent images of acoustic impedance maps of the 2% agarose phantom with diffusing 10% NaCl solution. The field of view for each image was adjusted to 4.8 mm × 4.8 mm, covered by 300 × 300 pixels.

Figure 2.8 reflects the changes in acoustic impedance values of the phantoms resulting from 10% NaCl solution diffusion for selected time points. Multi-colored acoustic impedance images recorded by SAM were converted to gray-scale intensity images using MATLAB and alterations in acoustic impedance values with time and position were extracted from those gray scale images as shown in Figure 2.8. Moreover, acoustic impedance values inside the well, at the well-phantom border and within the 2 % agarose phantom were demonstrated as an inset in Figure 2.8. Trends reflecting the alterations in the acoustic impedance values for each time point were confirmed by literature findings for the NaCl diffusion within the agarose phantom. For 10 % NaCl, the diffusion process was followed for 1-hour timespan, however, approximately after 30 minutes, differences in acoustic impedances between NaCl regions, the phantom and the well-phantom border became less distinct due to the previously diffused ions and made the recording of the acoustic impedance images challenging. The acoustic impedance for time points were projected at every 10 points to increase the visibility of the data points.

The total amount of NaCl solution diffusing from its nest into the phantom was kept constant in all experiments. We used this constraint which was previously defined in Equation 2.1 for scaling of the maximum acoustic impedance values of 10% NaCl solution at selected time points within the region of interest of 4.8 mm $\times$ 4.8 mm, and then fitted to Equation 2.5 by means of Custom Equation Fit in MATLAB [113]. Figure 2.9 reflects all measured data points throughout the experiment from the time point of four minutes to thirty-two minutes at time intervals of 2 minutes together with theoretical trend using Equation 2.5. The maximum acoustic impedance value for each time point appeared to coincide with the theoretical fit. In course of time, they declined as expected from the diffusion. From the results of this study, it seems reasonable to conclude that spatially altering acoustic impedance values were in agreement with the diffusion process. We also extracted an experimental diffusion coefficient as 1.01 $\times$ 10^{-5} cm^2/s.

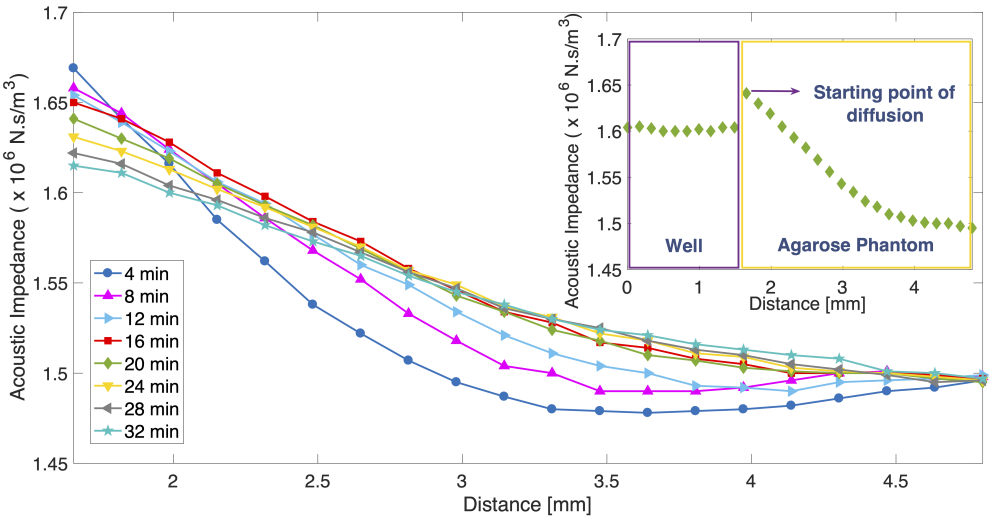


Figure 2.8. Comparison of changes in acoustic impedance values of the 2% phantom resulting from 10% NaCl solution diffusion for selected time points. Initial data points correspond to the acoustic impedance values at the well-phantom border. Acoustic impedance values inside the well, at the well-phantom border and within the phantom are demonstrated in figure inset.

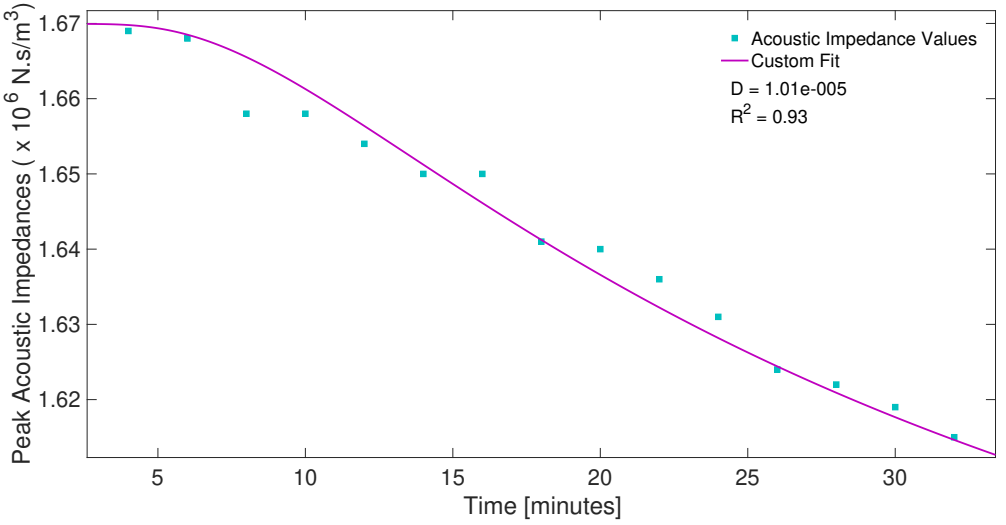


Figure 2.9. Decay trends of the maximum acoustic impedance values for 10% NaCl diffusion in the 2% agarose phantom. Experimentally obtained values illustrated by the green squares were fitted to Equation 2.5 producing solid line.

2.4. Discussion

In this study, we proposed time-dependent acoustic impedance imaging of sodium diffusion by SAM operating at 80 MHz with a lateral resolution of 20 μm. The suitability of SAM in sodium diffusion quantification was first tested within the agarose phantom as a proof-of-concept. Previous researchers have documented that imaging of sodium ion has a high potential to obtain characteristic information of disease-related variances about biological surroundings such as tissues, cells and body fluids. The normal intracellular sodium concentration of tissues is about 10 to 15 mmol/L, while extracellular sodium concentration is around 140-150 mmol/L. The range for the physiologically possible sodium concentration is limited, however, researchers noted that disruptions affecting the sodium ion homeostasis can lead to increases in the sodium level within the biological media [117–121]. Besides, the agarose/saline test phantoms for sodium quantification in sodium MRI were taken into account [99]. Therefore, in this study, considering the range of the physiological sodium concentration and the reference phantoms for sodium quantification in sodium MRI, we specified the sodium concentrations in and around the physiologically possible domain of sodium amount (130-350 mmol/L) within tissues (i.e. brain, muscle and cartilage) [99]. Additionally, in our study, the monitoring of sodium dynamics by SAM was first performed within the agarose phantom as proof-of-concept, since agarose phantom is a tissue-equivalent material of known acoustic features (i.e. speed of sound and acoustic attenuation coefficient) in ultrasound imaging. Also, its practical handling and easy preparation simplify and speed up the development of a system by decreasing the necessity of conducting human and animal experiment [110]. We determined the concentration of the agarose phantom at 2% for all the measurements in the study.

As well as the biologically meaningful range for the sodium concentration, we also studied the very high total sodium content of 10% which allowed us to study and verify diffusion of sodium ions through time-varying acoustic impedance measurements by SAM. Since variations along the gradient were more pronounced, the effects of fluctuations were less significant in data. Thus, this part of the study provided much more

precise information than lower concentration solutions (0.8% - 2%) to clearly see and quantify the sodium diffusion. We parenthetically remarked that the low concentration detections of NaCl from 0.8% to 2% were more critical with our technique. Thus, in the first part of our study, we prepared NaCl concentrations ranging from 0.8% to 2% with increments of 0.2% to test the ability of SAM in low concentration saline solution measurements. Then, to get a general trend, acoustic impedance values as a function of the NaCl concentrations varying from 0.8% to 2% with increases of 0.2%, 2% to 5% with increments of 1% and 10% were obtained by SAM. Figure 2.5 shows the plot of acoustic impedance values for NaCl solutions at previously defined concentrations. In the projected concentration domain in Figure 2.5, we found a linear correlation between concentration and acoustic impedance which is given in Equation 2.9. From the results, we concluded that the lowest concentration value for imaging and monitoring of the diffusion process by SAM functioning with 80 MHz transducer was equal to 1%. Throughout screening of the test phantom, we needed only acoustic impedance differences to track sodium ion dynamics. Namely, contrasts between the well and the agarose phantom regarding acoustic impedances were accurately imaged for the lowest saline solution concentration of 1%.

In this study, the diffusion process could be thoroughly followed for a time span of 14 minutes with the lowest NaCl concentration of 1%. Reductions of differences in acoustic impedances between the well and the phantom caused a decrease in the contrasts of two regions. After 14 minutes, the phantom was sufficiently saturated by saline solution as shown in Figure 2.6. Besides, Figure 2.6 shows a gallery of acoustic impedance images for 1%, 1.5% and 2% NaCl solutions recorded over a time span of 14 minutes to provide a comparison. Differences in acoustic impedance between the well and the background were sufficient to discern the well-agarose phantom boundary and ion diffusion for low concentrations (1%, 1.5% and 2%) in the time span of 14 minutes. With this, SAM permitted us to follow time-dependent variations in acoustic impedance resulting from sodium concentration activity within the agarose phantom with micrometer resolution at the concentration values adjusted in the research.

The acoustic impedance of 10% NaCl, which is relatively high concentration concerning its bio-availability, was measured as (1.67 ± 0.01) × 10^6 N·s /m^3 by SAM. Compared to the NaCl concentrations of 1%, 1.5% and 2%, we obtained sharper contrasts between the well and the phantom for approximately 30 minutes because of the significant concentration gradient between regions initially. Figure 2.7 shows acoustic images for 10% NaCl solution at consecutive times covering 30 minutes by acquisition step of 2 minutes. Acquisition of each 2D acoustic impedance image lasted in 2 minutes with 300 × 300 sampling points over an area of 4.8 mm × 4.8 mm. For the initial state of the experiment, a well-agarose phantom border was precisely distinguishable on acoustic impedance images for 10% NaCl solution. Due to sodium ion movements, the contrast started to fade out and border became less detectable because acoustic impedance values of both regions began to have closer values. After approximately 30 minutes, little contrast between the well and the phantom was observed. For 10% NaCl, we plotted acoustic impedance values as a function of position within the agarose phantom at consecutive times, as shown in Figure 2.8. The acoustic impedance data were analyzed from the time point of four minutes to damp out any source of undesired perturbations such as the effect of initial velocity which can result from the introduction of NaCl solution to the well. The data recording might be initiated at any instant, however, pure diffusivity will not be observed in time periods prior to four minutes [122]. Before introducing NaCl solution into the well, the acoustic impedance of the agarose phantom was measured as (1.52 ± 0.04) × 10^6 N·s /m^3. When the 10% NaCl solution was poured into the well, the sodium concentration, and likewise the acoustic impedance of the phantom linearly increased as reported in the study of Bhatnagar *et al.* [123]. The theory of diffusion states that with instantaneous sources, the diffusion process is not continuous but terminates [112]. As shown in Figure 2.8, experimentally obtained maximum acoustic impedance values within the region of interest of 4.8 mm × 4.8 mm were correlated with the theory of diffusion for instantaneous sources and exhibited similar decaying behavior at time intervals of 4 minutes. Over time, the acoustic impedance values monotonically decreased with distance from the well-phantom border due to decreasing amount of NaCl solution at a particular position [112]. At the beginning of the experiment, the gradient between

the acoustic impedance values of the well and the phantom was maximum, and accordingly, the curve showed a steep declination, which was due to the implementation of highly concentrated 10% NaCl solution. With increasing time, the gradient became less distinct compared to the initial trend due to previously located ions from the well into the phantom, and the curve became shallower. This was the expected trend for diffusion. We also observed fluctuations for some data points as a result of the composite gel structure of the agarose phantom. According to the study of Muhr and Blanshard [124], the structure of agarose gel was explained as a mesh, with water-filled spaces between polymer chains. Therefore, heterogeneous structure and impermeable vacancies of agarose phantom may result in unexpected acoustic impedance values. Moreover, as clearly seen in Figure 2.8, it did not change the general behavior of pure diffusion.

To quantify the diffusion for 10% NaCl solution within the 2% agarose phantom, using Equation 2.1, the empirically defined maximum acoustic impedance values for an image area of 4.8 mm $\times$ 4.8 mm were scaled and fitted to Equation 2.5 by Custom Equation Fitting Toolbox in MATLAB. Figure 2.9 shows the measured data points together with the theoretically plotted curve. The experimental acoustic impedance values were in agreement with the theoretical curve. As time elapsed, the maximum acoustic impedance values for each time point within the field of view of 4.8 mm $\times$ 4.8 mm decreased, as expected from the diffusion. We extracted a diffusion coefficient of 1.01×10^{-5} cm^2/s from Figure 2.9. In the study of Schantz *et al.* [125], NaCl diffusion was analyzed within approximately 1.5% agarose phantom. They used a 2 g of agar powder for 100 ml water, but also stated that because of moisture in the phantom, the actual concentration was almost equal to 1.5%. The diffusion coefficient in our study was calculated to be on the order of 10^{-5} cm^2/s, which agrees with the diffusion coefficient previously reported by Schantz *et al.* [125]. Therefore, we can conclude that time-varying acoustic impedance determination by SAM is a valid method to substantiate the sodium diffusion within the agarose phantom.

As a future work, we plan on monitoring the sodium activity within the concentration range of cell interior (10-15 mmol/L) [91], which would help to distinguish intracellular and extracellular chambers and offer information about the intracellular environment. Moreover, in our work, we conducted all the experiments within the diffusion phantom since fresh tissue and cell culture investigations were not subject to this study. Before performing the sodium imaging in live tissues and cells by SAM, we first tested our idea in the agarose phantom to check whether time-dependent acoustic impedance measurements of NaCl diffusion by SAM is valid or not. Hence, our first goal for this investigation was to show and prove the ability of SAM in sodium ion dynamics monitoring by time-dependent acoustic impedance measurements within the agarose phantom which has been used as a tissue substitute in ultrasound imaging for a long time [110]. One of the reasons why we chose the agarose phantom was that agarose phantoms have been used in ultrasound imaging for a long time for the development and characterization of the imaging systems and algorithms alongside its practical handling and easy preparation [110]. Secondly, there are similar studies in literature in which agar phantom was used to study sodium ion monitoring. For example, using agarose gel phantom and NaCl diffusion, similar experiment was conducted by using magnetic resonance electrical impedance tomography (MREIT) [113]. Thus, agarose phantom set-up was the first design that we planned for monitoring of sodium ion dynamics by SAM. On the other hand, visualization of sodium by SAM in complex surroundings such as *ex vivo* tissues and *in vitro* cell populations will be challenging due to the non-homogeneous nature of them. Yet, through considering both the similarity of the agarose phantom to tissues and our findings, we believe that one may get similar behavior for the acoustic impedance and concentration relationship as given in Figure 2.5 within the intricate biological media (i.e., tissues or cell populations), as well; but this necessitates a well-thought design, optimization of the experimental conditions and specific analysis of the experimental data for the extraction of sodium ion dynamics. To illustrate, these cases, particularly cell population and serum studies, may require higher frequency ultrasonic transducers of > 320 MHz which could provide the resolution that is capable of cellular imaging (i.e., around 5 μm at 320 MHz). Future studies, which take these conditions into account, will be designed for

determination and monitoring of sodium ion dynamics in the biological environment.

As was pointed out in the introduction of this study, several techniques have been applied to the measurement of sodium level such as flame photometry, atomic absorption spectrophotometry, flow cytometry, ion selective electrode and neutron activation [94–98]. However, in spite of their reasonable ability to determine sodium level, all these options have quite a few shortcomings which may affect clinical applications adversely. These shortcomings comprise inadequate accuracy, indirect measurement, destructive to the integrity of the sample under investigation, laborious sampling and complicated machinery. In addition, Sodium MRI offers non-invasive quantification of sodium content [99], but demands compact tissues in a magnetic field and long scanning time (10-30 minutes). The low physiological amount of intra and extracellular sodium ion (10-15 mmol/L and 140-150 mmol/L, respectively) result in low resolution (2-10 mm) and low signal-to-noise ratio (around 20-40) [99]. In light of all these, using SAM would be a very worthy addition for sodium concentration imaging and monitoring. In this study, we claimed that time-dependent acoustic impedance measurements of sodium concentration activity using SAM with 80 MHz ultrasonic transducer with a lateral resolution of 20 μm has a vast amount of benefits over previously aforementioned sodium analysis methods. Over clinically proven sodium monitoring tools, the first advantage of SAM for imaging and monitoring of sodium ion dynamics is that it is relatively fast technique in which data acquisition of 2D acoustic impedance images with an area of 4.8 mm $\times$ 4.8 mm containing 300 x 300 sampling points takes about 2 minutes. Also, the attractiveness of SAM is that it offers micrometer resolution (around 20 μm at 80 MHz) alongside easy-to-perform and direct monitoring. Further, acoustic impedance measurement of sodium ion dynamics by SAM is a non-destructive monitoring tool whereas sodium assays measuring total cell sodium level such as flame photometry, atomic absorption spectrophotometry and neutron activation destroy the samples. Accordingly, the non-destructive nature of SAM is an advantage when the sample under investigation is desired to be used for following observations such as light microscopy analysis. Another advantageous property of SAM is the ease of sample preparation and hence it avoids inducing any mechanical changes in the samples due

the specific sampling process (i.e. staining or fixation) [114]. Thus, to overcome artifacts caused by alterations due to sample preparation, acoustic impedance measurement through SAM for the imaging and monitoring of sodium ion within biological media such as tissue, cell populations or serum may be useful. With this study, we showed that SAM shows a promise as a sodium monitoring tool.

In this investigation, we focused on monitoring of sodium diffusion since sodium is a vital component of living organisms and alterations in sodium ion homeostasis are known to be fundamental indicators of cautious complications in the integrity of ion and cellular balance. In light of this information, in future, the success of SAM in quantifying sodium concentration activity by time-dependent acoustic impedance measurements could be extended to the non-destructive, interference-free and easy-to-operate marker to follow dynamic processes such as the interaction of chemotherapy treatment with the tissue or cell populations *in vitro*.

3. ACOUSTIC DIAGNOSIS OF RADIOTHERAPY-INDUCED EFFECTS ON ELASTICITY OF HUMAN TEETH

3.1. Introduction

Head and neck cancers represent an inhomogeneous group of malignancies of the upper aerodigestive tract. This kind of cancer is seen at high frequencies of 500.000 new cases in a year [126]. Radiotherapy is prescribed to treat individuals with head and neck cancers. It is also used as a palliative together with chemotherapy drugs for malignancies, which are not suitably operated on. Radiotherapy can result in severe reactions of the oral cavity, though it aids healing and maintain the nature of tissues [127]. Individuals are principally treated by the radiation doses up to 60 Gy divided into 2 Gy fractioned daily doses, where the tissues of oral cavity, salivary glands and mandible are being irradiated [128]. According to the studies, individuals subjected to radiotherapy for head and neck cancers may encounter direct and indirect outcomes [129]. Alterations in salivary gland composition, candidiasis, vascular variations, oral mucositis and necrosis of soft tissues could originate during or in the first days or within months or years after the radiotherapy [129]. Apart from indirect effects, radiation is also known to directly damage the dental tissue to lose its structural identity through the reactions of variations in microhardness of enamel and dentin, elastic modulus, crystalline and dentin-enamel junction morphologies and matrix metalloproteinases (MMPs) [130–132]. Literature comprises a vast amount of investigations on histological, chemical, mechanical and morphological alterations on teeth subjected to ionizing radiation to gain knowledge for the causes of radiation therapy-induced effects [133–144]. Nevertheless, non-physiological conditions of these investigations extensively have limitations which may be harmful to the nature of the sample through exceeding the characteristics elastic limit [135]. However, the findings are still controversial, and thereby pathomechanism of complications in human teeth at microscale after radiation therapy is still ambiguous. In the last several years, re-

searchers have focused on ultrasound for the inspection of hard tissues (i.e. teeth and bone) with the benefits of non-invasive, non-ionizing and non-harmful design [145–147]. In our recent proceeding study, we have also tested the applicability of SAM in tooth characterization after radiotherapy [148]. Current state of the art lacks diagnostic tools and has not well-developed. Thus, this study was motivated by the desire to suggest a hand-held tool which might enhance our understanding about micromechanicsm of the human tooth. It aims to show the applicability of 320 MHz SAM in the evaluation of the tooth alteration at the micrometer level following radiotherapy.

3.2. Methodology

3.2.1. Tissue Selection and Preparation

After review and approval of the proposed investigation through Ethical Committee of Kartal Doctor Lutfi Kirdar Education and Research Hospital, Ministry of Health, Istanbul with an approval number of 2018/514/18/9, human third molars of individuals 18 to 50 years old were collected by informed consent from Yeditepe University Faculty of Dentistry between September 2018 and May 2019. For this prospective study, of the initial extracted 65 human molar teeth, we included 45 (n=45) teeth homologous to each other due to structural similarities. The established inclusion criterion was caries-free teeth. We excluded 20 teeth since they had cracks and fractures, presence of caries, appearance of metallic restorations, endodontic treatment. The extracted sound human teeth were stored in distilled water changed at 37C° to mimic mouth moist. The roots and debris were removed. The teeth were bisected longitudinally by saw microtome (IsoMet 1000, Buehler) and then the surface of the remaining sections comprising enamel and dentin were polished (Phoenix Beta, Buehler) with a waterproof abbrasive paper of 1200 grit to attain a smooth surface to avoid superficial scattering of the sound waves. The thickness of the polished samples were approximately 1 mm. In our study, there is no requirement for the tooth sample to be thin sliced (i.e. 10 m), stained and fixed for the visualization. The teeth were distributed into 6 groups (n=9) in accordance with the irradiation doses: control, 2 Gy, 8 Gy, 20 Gy, 30 Gy and 60 Gy.

The samples for each group were saved for further investigation in Scanning Electron Microscopy (SEM).

3.2.2. Irradiation Design

Teeth samples were irradiated with 2 Gy, 8 Gy, 20 Gy, 30 Gy and 60 Gy doses in single fraction by a clinical linear accelerator (LINAC) (Elekta Versa HD, Elekta, Crawley, UK). 6 MV flat which has a dose rate of 600 cGy/min at dmax and unflattened photonbeams used which has a dose rate of 1200 cGy/min. All teeth were located in the 35 mm polystyrene petri dish. Irradiations were conducted with the positioned samples submerged in a custom-made rice phantom to achieve homogeneous dose distribution to the dishes as well as to simulate body. Before irradiation, the rice phantom was scanned through Computed Tomography (CT) with a slice thickness of 2 mm. The petri dish was deliniated as a Gross Tumor Volume (GTV). The dose distribution of the experimental design was acquired by Monaco Treatment Planning System. Figure 3.1 shows details of the irradiation procedure for the polystyrene petri dish which was located within the rice phantom.

The polystyrene petri dish was determined as a Gross Tumor Volume. The GTV was conformed 95/100 (95%) by prescribed doses using anterior-posterior/posterior-anterior (AP/PA) radiation fields, and Motor Unit (MU) calculation was done by collapsed cone algorithm by Treatment Planning System (Monaco 5.11.02v, TPS). Using 10 cm $\times$ 10 cm fields the number of monitor units were calculated by collapse cone calculation algorithm to consider heterogeneity to give the prescribed radiation doses that were 2, 8, 20, 30 and 60 Gy to the dental tissues located in the polystyrene petri dishes. Before irradiation of the dishes, output of LINAC was corrected to ensure dose differences at dmax smaller than 2% differences according to TRS 398 [149]. Irradiation doses of dishes were confirmed for each experiment setting through 0.6cc farmer type ionization chamber. The position accuracy of the dishes within the phantom were checked for each irradiation through comparing Digital Reconstructed Radiography (DRR) images created by TPS and kilo-voltage (kV) images obtained by kV system

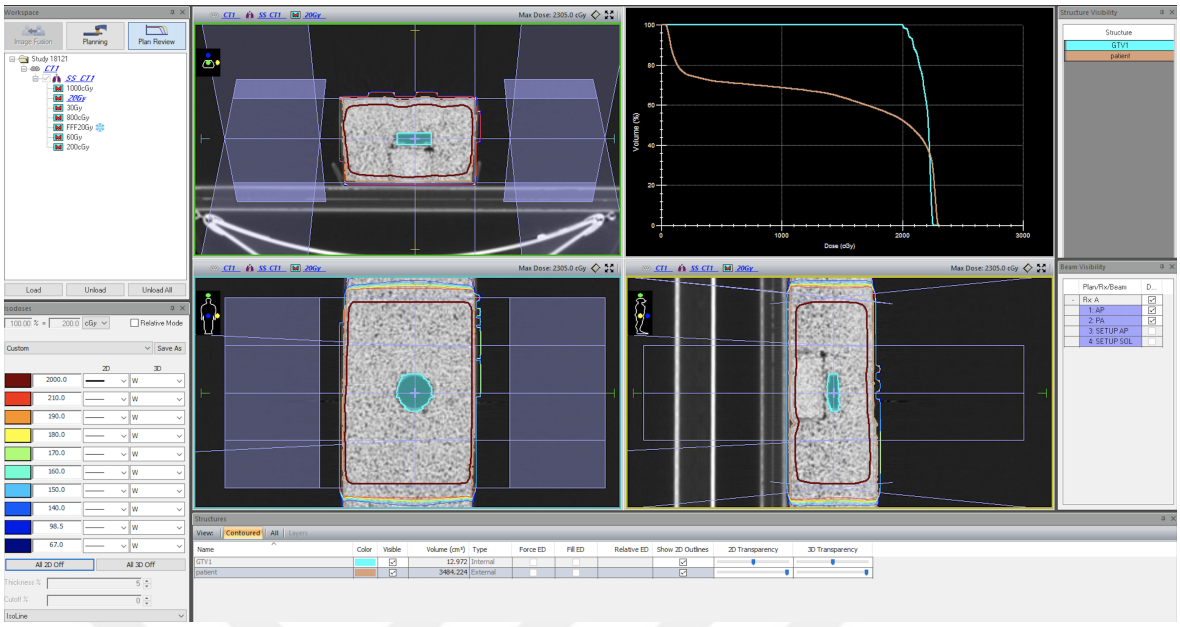


Figure 3.1. Details of the irradiation procedure for the polystyrene petri dish located within the rice phantom.

of linear accelerator. Before each treatment the position control of the phantom using kV-kV images was controlled to ensure that the polystyrene petri dish was located within the same region with the tomography planning.

3.2.3. Scanning Electron Microscopy (SEM) Analysis

For the SEM analysis, a sample from each irradiated group was used to image. In total, 6 specimens were visualized from the enamel and dentin regions. These samples were divided into groups in accordance with the radiation dose applied (control, 2 Gy, 8 Gy, 20 Gy, 30 Gy and 60 Gy). A sample from each group was used to obtain images and employ qualitative analysis Samples were positioned on aluminum stubs, covered by a thin layer of platinum for 15 minutes, and imaged using a FEI-PHILIPS XL30-ESEM-FEG.

3.2.4. Statistical Analysis

Statistical differences for acoustic impedance records were conducted through using Student t-test succeded by Mann-Whitney U analysis in GraphPad Prism 8 (GraphPad Software, San Diego, California) ($p < 0.05$), while SEM images were assessed qualitatively. All data were given as the average ± Standard Deviation (SD).

3.2.5. Ultrasound Data Acquisition by 320MHz SAM and Analysis

For the measurements of acoustic characteristics of dental tissue before and after *in vitro* irradiation, we used 320-MHz SAM (AMS-50SI, HONDA ELECTRONICS CO., LTD, Toyohashi, Japan) in pulse-echo mode to directly measure sample reflection coefficient and, therefore acoustic impedance. The schematic of principle of SAM is given elsewhere [70]. Distilled water was applied as a couplant between transducer and the sample. A radio-frequency signal produced by way of a transmitter reaches to the piezoelectric transducer of the 320 MHz acoustic lens yielding sound waves. The sound waves move through a sapphire rod, and then are converted to spherical waves and focused on the surface of the sample by the help of an acoustic lens. Reflected acoustic waves by the sample are collected through the same acoustic lens and then turned to a radio-frequency signal by the transducer, and transmitted to a circuit of video-processor. The amount of reflected sound wave is directly comparable to the reflection coefficient:

$$\mathrm{R} = \frac{Z_t - Z_w}{Z_t + Z_w} \tag{3.1}$$

in which Z_t and Z_w the acoustic impedance of the teeth samples and the coupling agent water, respectively. The acoustic impedance (Z) is related to the elastic features of the sample and expressed as the product of mass density ρ and compressional wave c_p and commonly defined in MRayl (1 Rayl = 1 kg $\mathrm{m}^{-2}\mathrm{s}^{-1}$).

The acoustic impedance of the coupling liquid is used to confirm the calibration curve in the following equation [70]:

$$\mathrm{Z} = \rho v = [\rho C_e]^{1/2} \tag{3.2}$$

where ρ is the density, C_e is the elasticity coefficient, and v is the acoustic velocity of the sample under investigation. If the density of the embedding material is kept constant during measurement, the variations in acoustic impedance will give the variation of tissue elasticity. The reflection coefficient is equivalent to the signal amplitude and establishes the brightness of the image. Higher acoustic impedance of the dental tissue sample accounts for a brighter image since the acoustic impedance of coupling liquid water is unchanged.

This study was conducted using specially constructed SAM for biological applications. It enables observation of the morphology and provides quantitative measures for biomechanical features of biological samples in the frequency range varying from 30 to 500 MHz. To visualize the samples, the microscope is equipped with a spherically focused broadband transducer with a central frequency 320 MHz since the azimuthal resolution has to be at least the same size of the sample for enamel prisms and dentin imaging [64]. The resolution is about 4.7 μm sufficient to visualize the microstructure details of dental tissue. The transducer includes a flat piezoelectric layer of ZnO with crystallographic orientation connected with a sapphire lens. From the bottom of the lens, its focal length was 0.50 mm with the spot size of 4 μm. The central frequency was 320 MHz, and acoustic pulse wave ranging from 200 to 400 MHz was focused on the junction between the tooth and the substrate, and passed through the substrate. The 320 MHz transducer was positioned under the sample on the X-Y stage where linear servo motors drove the both X-scan and Y-scan. Polystyrene petri dish holding the tooth sample was placed above the transducer as shown in Figure 3.2 (created by BioRender), in which the front surface of the tooth was in contact with the transducer. Acoustic impedance of tooth was figured out using water as a substrate. The acoustic impedance of water as a substrate was 1.5 MRayl. Each tooth sample was

irradiated and scanned along the X-Y axes in a frame with 300 × 300 pixels. pixels. Two-dimensional distribution of the acoustic impedance was obtained and the field of view was 4.8 mm × 4.8 mm with a 16 μm scan step. The treatment time for each tooth scan took 2–3 min. Eight pulse echo sequences were selected for each experiment to reduce noise.

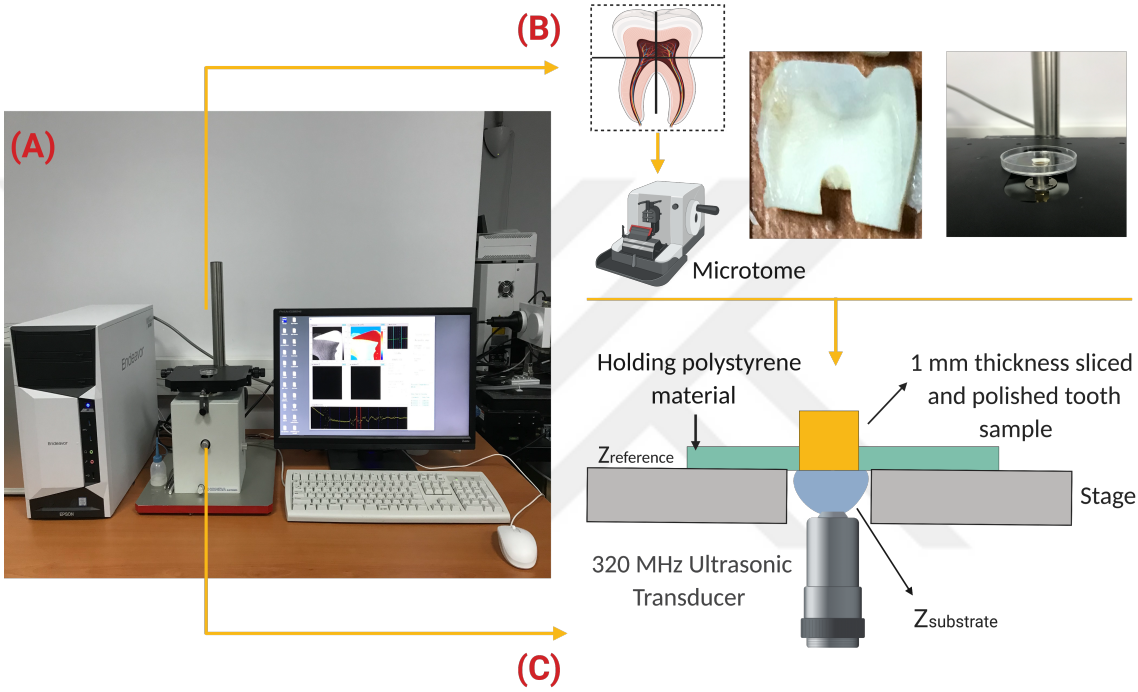


Figure 3.2. (A) Scanning Acoustic Microscopy (SAM) System (B) Schematic representation of tissue sectioning (cutting points from enamel and longutidunal direction) and localization for the measurement. (C) Schematic representation of acoustic impedance measurement mode. In this case, water is used as substrate. Tooth sample is not necessarily thin sliced. Just front surface must be polished to be very flat for the acoustic impedance measurement of the tooth sample

3.3. Results

3.3.1. Acoustic Impedance Imaging

Figure 3.3 displays non-uniform biomechanical features of dental tissue showing up alterations in the intensity of the reflected acoustic signal in bulk enamel and dentin for non-irradiated and for each radiation dose applied in this study. It can be seen that investigation at 320 MHz permitted to discern enamel and dentin as well as many microstructure details to be visualized in acoustic images. In the acoustic impedance image, SAM clearly monitored two-dimensional color distribution of the acoustic impedance of the caries-free human molars. The gradation color variations from control to 60 Gy two-dimensional images showed the course of the acoustic impedance values with respect to radiation doses. Enamel and dentin regions for non-irradiated group were composed of higher acoustic impedance values than those of the teeth of irradiated groups of 2 Gy, 8 Gy, 20 Gy, 30 Gy and 60 Gy. The softened dental tissue due to the ionizing radiation appeared in the image as bright orange areas of various tints relating to regions with a lower intensity of the acoustic signal.

For acoustic impedance analyses, in total, 45 sound human third molar were used. These samples were divided into groups, each of which contains 9 teeth, according to the radiation dose subjected. Table 3.1 and Figure 3.4 demonstrate the acoustic impedance data distribution of non-irradiated and irradiated enamel and dentin.

Before irradiation of the samples, acoustic impedance of both enamel and dentin was measured. Enamel from sound teeth showed higher acoustic impedance value ($Z = 12.94 \pm 0.67$ MRayl, n=9) than that of dentin (7.94 ± 0.69 MRayl, n=9), and therefore appeared to have higher elastic modulus due to the structure and organic components. The course of the acoustic impedance values with respect to radiation dose received can be clearly seen from Figure 3.4. The teeth samples exhibited reduced values in enamel and dentin starting from radiation dose of 2 Gy to 60 Gy. The mean acoustic impedance value of enamel of the pre-radiation teeth group of 12.94 ± 0.67 MRayl was the highest

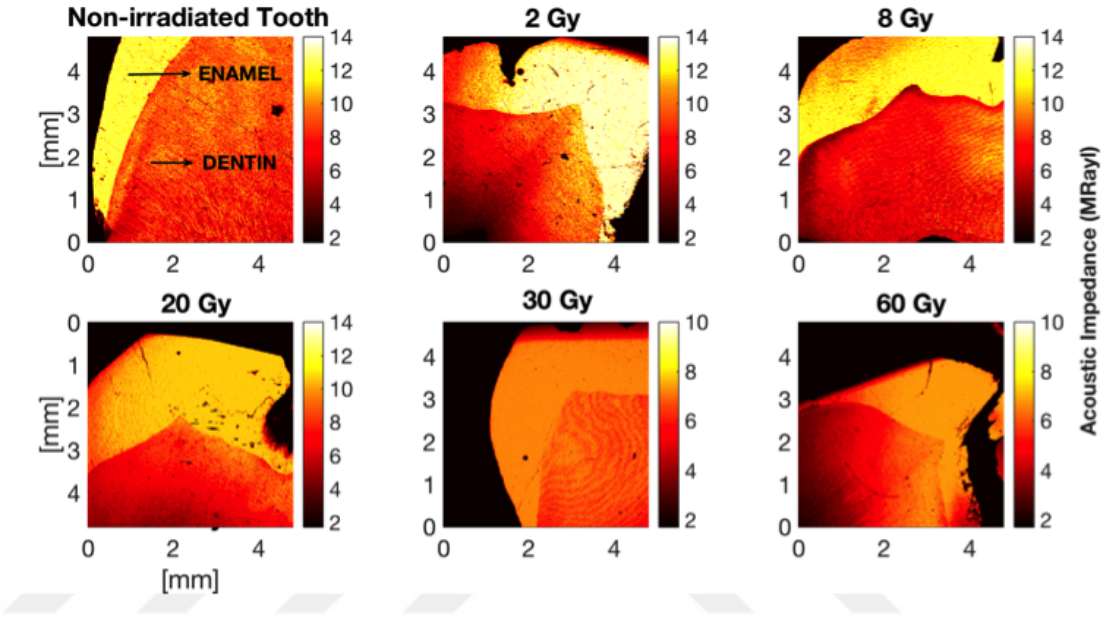


Figure 3.3. Two-dimensional acoustic impedance images of human tooth pre- and post-radiation therapy application recorded by 320 MHz Scanning Acoustic Microscopy. The resolution was defined through the field of view of 4.8 mm × 4.8 mm for each image with a 300 × 300 scanning points with a scan size of 16 μm. All image were determined to visualize both enamel and dentin within a signal scan. Gradation in color bar (red to yellow) represent the variation after subjection to radiation doses which are clinically used to cure head and neck cancers. Sound dentin shows up higher acoustic impedance (orange to yellow) than the softened dentin through radiotherapy.

Table 3.1. Mean and Standard Deviation of recorded acoustic impedance values for each region and irradiation dose obtained by 320 MHz Scanning Acoustic Microscopy (SAM). The statistically different groups were marked with the stars ($p < .05$.)

Group & **Region**		**Acoustic Impedance (MRayl)**
Control	Enamel	12.94 ± 0.67
	Dentin	7.94 ± 0.69
2 Gy	Enamel	12.65 ± 0.43
	Dentin	7.42 ± 0.35
8Gy	Enamel	11.88 ± 0.35
	Dentin	7.39 ± 0.27
20Gy	Enamel	11.37 ± 0.63
	Dentin	6.52 ± 0.43*
30Gy	Enamel	7.24 ± 0.18*
	Dentin	5.71 ± 0.66*
60Gy	Enamel	6.49 ± 028*
	Dentin	4.82 ± 0.53*

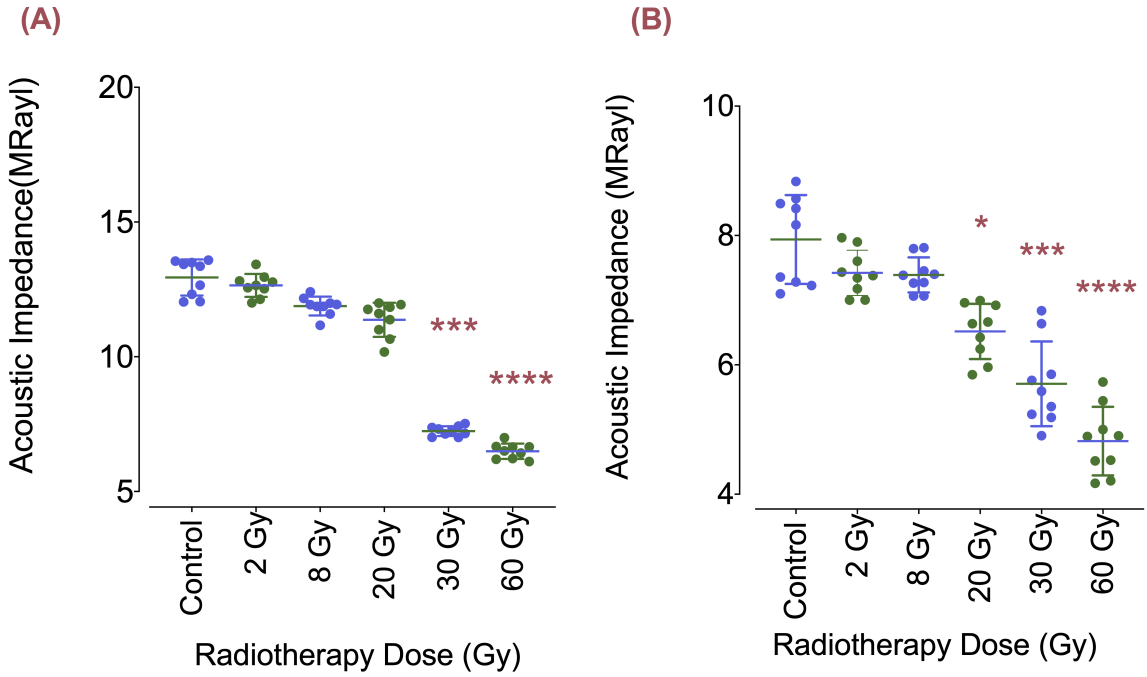


Figure 3.4. Distribution of acoustic impedance values for enamel (A) and dentin (B) for non-irradiated and irradiated groups (control, 2 Gy, 8 Gy, 20 Gy, 30 Gy and 60 Gy). Stars above the scatter plots show a statistically significant difference in mean acoustic impedance relative to non-irradiated group (*) ($p < 0.05$).

among the groups. The acoustic impedance values compared to non-radiated control group displayed significant variations after accumulated radiation doses of 30 Gy and 60 Gy, while irradiation doses lower than 30 Gy showed no significant effect on acoustic impedance distribution of the enamel (Figure 3.4). For enamel, after applying 30 Gy *in vitro* irradiation, the acoustic impedance was measured 7.24 ± 0.18 MRayl, which was lower than the acoustic impedance value of pre-irradiation group of 12.94 ± 0.67 MRayl. The difference from the control group was found statistically significant (p = .0002). After 60 Gy radiation dose application, the mean acoustic impedance value of 6.49 ± 028 MRayl was measured, which was statistically lower than that of the non-irradiated teeth group ($p < .0001$). Lower mean acoustic impedance values than that of the non-irradiated teeth group were also observed after 2 Gy, 8 Gy and 20 Gy *in vitro* irradiation which were figured out 12.65 ± 0.43 MRayl, 11.88 ± 0.35 MRayl, 11.37 ± 0.63 MRayl, respectively ($p > .05$).

For dentin, a trend of varying acoustic impedance values was also obtained as the teeth affected by radiation dose received. The average acoustic impedance value of 9 sound dentin, which were not irradiated, was higher than those of radiated dentin (7.94 ± 0.69 MRayl). Under radiotherapy doses of 2 Gy and 8 Gy, irradiation obviously had a minor effect on the biomechanical characteristic of the dentin. The recorded acoustic impedance values for 2 Gy and 8 Gy were 7.42 ± 0.35 MRayl and 7.39 ± 0.27 MRayl, respectively. These differences were not reported as significant. Compared to control group, the effect of *in vitro* subjection of the radiotherapy dose of 20 Gy towards the teeth was measured as the acoustic impedance of the dentin diminished from the mean acoustic impedance value of 7.94 ± 0.69 MRayl to 6.52 ± 0.43 MRayl. The variation in the acoustic impedance was stated as a significant difference at the $p = .0296$ level. The comparison between 30 Gy radiation dose group and the pre-irradiated group revealed a significant change from 7.94 ± 0.69 MRayl for the sound dentin group to 5.71 ± 0.66 MRayl for post-irradiation teeth group ($p = .0006$). For dentin, 60 Gy irradiation had the highest level of influence on the human teeth in terms of difference in mean acoustic impedance value. Non-irradiated group had the mean acoustic impedance of 7.94 ± 0.69 MRayl on the other hand, 60 Gy radiation dose received group had the

average acoustic impedance of 4.82 ± 0.53 MRayl exhibiting a significany change ($p < .0001$).

3.3.2. Scanning Electron Microscopy

The enamel of pre-irradiation teeth showed the presence of regular normal enamel at all depths with the well-organized prisms as it can be clearly seen in Figure 3.5. Similar characteristics were also observed after subjection of radiation doses of 2 Gy, 8 Gy and 20 Gy on enamel surface. On the other hand, following exposure to 30 Gy, a slight micro-morphological variation was visualized in the prismatic structure of the enamel with all of the inspected regions of the treated tooth (Figure 3.5). With an increasing dose of radiation to 60 Gy, micro-morphological variations appeared more evident. Exposure to 60 Gy hindered the observation of interprismatic structure and hydroxypatite crystals making the enamel surface amorphous.

As for dentin, the pre-irradiation group demonstrated well-defined intertubular, peritubular and dentinal tubule together with an normally ordered collagen network. The SEM photomicrographs of the groups subjected to radiation doses of 2 Gy and 8 Gy showed similar micromorpholocial properties. In comparison to sound dentin images, treatment of the teeth by 30 Gy and 60 Gy radiation doses caused a progressive variation in the morphology in all of the assessed parts. Due to the increasing radiation doses, intertubular dentin, peritubular dentin and dentinal tubular illustrated unregular structure compared to non-irradiated group. The dentinal tubules started disappearing for the 60 Gy irraditation 50000x magnification.

3.4. Discussion

Though the radiotherapy efficaciously cures individuals with head and neck cancers, it may bring several side effects lowering the quality of life. The deterioration of the elasticity of the human tooth after radiotherapy has not well developed. Accordingly, this study was motivated by the desire to suggest a hand-held tool which

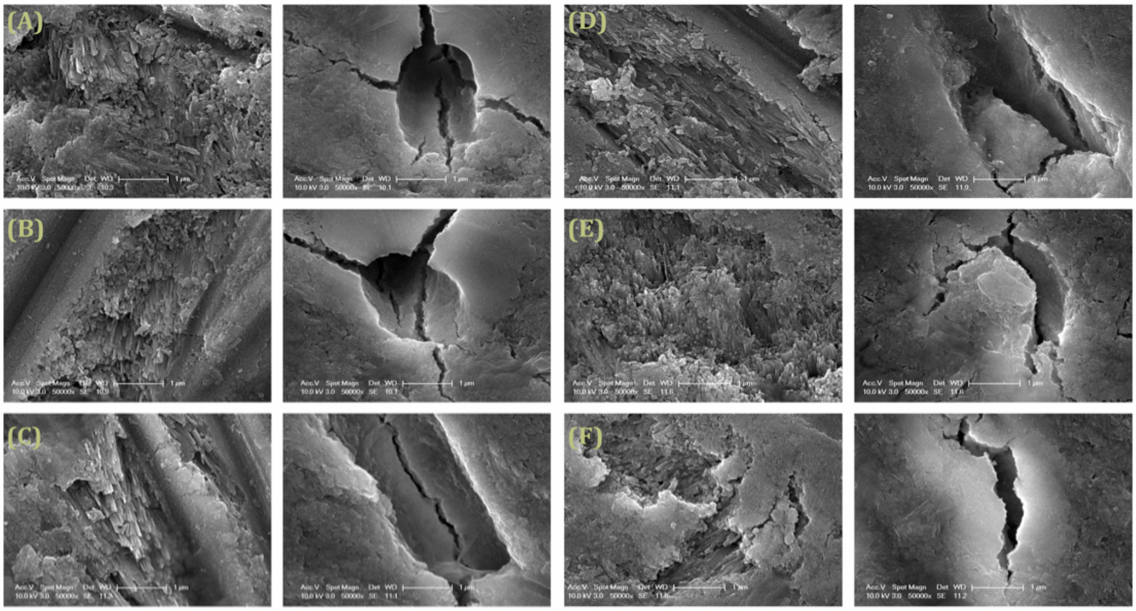


Figure 3.5. Electron micrographs of the enamel and dentin of the human molar teeth. The images were obtained by Scanning Electron Microscopy (SEM) at 50000x. Left-hand side images represent enamel, while right-hand side show dentin. (A) No irradiation (B) 2 Gy, (C) 8 Gy, (D) 20 Gy, (E) 30 Gy and (F) 60 Gy, respectively.

might enhance our understanding about the micromechanical properties of the human tooth. Our aim was to show the applicability of 320 MHz Scanning Acoustic Microscopy (SAM) in the evaluation of the tooth alteration at the micrometer level following radiation therapy. The radiation dose dependence of the acoustic impedance variations on the extracted human teeth was quantitatively identified using 320 MHz SAM in the acoustic impedance mode. The outcomes suggest that SAM is a promising tool to analyze the elasticity and its distribution in the targeted tissue *in situ*. Based upon the principle of acoustic impedance measurement, a hand-held acoustic probe, which establishes a relationship between acoustic impedance variations and the radiation doses, may be designed in future. Hence, acoustic impedance measurements *in situ* could pave the way to follow dental tissue at the microscale resolution to guide and ensure the safety of individuals treated by radiotherapy with a non-invasive and non-ionizing approach in clinical settings.

Findings in the proposed study showed that the average acoustic impedance values of non-irradiated sound dentin were lower than those of non-irradiated sound enamel. This difference was as anticipated, since enamel differs from dentin in the form of structure and orientation. A link between structural variations and elastic features of enamel and dentin was formely documented through determination of elastic modulus [150]. Results imply that SAM could be used to distinguish enamel from dentin through the acoustic impedance quantification.

The study further demonstrated that enamel behaved rather differently from dentin as a function of the irradiation dose. The findings of the method gave that ionizing radiation resulted in a dose-dependent reduction in the enamel microhardness for cumulative doses of 30 Gy and 60 Gy. For the doses, a conformable relationship between the variations in acoustic impedance and prismatic structure of enamel was established. SEM images showing the prismatic structure of enamel appeared more evident with the radiation doses of 30 Gy and 60 Gy, which matched the literature [151]. This observation was also in agreement with the previous study of teeth indicated that microhardness of irradiated human teeth was lower compared to non-irradiated human

teeth groups [141]. Radiotherapy can lead to restructuring of the crystal structures of mineralized tissues, and accordingly makes changes in the structural elasticity. The enamel is organized by prisms, and the structural orientation defines the non-isotropic appearance of the enamel and reflects it mechanical features [152]. SEM investigations for 30 Gy and 60 Gy irradiation doses unclosed morphological variations in the enamel marked through progressively disorganized interprismatic structure, as previously studied [152]. The elasticity and the integrity of the teeth were affected, and the radiogenic damage was observed as a lower microhardness in enamel proved by acoustic impedance. This may occur because of decarboxylation of the tissue [131]. The lower acoustic impedance value and the change in enamel crystalline structure might be the reason for the increased risk of dental deterioration after radiotherapy. The lack of statistical differences in the acoustic impedance after 2 Gy, 8 Gy and 20 Gy dose exposures has to be clarified, as the enamel mechanical structure and composition might be affected through ionizing radiation; yet those modifications may be incipient evidences of slight micro-morphological alterations in the enamel. This result should be regarded for the establishment of protocols to hinder or weaken deleterious influences during radiotherapy. The elastic properties of dentin undergone radiotherapy appeared to be much more than those of enamel. Following cumulative irradiation with 20 Gy, decreasing trend in acoustic impedance values of dentin was observed. As for SEM images, it was observed irradiated teeth by cumulative radiation doses of 20 Gy, 30 Gy and 60 Gy presented an increasing morphological deterioration. Starting with 20 Gy, presence of fissures, cracks and obliteration in dentinal structure became notable. The reduction in dentin elasticity evidenced by the acoustic impedance measurements may be expressed by the variations in organic components in dentin tubules.

The literature has also reported ionizing radiation may lead to reduction in microhardness [151]. Enamel and dentin responded differently to the radiotherapy, which is possibly due to the water content. Dentin has higher water content equal to 10% whereas enamel has 4% by weight [153]. Resulting from the physical interaction of ionizing radiation in water, radiotherapy causes production of free radicals and hydrogen peroxide [154]. Thereby, in terms of water content, dentin may be more unstable

and susceptible to the radiotherapy, and a substantial influence on the microhardness of dentin structure was observed. Acoustic impedance of dentin was progressively reduced with the increasing radiation doses. SEM images reflecting micro-morphological alterations such as obliteration and fissures in dentinal structure may also confirm the progressive differences in elasticity of dentin. The proposed study was employed *in vitro*, therefore it has constrains on the reproduction factors (i.e., alterations in oral microflora and hyposalivation) that cannot be taken into account.

Determination of acoustic impedance values made a reliable technique for quantification of microhardness characteristics of dental tissues with no mechanical harm to the samples. Our findings support the evidence of a direct radiogenic-related influence on enamel and dentin at the micrometer level. Scanning Acoustic Microscopy (SAM) was suggested as a feasible method which enables detection of alterations in the microhardness due to the radiation therapy through the acoustic impedance values of enamel and dentin. As a future study, we plan on applying a dose of 2 Gy/fraction up to a cumulative dose of 60 Gy. The measurements of post-irradiation enamel and dentin acoustic impedance are aimed to be measured after every 2 Gy of irradiation till completing 30 irradiation cycles. Based upon the principle of acoustic impedance measurement, a hand-held ultrasonic stiffness checker establishing a relationship between acoustic impedance variations and the radiation doses may be designed. The link between micro-mechanical to morphological variations needs further assessments.

4. QUANTIFYING THE INFLUENCES OF RADIOTHERAPY ON DEFORMABILITY OF HUMAN ERYTHROCYTES BY DUAL-BEAM OPTICAL TWEEZERS

4.1. Radiotherapy Treatment and Red Blood Cells

Radiation therapy is widely used as a treatment tool for malignancies since it is capable of killing cancer cells and shrinking tumors using ionizing radiation. However ionizing radiation, typically face issues not only because of the target tumor action but also because of the adverse influences of radiation exposure on non-target cells or tissues [155]. In recent years, there has been an increasing amount of research on the use of ionizing radiation due to the high targeting capacity and therapeutic effect. Though radiation therapy brings many advantages in the application, radiation-related complications are still unavoidable risks for off-target cells. Accordingly, decreasing its adverse consequences on the off-target cells is a critical problem, and remains a significant research area for radiation biology. Radiotherapy can promote biological damage at the molecular level and cellular DNA chains as single- or double-strand breaks. On the one hand, DNA in the nucleus was marked as the initial and fundamental target of radiation exposures directly by deposition of energy or indirectly by the production of reactive oxygen/nitrogen species. Thus, the primary adverse effects are attributed to DNA deterioration in target cells which have not been properly brought back through processes of metabolic repairment [156, 157]. On the other hand, radiotherapy also acts directly on the membrane, confirming that plasma membrane shows an alternate path to DNA in radiation-modulated cell reactions [90]. Previous studies have documented the direct influences of cellular death caused by human tissue irradiation in particular attention to chromosome rearrangement and genetic mutation resulting from the radiation-induced deposition of energy [158–161]. Also, cellular immunity, free hemoglobin level, sodium ions (Na^+), potassium ions (K^+) and chloride ions (Cl^-)

concentrations, cell outline variations, a reduction in the production and alterations in the aggregation state of platelets have been researched studies on the irradiation of red blood cells [162–171]. Mostly, these investigations reveal that there is an association between the irradiation dose and the loss of the erythrocyte function. However, little is known about the possible effects on mechanical features of the red blood cells exposed to radiation therapy. Measurement of mechanical properties such as elasticity, deformability, and stiffness in biological specimens are extensively regarded to reflect variations in biological function, and can demonstrate the mechanical principles of organism units in numerous physiological or pathological states [172,173]. Both morphology and cytoskeleton meshwork regulate red blood cell deformation and impairment. Abnormalities in the biconcave disc shape, the membrane, and the cytoskeleton closely pictures some red blood cell-related diseases [174]. They give rise to characteristic illnesses such as diabetes mellitus [175], sickle cell anemia [176], malaria [177] and cancer [178]. It is also well-known that radiotherapy leads to many complex and dynamic variations in cell outline along with cell membrane damage. To illustrate, changes in the membrane permeability and the membrane-cytoskeleton structure may induce differences in the membrane, containing metabolic and behavioral changes, giving rise to cell dysfunction [179–181]. Therefore, knowledge of the cell mechanics at the whole-cell level contributes to the further understanding of radiation-related damage.

Different methods assess elasticity and deformability of cells AFM, micro-needle manipulation, cell poking, and magnetic tweezers [182–187]. However, they encounter fundamental obstacles to generalized application. The tools have a high spring constant relative to the modulus of elasticity of the sample, and they are not capable of resolving small differences in cell elasticity. Some of these methods can only reach a limited fragment of the cell due to the contact area. Accordingly, whole-cell elasticity cannot be directly measured.

Laser traps enable holding, manipulation, and characterization of a diverse variety of microscopic and nanoscopic materials [28–31]. Optical forces, exerted through light due to the momentum transferred, have been applied to investigate elasticity of ery-

throcytes using two optical techniques: optical tweezers method and optical stretcher method [21, 188–191]. The dual-beam optical tweezers in stretching mode produces forces which bridge those produced through conventional optical tweezers. The whole-cell cortex elasticity can be directly quantified by the measurements of deformation in this method. Without microbead handles simple set-up also has the benefits of a large amount of whole-cell mechanical determinations. Non-physiological handling by surface-attached microbeads can also result in measurement artifacts. Besides, these methods necessitate quite complicated experimental preparations such as microbead attachment to the cell membrane, and a considerable amount of cells cannot be measured in a limited life cycle of live cell cultures. Up until now, the ability of dual-beam optical tweezers in stretching mode producing a measurable deformation of the erythrocytes exposed to radiotherapy has never been tested. For this reason, we probed whether definitive or subtle changes in the deformability of the erythrocytes in response to radiotherapy can serve as a sensitive biomarker by dual-beam optical tweezers measurements. To test this, blood samples were irradiated with 2 Gy (n=109), 12 Gy (n=112), and 25 Gy (n=118) radiation doses. Also effects of radiation therapy on red blood cells were investigated through hemogram analysis for each irradiation dose in the study.

4.2. Methods

A commercial dual-beam tweezers (Zeiss PALM Micro Tweezer) with 1064 nm laser wavelength, 3W output power, and 100X oil immersion (NA=1.518) objective was used to perform the stretching experiments, see Figure 4.1A (Created with Biorender.com). The set-up was operated in stretching mode to record the deformability of the red blood cells, as cartooned in Figure 4.1B.

First of all, the traps were positioned on the two sides of a single red blood cell with the trap separation of 5 μm. In this configuration, they were off. Then, they were activated, and one of the traps was moved with the velocity of 0.5 μm/s for 20 s time duration. During that time, with the movement of the trap, the RBC first started

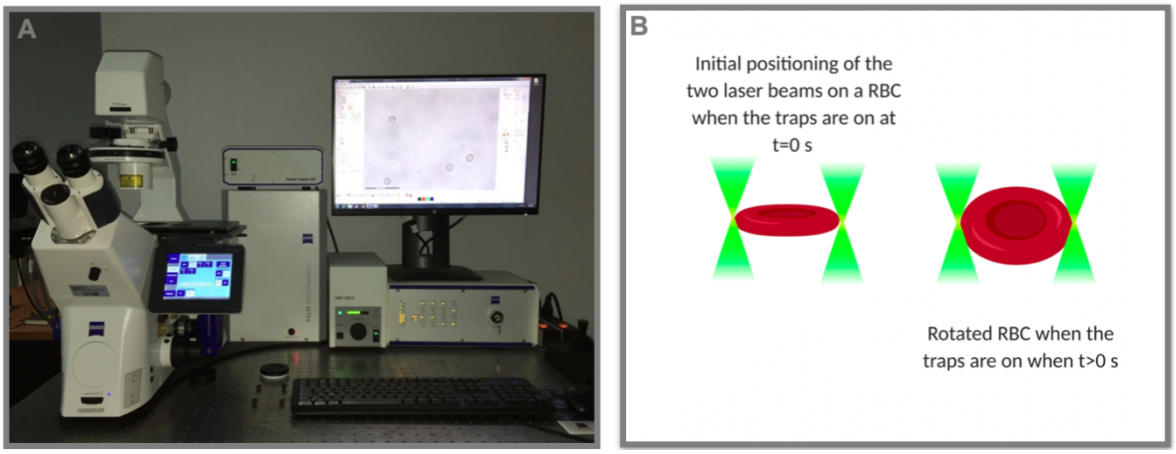


Figure 4.1. (A) Dual-beam Optical Tweezers Set-up used to quantify deformability of red blood cells (RBCs) after radiotherapy treatment, (B) Initial positioning of the traps on a RBC in stretching mode.

stretching and then after reaching to a certain length, it escaped from the moving trap and began to relax. In the shape analysis of each single red blood cell, we used an analysis script that was written in MATLAB. This script first converted the frame from an RGB image into a grayscale image. Then, this grayscale image was converted into a binary image. This binary image was sent to MATLAB's Maximum Feret Diameter (MFD) function, which gave the extreme edges of the cell boundary and was used to track the change of axial length of the RBC. This script offered the initial (minimum) and final (maximum) lengths of the RBCs over 20 s. From this, we extracted the deformability index (DI) by the following equation [191]:

$$DI = \frac{L_{max} - L_0}{L_0} \tag{4.1}$$

where, L_0 is the unstretched (initial) size, L_{max} is the maximum (final) stretched size of the RBC.

4.2.1. Sample Preparation

Blood samples were collected by puncturing a fingertip using a sterile lancet needle. Blood smear on the tip of micropipette was mixed with a solution consists of 1 mL PBS and 100 μL BSA (Bovine serum albumin). For preventing RBCs to adhere to the cavity well microscope slide, 15 μL BSA was dried on a coverglass inside an incubator at 24.5° C for 2 hours [192]. Prepared sample of 70 μL was placed onto the microscope slide and BSA-dried cover glass was placed on top of it (Figure 4.2). The borders of the cover glass was sealed using a nail polish. All the experiments were performed at room temperature.

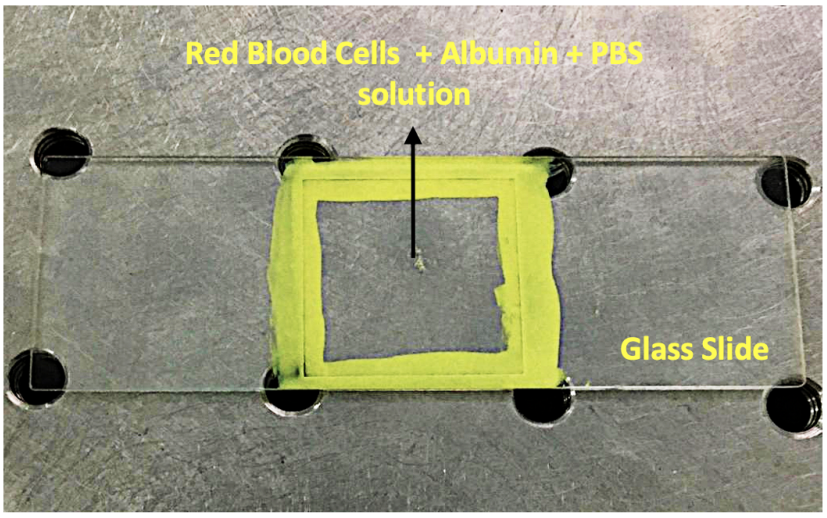


Figure 4.2. Blood sample + Bovine serum albumin (BSA) + Phosphate-buffered saline (PBS) solution on a glass slide with a well at the center.

4.2.2. Irradiation Protocol

The blood samples stored in EDTA tubes were irradiated by a total and single-dose application of 2 Gy, 12 Gy and 25 Gy in a single fraction by LINAC (Elekta Versa HD, Elekta, Crawley, UK) in Istanbul Oncology Hospital. This study used 6 MV flat with a dose rate of 600 cGy/min used in dmax and unflattened photon beams with a

dose rate of 1200 cGy/min. The EDTA tubes were submerged in a custom-made rice phantom in an attempt to distribute radiation homogeneously and mimic the body. The remaining details of the irradiation protocol was the same as the sub-chapter 3.2.2.

4.3. Results

The results of the current study evidenced significant differences in initial (unstretched) cell size, final (stretched) cell size and DI of RBCs, among the control and the experiment groups. Statistical differences were calculated by using Student's t-test, one-way ANOVA and Dunnett's multiple comparisons tests for the groups (i.e. the control and an experiment group). Results were accepted statistically different when $p < 0.05$ for each analysis. The behavior of red blood cell diameter in stretching experiment is shown in Figure 4.3.

The stretching experiment was performed with different laser trap powers (operating at 40%, 60%, 80% and 100%) on the control group (0 Gy) to characterize the dependence of DI on the trapping laser power. According to the Figure 4.4A, a linear increase was observed in DI with an increasing trap power [193]. Since the maximum stretching of the RBCs (without rupturing) was preferred, the experiments were conducted with the laser traps operating at 100% power for all the data groups. The relation between the unstretched size of RBCs and DI was analyzed by using a linear regression as given in Figure 4.4B. When all the dose groups along with the control group were considered, an inverse relation between the unstretched cell size (L_0) and DI was observed for each data set. RBCs in the experiment groups were viewed to be more deformable compared to control group.

Table 4.1 shows the comparisons among control and experiment groups (2 Gy, 12 Gy and 25 Gy). L_0, L_{max} and DI parameters for all the groups were compared and statistically different groups were determined through one-way ANOVA and Dunnett's multiple comparisons test. A $p < 0.05$ value was considered statistically different.

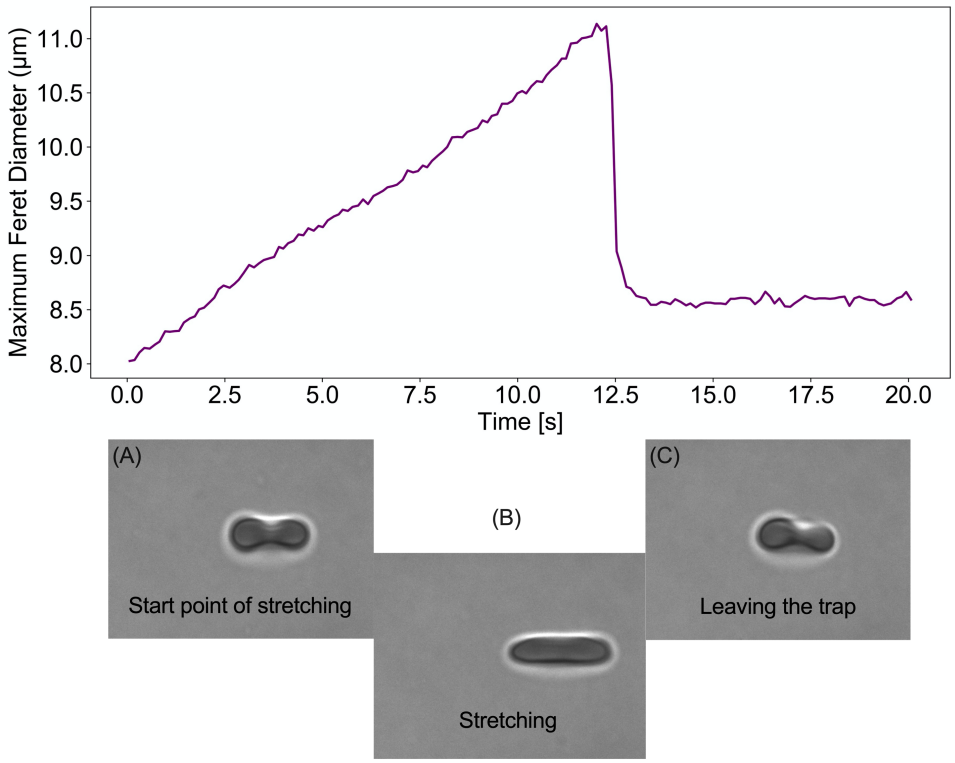


Figure 4.3. Stretching of a RBC by dual-optical traps, (A) The traps were positioned on the two ends of the RBC with the trap separation of 5μm, corresponding the starting point of the stretching, (B) Just before escaping from one of the traps, RBC was reached to the maximum length, showing the peak of the Maximum Feret Diameter (MFD) vs time graph, (C) Contracted RBC after escaping from the traps.

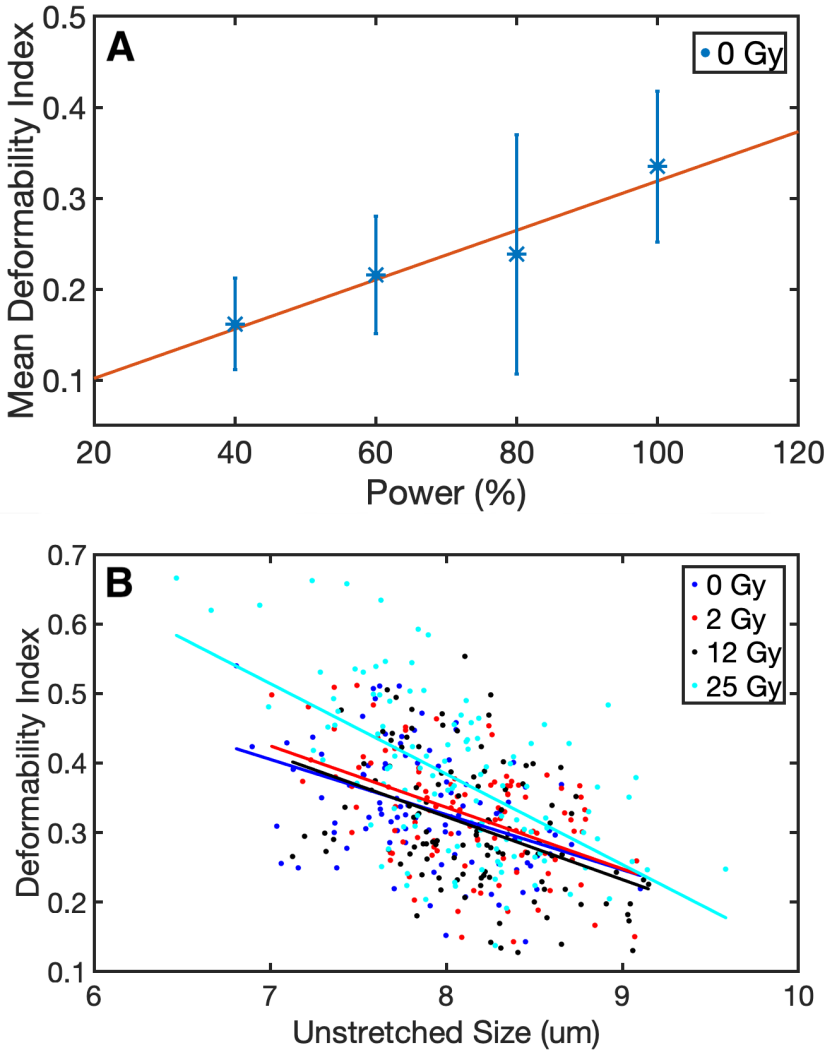


Figure 4.4. (A) Change in the mean DI of the control group with respect to the laser trap power operating at 40%, 60%, 80% and 100%, (B) The scatter plot of DI vs. unstretched RBC size with the corresponding linear fit lines are presented for the four data groups. R-squared values of the linear fit lines: 0.170, 0.235, 0.167, 0.344 for the data sets of 0 Gy, 2Gy, 12 Gy, 25 Gy, respectively.

Besides, Kernel density estimation plots, given in Figure 4.5, revealed that the initial cell sizes (L_0) for each experiment group were found to be significantly ($p < 0.05$) elevated relative to the control group, see also Table 4.1.

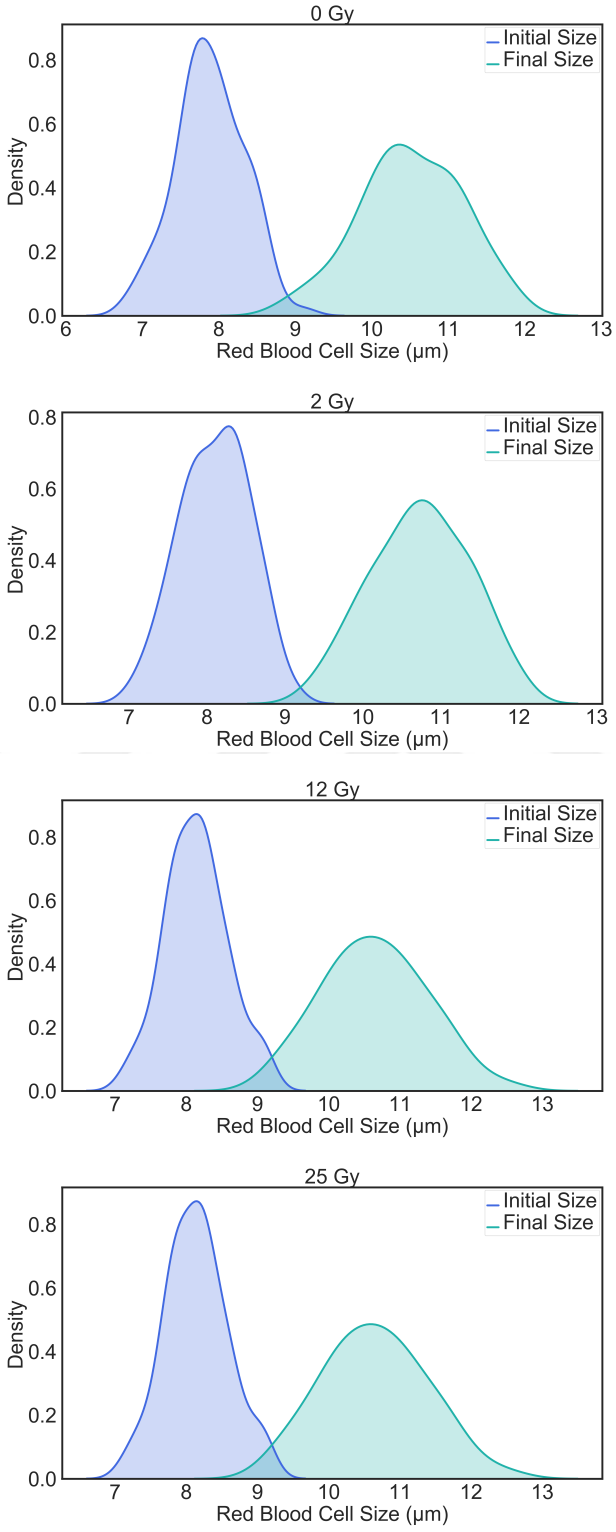


Figure 4.5. Kernel density estimations for pairs of initial and final RBC lengths in the control group, 2 Gy, 12 Gy and 25 Gy groups.

Table 4.1. Comparisons of the control group and experimental groups in accordance with the one-way ANOVA and Dunnett's test. A $p < 0.05$ value was considered statistically different. ns shows no significant difference among groups.

		***p*-value**	
Dose Groups (Gy)	$L_0(\mu\text{m})$	$L_{max}(\mu\text{m})$	DI
0-2	0.0042	0.0953(ns)	0.9312(ns)
0-12	0.0004	0.4883(ns)	0.2194 (ns)
0-25	0.0424	9e-08	0.0068
2-12	0.9233(ns)	0.7815(ns)	0.5264(ns)
2-25	0.8361(ns)	0.0040	0.0005
12-25	0.4481(ns)	0.00005	2e-06

The calculated deformability indices for each data set are demonstrated in Figure 4.6A and the corresponding Kernel distributions given in Figure 4.6B shows that, compared to the 0 Gy, mean DI was significantly increased in 25 Gy group, while a decrease was observed for 12 Gy group.

On the other hand, between the control group and 2 Gy group, no significant difference was recognized in DI (p=0.9312, Table 4.2). Among the all data sets, the highest variance in DI was observed in 25 Gy group with the corresponding Kernel bandwidth of 0.0518.

Table 4.2. Number of the RBCs, mean of L_0, L_{max} and DI values for each data set.

Dose (Gy)	**# of RBCs**	**Mean L_0 (μm)**	**Mean L_{max} (μm)**	**Mean DI**
0	97	7.87 ± 0.44	10.51 ± 0.66	0.33 ± 0.08
2	109	8.11 ± 0.44	10.74 ± 0.44	0.33 ± 0.08
12	112	8.14 ± 0.43	10.65 ± 0.43	0.31 ± 0.09
25	118	8.05 ± 0.52	11.06 ± 0.76	0.38 ± 0.11

Table 4.3 tabulates the hematological parameters in the non-irradiation (control)

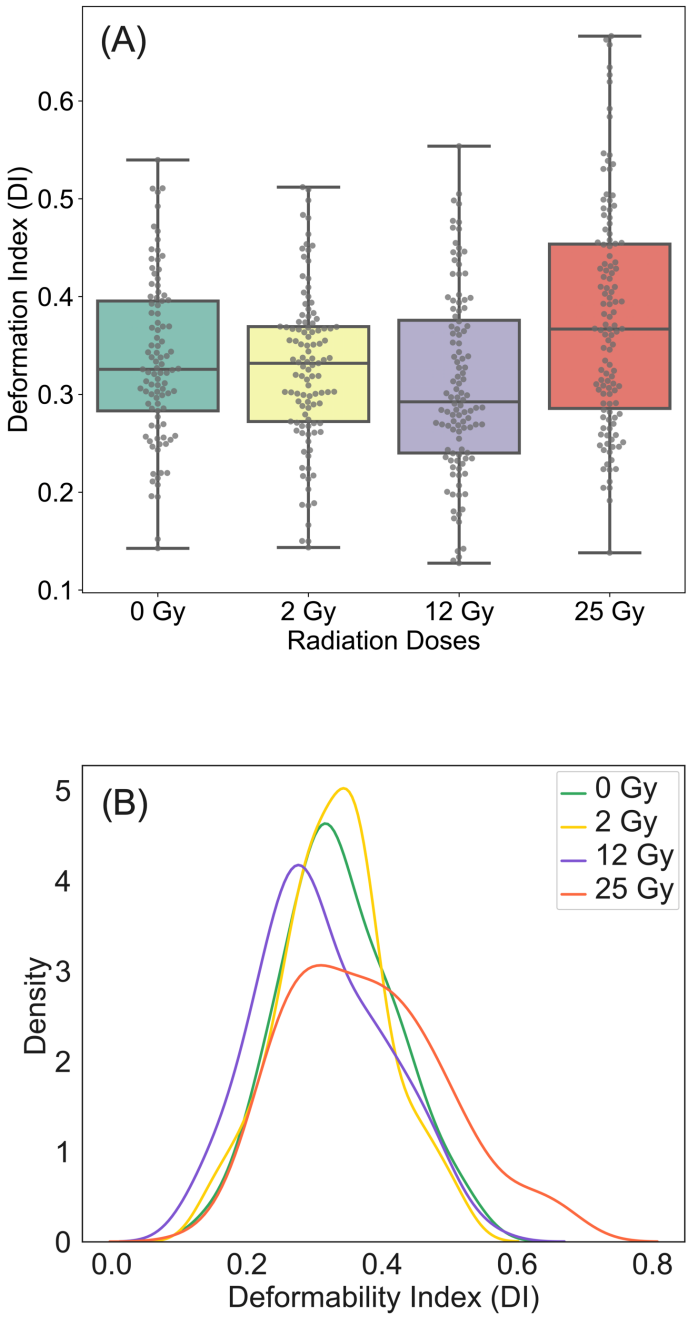


Figure 4.6. (A) The box plot shows the summary of the four data sets. The gray dots show the data points, and the gray line in the boxes show the mean values of the corresponding data sets, respectively. (B) Kernel density estimations (kernel=normal) for deformability index are demonstrated for each dose groups. Kernel bandwidths were found as: 0.0362, 0.0278, 0.0379, 0.0518 for the groups 0 Gy, 2 Gy, 12 Gy, 25 Gy, respectively.

and treated groups by 2 Gy, 12 Gy and 25 Gy, respectively. 12 Gy and 25 Gy radiotherapy doses got higher values with an increasing trend compared to control and 2 Gy groups in the number of white blood cells (WBC) and platelet (PLT). However, with the increasing doses (12 Gy and 25 Gy), the decrease in the number of red blood cells and the decrease in the amount of MCHC (mean cell hemoglobin concentration) was observed compared to the control group. The values for WBC, PLT and red blood cells were all in the reference range but they showed a different values compared to the non-irradiated group in that range.

Table 4.3. Whole blood count comparisons between the non-irradiated group and irradiated groups at 2 Gy, 12 Gy and 25 Gy. WBC: White Blood Cell, RBC: Red Blood Cell, HCT: Hematocrit, MCH: Mean Corpuscular Hemoglobin, RDW: Red Cell Distribution Width, MCHC: Mean Cell Hemoglobin Concentration, MCV: Mean Cell Volume, PLT: Platelet, RDW-CV: Red Blood Cell Distribution Width.

Parameters (unit)	**Reference**	**Control**	**2 Gy**	**12 Gy**	**25 Gy**
WBC($\times 10^3/\mu L$)	4.0 - 10.0	**4.98**	**4.93**	**6.64**	**6.78**
Neutrophil($\times 10^3/\mu L$)	2.00 - 7.00	**1.89**	**1.98**	3.68	3.71
Lymphocyte($\times 10^3/\mu L$)	0.80 - 4.00	2.61	2.50	2.36	2.42
Monocyte($\times 10^3/\mu L$)	0.12 - 1.20	0.32	0.31	0.48	0.49
Eosinophil($\times 10^3/\mu L$)	0.02 - 0.50	0.14	0.13	0.10	0.12
Basophil($\times 10^3/\mu L$)	0.00 - 0.10	0.02	0.01	0.02	0.04
RBC($\times 10^6/\mu L$)	3.50 - 5.50	**4.50**	**5.06**	**4.53**	**4.50**
HGB(g/dL)	11.0 - 16.0	**13.7**	**14.8**	**13.9**	**13.7**
HCT(%)	37.0 - 54.0	43.8	45.7	44.0	43.8
MCV(fL)	80.0 - 100.0	97.2	90.3	97.1	97.2
MCH(pg)	27.0 - 34.0	29.6	29.2	30.6	30.5
MCHC(g/dL)	32.0 - 36.0	32.9	32.3	**31.5**	**31.4**
RDW-CV (%)	11.0 - 16.0	12.7	11.8	12.8	12.7
PLT($\times 10^3/\mu L$)	100 - 300	**259**	**252**	**276**	**282**

Figure 4.7 indicates effects of radiation therapy on red blood cell morphology for the control and three experimental groups (2 Gy, 12 Gy and 25 Gy). The images revealed prominent morphological variations for 12 Gy and 25 Gy. The number of crenated red blood cell was increased per image area with the increasing dose.

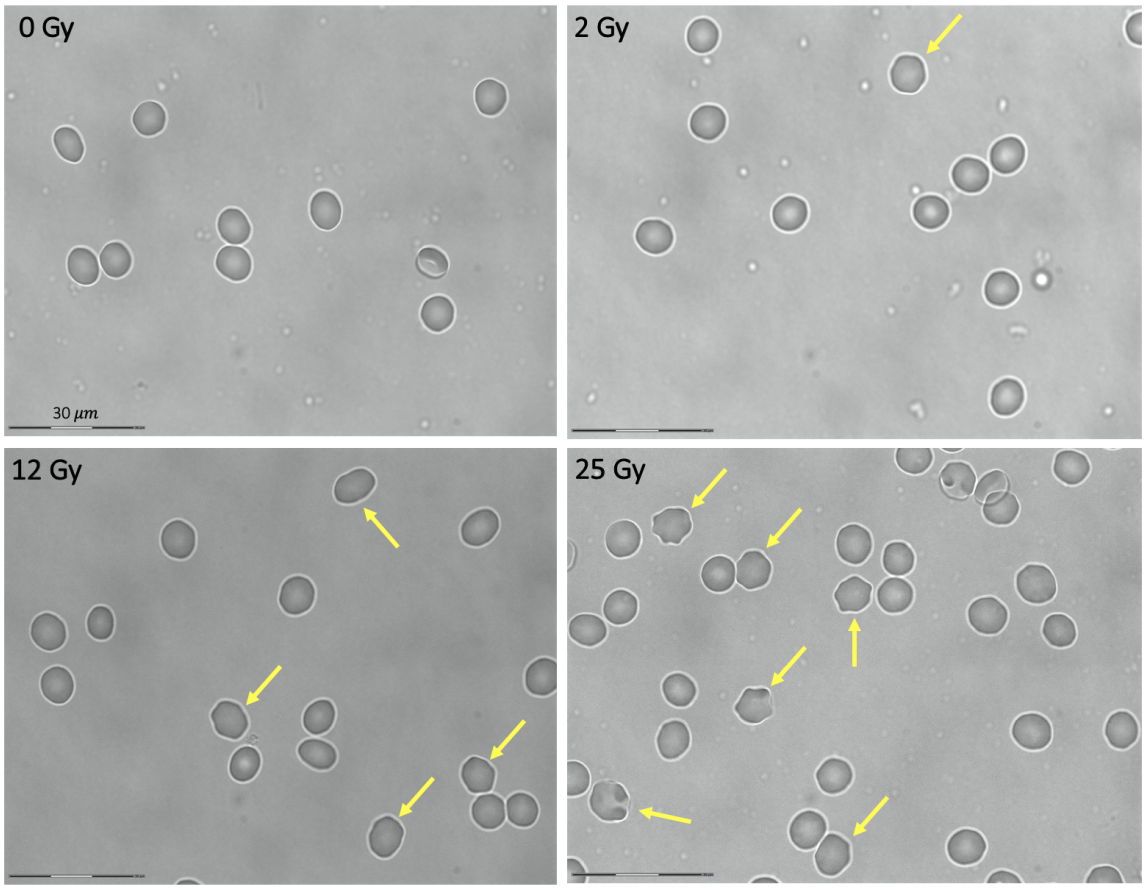


Figure 4.7. Morphology of red blood cell sample for non-irradiated and irradiated experimental groups at 2 Gy, 12 Gy and 25 Gy, respectively. Yellow arrows indicate morphologically differentiated red blood cells after radiotherapy exposure.

4.4. Discussion

We showed a feasibility study of radiation therapy effects on the mechanical properties of cells using dual-beam optical tweezers in stretching mode by the measurements of optical deformability. The method was first tested on a red blood cell model as proof of concept. Up until now, no study has measured the deformability of erythrocytes as a determinant factor to assess cell reactions to radiotherapy. Healthy red blood cells were irradiated by 2 Gy, 12 Gy and 25 Gy cumulative radiation doses. Deformation, which is a function of time and equated to the elasticity of cells, permitted the sensitive distinction between non-irradiated and irradiated red blood cells. The findings reported that irradiation of red blood cells by 2 Gy, 12 Gy and 25 Gy quantified by the dual-beam optical tweezers showed a dose-dependent variations (increase or decrease) in the stiffness of the erythrocyte membrane. The relationship may be mainly emerged due to the following explanations.

Radiobiology has been studying the biological responses of cells or tissues to ionizing radiation. It is well-known that ionizing radiation provokes damage directly by deposition of energy or indirectly by production of reactive oxygen/nitrogen species in DNA double helix in the nucleus. However, the origin of molecular events triggered at the plasma membrane, which are caused by radiation, is unclear. Erythrocytes were used as primary test objects since they are nucleus-free, and have smooth membrane surfaces maintaining their integrity. Also, they are off-target cells circulating all over the body, and thus a good model to study the biomechanical effects on the structure following radiation exposure. Taken together, we focused on any potential radiation-related effects on the deformability of the red blood cortex to distinguish adverse effects from DNA damage using the dual-beam optical tweezers in stretching mode. Healthy red blood cells have good biomechanical characteristics that build upon the biconcave disc shape, the cytoplasm viscosity, cytoskeleton and the stiffness of the phospholipid bilayer membrane. Current literature represents variation of any of these contributors may induce differences in the membrane morphology, cytoskeletal network, and mechanical features of RBCs and thus create morphologically distinct signals [194,195]. As

previously mentioned, these are responsible for both the deformability of red blood cells and variations in biolgical function. More specifially, notable variations in red blood cells arise from a coupled dynamic response of the membrane and spectrin meshwork. Spectrin, a fundamental component of cytoskeleton proteins, not only has a crucial role in the preserving the outline of the cell and cytoskeleton network but also reflects deformability or responses to exterior perturbations [196]. Our investigation presented that different radiation exposures lead to various degrees of damage to the membrane of red blood cells. Radiation exposure of red blood cells by 25 Gy generated the highest deformability among the irradiated groups. Based on statistical analysis, the red blood cell population for 25 Gy was significantly distinguishable with 95% confidence from the non-irradiated population. One of the reasons underlying this finding can be explained by the rearrangement of lipids, fatty acids, and spectrin-α1 protein and collapse of the membrane skeleton due to the radiation effects on the plasma membrane [197]. A link between cell stiffness and radiotherapy treatment was formerly documented, therefore this difference was as anticipated [198, 199]. A slight change in the outline of the red blood cells was observed for 25 Gy radiation exposure, which is shown in Figure 4.7. Red blood cell with damaged morphology was most frequently found in this radiation dose group. Namely, the number of crenated red blood cells was the highest per image area with 25 Gy exposure. Moreover, the hemogram results showed the highest values for the number of WBCs and platelets for 25 Gy. The reason behind the increase in the platelet number can be explained and verified by changes the aggregation state of platelets after radiotherapy exposure [171]. As for WBCs in hemogram, the dose was an influencing factor in the count that lead to a greater increase after radiotherapy exposure by 25 Gy. However, in the study of Sanzari *et al.* [200], radiotherapy decreased the number of white blood cells. Also, Taqi *et al.* reported no significant variations in the whole-blood count, and hence white blood cell counts [200]. Any differences between the current investigation and the literature reports can be attributed to the differences in the in the deposited amount of the irradiation doses in the cells. Furthermore, the mean hemoglobin concentration level was decreased in 25 Gy dose exposure. This can be because the plasma membrane of red blood cells consists of unsaturated lipid, and hemoglobin, being a free radical reaction source, may cause peroxidation of

lipid, which can influence fluidity and state of hemoglobin. The average deformability index for 12 Gy radiation dose was not significantly different to the average deformability index of 0 Gy but it showed a decreased deformation trend. Red blood cells in 12 Gy became less deformable compared to the non-irradiated group. However, this result did not match the literature reported earlier [198]. The increase in stiffness of red blood cells evidenced by the mean deformability index might be related to the slight increase in spectrin expression which was observed for values lower than 4 Gy in the study of Zhang *et al.*. Also, the maturity of erythrocytes for 12 Gy dose group may be the contributing factor to the mean deformability index. It is because erythrocytes become stiffer as they age, and consequently less deformable [201]. As for 12 Gy, slight variations in the morphology of the red blood cells were visualized. However, the number of morphologically deformed red blood cells was less than 25 Gy, as expected. Furthermore, as in the case of the irradiated group of 25 Gy, higher values were observed in the counts of WBCs and platelet whereas lower values were recorded for RBCs and hemoglobin concentration compared to control and 2 Gy groups. Contrary to published studies [198, 199], this study did not find a significant difference between 0 Gy and 2 Gy in terms of elasticity of red blood cells. Overall, the deformability indices obtained by dual-beam optical tweezers application proved there was no linear dependence between irradiation dose and stiffness of the red blood cells. Red blood cells responded to radiotherapy treatment differently because of the amount of the absorbed dose and cell features.

The dual-beam optical tweezers approach creates forces that bridges those obtained through conventional optical tweezers. A significant benefit of the technique over the conventional optical tweezers is that there is no requirement to attach and position microbeads to the cortex of the erythrocytes for stretching measurements. With this, we were able to measure the whole-cell elasticity of a large number of red blood cells in a life-span of cultured live-cells by eliminating the time taken to attach and locate the microbeads. Dual-beam optical tweezers also allowed us to probe definitive and subtle variations in the deformability of the red blood cells after radiotherapy treatment. Therefore, the findings of the present study provided the following insights for future

research: Dual-beam optical tweezers may be used as a biomarker to follow changes in response to radiotherapy treatment in a cell's mechanics, that is showed up in plasma membrane and cytoskeleton network in radiobiology investigations. Thus, this method may offer further knowledge in cellular function after radiotherapy with a more unifying view, containing mechanical properties from the membrane. Deformability measurements by the dual-beam tweezers may put a new emphasis on radiotherapy-induced effects in the future.

5. CONCLUSION

In this dissertation, biomechanical characteristics of living cells and tissue-mimicking materials were quantified by SAM and dual-beam optical tweezers set-ups by the measurements of acoustic impedance and deformability index to characterize the influences of external stimuli and biomarkers in cancer. This thesis covers three achievements. The conclusion from each achievement is given in the following.

We proposed the study in which we used NaCl diffusion in the agarose phantom and proved the feasibility of SAM equipped with 80 MHz which has a lateral resolution of 20 μm to track variations in the agarose phantom's acoustic impedance maps in time in Chapter 2. With this study, it was concluded that acoustic impedance measurements of sodium content by SAM in a micrometer resolution have a variety of benefits over other sodium determination techniques (flame photometry, flow cytometry, atomic absorption spectrophotometry, ISE, neutron activation and sodium MRI) owing to non-contact and non-destructive mechanism without special sampling and rapid observation capability corresponding to 2 minutes for 4.8 mm x 4.8 mm imaging area. Furthermore, we validated the sodium diffusion by means of time-varying acoustic impedance quantifications. Through these, we proposed a novel sodium content determination which may be employed not only in static image obtaining but also used for sodium ion dynamic investigations (e.g. the interaction of chemotherapeutic agents with the biological matter).

Chapter 3 gave the third major subject of this thesis that showed the potential of SAM in the quantification of radiation therapy effects on extracted and sound human third molar teeth by the acoustic impedance measurements. In accordance with the results, structure of the human teeth was apparently visualized in the form of acoustic impedance distributions. Thus, it was shown that 320 MHz SAM can measure direct radiogenic-related effects on enamel and dentin at the micrometer resolution by the acoustic impedance measurements. This study established a relationship between pre-

scribed radiation doses and acoustic impedance variations in human teeth. Besides, we were able to resolve enamel and dentin by the differences in acoustic impedance values. Hence, SAM was recommended as a feasible technique to evaluate micromechanical variations by the acoustic impedance measurements in enamel and dentin due to the radiotherapy treatment for head and neck cancer patients in pre-clinical settings. In the future, the potential of SAM can be implemented to a hand-held ultrasonic stiffness checker, which may be constructed based on the acoustic impedance measurement configuration.

The final achievement of this thesis was given in Chapter 4. Dual-beam optical tweezers for estimating the deformability or stiffness variations after radiotherapy treatment on the cell cortex of erythrocytes was studied since the origin of molecular events triggered at the plasma membrane, which are caused by ionizing radiation, remains unclear. The output obtained from this study indicated the *in vitro* exposure of human blood to radiation doses of 2 Gy, 12 Gy, and 25 Gy represented the different amount of effects, which was quantified by the measurements of deformability indices and account for definitive and subtle variations of erythrocytes. Detrimental impacts on the morphology of the red blood cells were found to be much more apparent with the increased dose. The number of deformed cells per image area was increased in the morphological analysis. Accordingly, the results of this study provided that deformability indices obtained by dual-beam optical tweezers in stretching mode may be used as a biomarker to follow variations, which cannot be detected by the whole-blood count and morphological investigations, in response to radiotherapy treatment in a cell's mechanics, that is showed up in plasma membrane and cytoskeleton network in radiobiology investigations. With this research we concluded that deformability measurements by the dual-beam optical tweezers may put a new emphasis on radiotherapy-induced effects in future.

REFERENCES

1. Washington, C. M. and D. T. Leaver, *Principles and Practice of Radiation Therapy-E-Book*, Elsevier Health Sciences, 2015.

2. Gunawan, A., *A study on Acoustic Impedance Microscopy for Biological and Medical Applications*, Ph.D. Thesis, Toyohashi University of Technology, 2015.

3. Holeček, M., P. Kochová and Z. Tonar, "Mechanical properties of living cells and tissues related to thermodynamics, experiments and quantitative morphology–A review", *Theoretical Biomechanics*, p. 1, 2011.

4. Wu, P.-H., D. R.-B. Aroush, A. Asnacios, W.-C. Chen, M. E. Dokukin, B. L. Doss, P. Durand, A. Ekpenyong, J. Guck, N. V. Guz *et al.*, "Comparative study of cell mechanics methods", *Nature methods*, Vol. 15, No. 7, p. 491, 2018.

5. Basoli, F., S. M. Giannitelli, M. Gori, P. Mozetic, A. Bonfanti, M. Trombetta and A. Rainer, "Biomechanical characterization at the cell scale: present and prospects", *Frontiers in physiology*, Vol. 9, p. 1449, 2018.

6. Lautenschläger, F., S. Paschke, S. Schinkinger, A. Bruel, M. Beil and J. Guck, "The regulatory role of cell mechanics for migration of differentiating myeloid cells", *Proceedings of the National Academy of Sciences*, Vol. 106, No. 37, pp. 15696–15701, 2009.

7. Alcaraz, J., J. Otero, I. Jorba and D. Navajas, "Bidirectional mechanobiology between cells and their local extracellular matrix probed by atomic force microscopy", *Seminars in cell & developmental biology*, Vol. 73, pp. 71–81, Elsevier, 2018.

8. Butcher, D. T., T. Alliston and V. M. Weaver, "A tense situation: forcing tumour progression", *Nature Reviews Cancer*, Vol. 9, No. 2, pp. 108–122, 2009.

9. Lee, G. Y. and C. T. Lim, "Biomechanics approaches to studying human diseases", *Trends in biotechnology*, Vol. 25, No. 3, pp. 111–118, 2007.

10. Lim, C., E. Zhou, A. Li, S. Vedula and H. Fu, "Experimental techniques for single cell and single molecule biomechanics", *Materials Science and Engineering: C*, Vol. 26, No. 8, pp. 1278–1288, 2006.

11. Wirtz, D., K. Konstantopoulos and P. C. Searson, "The physics of cancer: the role of physical interactions and mechanical forces in metastasis", *Nature Reviews Cancer*, Vol. 11, No. 7, pp. 512–522, 2011.

12. Bufi, N., M. Saitakis, S. Dogniaux, O. Buschinger, A. Bohineust, A. Richert, M. Maurin, C. Hivroz and A. Asnacios, "Human primary immune cells exhibit distinct mechanical properties that are modified by inflammation", *Biophysical journal*, Vol. 108, No. 9, pp. 2181–2190, 2015.

13. Lammerding, J., P. C. Schulze, T. Takahashi, S. Kozlov, T. Sullivan, R. D. Kamm, C. L. Stewart and R. T. Lee, "Lamin A/C deficiency causes defective nuclear mechanics and mechanotransduction", *The Journal of clinical investigation*, Vol. 113, No. 3, pp. 370–378, 2004.

14. Wang, J. H.-C. and B. P. Thampatty, "An introductory review of cell mechanobiology", *Biomechanics and modeling in mechanobiology*, Vol. 5, No. 1, pp. 1–16, 2006.

15. Guilak, F. and V. C. Mow, "The mechanical environment of the chondrocyte: a biphasic finite element model of cell–matrix interactions in articular cartilage", *Journal of biomechanics*, Vol. 33, No. 12, pp. 1663–1673, 2000.

16. Buxboim, A., I. L. Ivanovska and D. E. Discher, "Matrix elasticity, cytoskeletal forces and physics of the nucleus: how deeply do cells 'feel'outside and in?", *Journal of cell science*, Vol. 123, No. 3, pp. 297–308, 2010.

17. Pegoraro, A. F., P. Janmey and D. A. Weitz, "Mechanical properties of the cytoskeleton and cells", *Cold Spring Harbor perspectives in biology*, Vol. 9, No. 11, p. a022038, 2017.

18. Quan, F.-S. and K. S. Kim, "Medical applications of the intrinsic mechanical properties of single cells", *Acta biochimica et biophysica Sinica*, Vol. 48, No. 10, pp. 865–871, 2016.

19. Suresh, S., "Biomechanics and biophysics of cancer cells", *Acta biomaterialia*, Vol. 3, No. 4, pp. 413–438, 2007.

20. Pollard, T. D. and J. A. Cooper, "Actin, a central player in cell shape and movement", *Science*, Vol. 326, No. 5957, pp. 1208–1212, 2009.

21. Guck, J., R. Ananthakrishnan, H. Mahmood, T. J. Moon, C. C. Cunningham and J. Käs, "The optical stretcher: a novel laser tool to micromanipulate cells", *Biophysical journal*, Vol. 81, No. 2, pp. 767–784, 2001.

22. Soon, T. T. K., T. W. Chean, H. Yamada, K. Takahashi, N. Hozumi, K. Kobayashi and S. Yoshida, "Effects of anticancer drugs on glia–glioma brain tumor model characterized by acoustic impedance microscopy", *Japanese Journal of Applied Physics*, Vol. 56, No. 7S1, p. 07JF15, 2017.

23. Rahayu, R. H., K. Takanashi, T. T. K. Soon, I. Seviaryna, R. Maev, K. Kobayashi, N. Hozumi and S. Yoshida, "Reaction assessment of cultured breast cancer cells exposed to anticancer agents using microscale acoustic impedance profile", *Japanese Journal of Applied Physics*, Vol. 57, No. 7S1, p. 07LF26, 2018.

24. Topal, T., X. Hong, X. Xue, Z. Fan, N. Kanetkar, J. T. Nguyen, J. Fu, C. X. Deng and P. H. Krebsbach, "Acoustic tweezing cytometry induces rapid initiation of human embryonic stem cell differentiation", *Scientific reports*, Vol. 8, No. 1, pp. 1–11, 2018.

25. Lam, W. A., O. Chaudhuri, A. Crow, K. D. Webster, A. Kita, J. Huang, D. A. Fletcher *et al.*, "Mechanics and contraction dynamics of single platelets and implications for clot stiffening", *Nature materials*, Vol. 10, No. 1, pp. 61–66, 2011.

26. Dufrêne, Y. F. and A. E. Pelling, "Force nanoscopy of cell mechanics and cell adhesion", *Nanoscale*, Vol. 5, No. 10, pp. 4094–4104, 2013.

27. Wang, Y., E. L. Botvinick, Y. Zhao, M. W. Berns, S. Usami, R. Y. Tsien and S. Chien, "Visualizing the mechanical activation of Src", *Nature*, Vol. 434, No. 7036, pp. 1040–1045, 2005.

28. Ashkin, A., "Acceleration and trapping of particles by radiation pressure", *Physical review letters*, Vol. 24, No. 4, p. 156, 1970.

29. Ashkin, A., J. M. Dziedzic and T. Yamane, "Optical trapping and manipulation of single cells using infrared laser beams", *Nature*, Vol. 330, No. 6150, pp. 769–771, 1987.

30. Maragò, O. M., P. H. Jones, P. G. Gucciardi, G. Volpe and A. C. Ferrari, "Optical trapping and manipulation of nanostructures", *Nature nanotechnology*, Vol. 8, No. 11, p. 807, 2013.

31. Polimeno, P., A. Magazzu, M. A. Iatì, F. Patti, R. Saija, C. D. E. Boschi, M. G. Donato, P. G. Gucciardi, P. H. Jones, G. Volpe *et al.*, "Optical tweezers and their applications", *Journal of Quantitative Spectroscopy and Radiative Transfer*, Vol. 218, pp. 131–150, 2018.

32. Oberstrass, F. C., L. E. Fernandes and Z. Bryant, "Torque measurements reveal sequence-specific cooperative transitions in supercoiled DNA", *Proceedings of the National Academy of Sciences*, Vol. 109, No. 16, pp. 6106–6111, 2012.

33. Hu, S., L. Eberhard, J. Chen, J. C. Love, J. P. Butler, J. J. Fredberg, G. M. Whitesides and N. Wang, "Mechanical anisotropy of adherent cells probed by

a three-dimensional magnetic twisting device", *American Journal of Physiology-Cell Physiology*, Vol. 287, No. 5, pp. C1184–C1191, 2004.

34. Ozcelik, A., J. Rufo, F. Guo, Y. Gu, P. Li, J. Lata and T. J. Huang, "Acoustic tweezers for the life sciences", *Nature methods*, Vol. 15, No. 12, pp. 1021–1028, 2018.

35. Cheeke, J. D. N., *Fundamentals and applications of ultrasonic waves*, CRC press, 2016.

36. Lofts, G., *Jacaranda Physics 1: VCE Physics Units 1 & 2*, John wiley, 2004.

37. Kossoff, G., "Display techniques in ultrasound pulse echo investigations: a review", *Journal of Clinical Ultrasound*, Vol. 2, No. 1, pp. 61–72, 1974.

38. Shung, K. K., *Diagnostic ultrasound: Imaging and blood flow measurements*, CRC press, 2015.

39. Carovac, A., F. Smajlovic and D. Junuzovic, "Application of ultrasound in medicine", *Acta Informatica Medica*, Vol. 19, No. 3, p. 168, 2011.

40. Foster, F. S., C. J. Pavlin, K. A. Harasiewicz, D. A. Christopher and D. H. Turnbull, "Advances in ultrasound biomicroscopy", *Ultrasound in medicine & biology*, Vol. 26, No. 1, pp. 1–27, 2000.

41. Graham, K. C., L. A. Wirtzfeld, L. T. MacKenzie, C. O. Postenka, A. C. Groom, I. C. MacDonald, A. Fenster, J. C. Lacefield and A. F. Chambers, "Three-dimensional high-frequency ultrasound imaging for longitudinal evaluation of liver metastases in preclinical models", *Cancer Research*, Vol. 65, No. 12, pp. 5231–5237, 2005.

42. Goertz, D. E., L. Y. Joanne, R. S. Kerbel, P. N. Burns and F. S. Foster, "High-frequency Doppler ultrasound monitors the effects of antivascular therapy on tu-

mor blood flow", *Cancer research*, Vol. 62, No. 22, pp. 6371–6375, 2002.

43. Vlad, R., S. Brand, A. Giles, M. Kolios and G. Czarnota, "Quantitative ultrasound assessing tumor responses to radiotherapy in cancer mouse models", *Ultrasonic Imaging*, Vol. 29, pp. 255–256, 2008.

44. Czarnota, G., M. Kolios, J. Abraham, M. Portnoy, F. Ottensmeyer, J. Hunt and M. Sherar, "Ultrasound imaging of apoptosis: high-resolution non-invasive monitoring of programmed cell death in vitro, in situ and in vivo", *British journal of cancer*, Vol. 81, No. 3, pp. 520–527, 1999.

45. Oelze, M. L. and J. F. Zachary, "Examination of cancer in mouse models using high-frequency quantitative ultrasound", *Ultrasound in medicine & biology*, Vol. 32, No. 11, pp. 1639–1648, 2006.

46. Vlad, R. M., *Quantitative ultrasound characterization of responses to radiotherapy in vitro and in vivo*, Citeseer, 2009.

47. Kemmerer, J., G. Ghoshal and M. Oelze, "Quantitative ultrasound assessment of HIFU induced lesions in rodent liver", *2010 IEEE International Ultrasonics Symposium*, pp. 1396–1399, IEEE, 2010.

48. Oelze, M. L., W. D. O'Brien, J. P. Blue and J. F. Zachary, "Differentiation and characterization of rat mammary fibroadenomas and 4T1 mouse carcinomas using quantitative ultrasound imaging", *IEEE Transactions on medical imaging*, Vol. 23, No. 6, pp. 764–771, 2004.

49. Vlad, R. M., S. Brand, A. Giles, M. C. Kolios and G. J. Czarnota, "Quantitative ultrasound characterization of responses to radiotherapy in cancer mouse models", *Clinical cancer research*, Vol. 15, No. 6, pp. 2067–2075, 2009.

50. Bushberg, J. T. and J. M. Boone, *The essential physics of medical imaging*, Lippincott Williams & Wilkins, 2011.

51. Cobbold, R., "Foundations of biomedical ultrasound Oxford University Press", *USA, New York*, 2007.

52. Chan, V. and A. Perlas, "Basics of ultrasound imaging", *Atlas of ultrasound-guided procedures in interventional pain management*, pp. 13–19, Springer, 2011.

53. Dukhin, A. and P. Goetz, "Ultrasound for Characterizing Colloids: Particle Sizing, Zeta Potential", *Rheology*, Elsevier Chichester, UK, 2002.

54. Fay, J. A., *Introduction to fluid mechanics*, MIT press, 1994.

55. David, J. and N. Cheeke, "Fundamentals and applications of ultrasonic waves", *Physics Department Concordia University Montreal, Quebec, Canada*, 2002.

56. Auld, B., "Acoustic Fields and Waves in Solids, vol. One and Two", , 1990.

57. Mark, J. E. *et al.*, *Physical properties of polymers handbook*, Vol. 1076, Springer, 2007.

58. Adjadj, L. P., G. Storti and M. Morbidelli, "Ultrasound attenuation in polystyrene latexes", *Langmuir*, Vol. 19, No. 9, pp. 3953–3957, 2003.

59. Faran Jr, J. J., "Sound scattering by solid cylinders and spheres", *The Journal of the acoustical society of America*, Vol. 23, No. 4, pp. 405–418, 1951.

60. Insana, M. F., D. G. Brown, K. K. Shung *et al.*, "Acoustic scattering theory applied to soft biological tissues", *Ultrasonic scattering in biological tissues*, pp. 75–124, 1993.

61. Inoué, S., "Foundations of confocal scanned imaging in light microscopy", *Handbook of biological confocal microscopy*, pp. 1–19, Springer, 2006.

62. Sokolov, S., "The ultrasonic microscope", *Doklady Akademii Nauk SSSR*, Vol. 64,

pp. 333–335, 1949.

63. Lemons, R. and C. Quate, "Acoustic microscope—scanning version", *Applied Physics Letters*, Vol. 24, No. 4, pp. 163–165, 1974.

64. Maev, R. G., *Acoustic microscopy: Fundamentals and applications*, John Wiley & Sons, 2008.

65. Hoppe, M. and J. Bereiter-Hahn, "Applications of scanning acoustic microscopy-survey and new aspects", *IEEE transactions on sonics and ultrasonics*, Vol. 32, No. 2, pp. 289–301, 1985.

66. von Buttlar, M., E. Mohamed and W. Grill, "Signal processing for time-lapse cell imaging with vector-contrast scanning acoustic microscopy", *Acoustical Imaging*, pp. 135–142, Springer, 2011.

67. Ohkawai, H., S.-I. Nitta, M. Tanaka and F. Dunn, "In vivo measurement of thickness or of speed of sound in biological tissue structures", *IEEE transactions on sonics and ultrasonics*, Vol. 30, No. 4, pp. 231–237, 1983.

68. Briggs, A., "Acoustic microscopy-a summary", *Reports on Progress in Physics*, Vol. 55, No. 7, p. 851, 1992.

69. Gunawan, A. I., N. Hozumi, S. Yoshida, Y. Saijo, K. Kobayashi and S. Yamamoto, "Numerical analysis of ultrasound propagation and reflection intensity for biological acoustic impedance microscope", *Ultrasonics*, Vol. 61, pp. 79–87, 2015.

70. Kobayashi, K., S. Yoshida, Y. Saijo and N. Hozumi, "Acoustic impedance microscopy for biological tissue characterization", *Ultrasonics*, Vol. 54, No. 7, pp. 1922–1928, 2014.

71. Hozumi, N., A. Kimura, S. Terauchi, M. Nagao, S. Yoshida, K. Kobayashi and Y. Saijo, "Acoustic impedance micro-imaging for biological tissue using a focused

acoustic pulse with a frequency range up to 100 MHz", *IEEE Ultrasonics Symposium, 2005.*, Vol. 1, pp. 170–173, IEEE, 2005.

72. Youssef, S., *High Resolution Imaging and Digital Characterization of Skin Pathology By Scanning Acoustic Microscopy*, Master Thesis, University of Windsor, 2018.

73. Hozumi, N., R. Yamashita, C.-K. Lee, M. Nagao, K. Kobayashi, Y. Saijo, M. Tanaka, N. Tanaka and S. Ohtsuki, "Time–frequency analysis for pulse driven ultrasonic microscopy for biological tissue characterization", *Ultrasonics*, Vol. 42, No. 1-9, pp. 717–722, 2004.

74. Saijo, Y., H. Sasaki, T. Yambe, M. Tanaka, N. Hozumi, K. Kobayashi and N. Okada, "Speed of sound microscopy for biomedical applications", *IEEE Ultrasonics Symposium, 2005.*, Vol. 1, pp. 419–422, IEEE, 2005.

75. Saijo, Y., M. Tanaka, H. Okawai, H. Sasaki, S.-I. Nitta and F. Dunn, "Ultrasonic tissue characterization of infarcted myocardium by scanning acoustic microscopy", *Ultrasound in medicine & biology*, Vol. 23, No. 1, pp. 77–85, 1997.

76. Sherar, M. and F. Foster, "The design and fabrication of high frequency poly (vinylidene fluoride) transducers", *Ultrasonic imaging*, Vol. 11, No. 2, pp. 75–94, 1989.

77. Hunt, J. W., M. Arditi and F. S. Foster, "Ultrasound transducers for pulse-echo medical imaging", *IEEE Transactions on Biomedical Engineering*, , No. 8, pp. 453–481, 1983.

78. Shung, K. K. and M. Zippuro, "Ultrasonic transducers and arrays", *IEEE Engineering in Medicine and Biology Magazine*, Vol. 15, No. 6, pp. 20–30, 1996.

79. Ng, A. and J. Swanevelder, "Resolution in ultrasound imaging", *Continuing Education in Anaesthesia Critical Care & Pain*, Vol. 11, No. 5, pp. 186–192, 2011.

80. Li, J., C. R. Friedrich and R. S. Keynton, "Design and fabrication of a miniaturized, integrated, high-frequency acoustical lens–transducer system", *Journal of Micromechanics and Microengineering*, Vol. 12, No. 3, p. 219, 2002.

81. Frinking, P. J., A. Bouakaz, J. Kirkhorn, F. J. Ten Cate and N. De Jong, "Ultrasound contrast imaging: current and new potential methods", *Ultrasound in medicine & biology*, Vol. 26, No. 6, pp. 965–975, 2000.

82. Cosgrove, D., "Ultrasound contrast agents: an overview", *European journal of radiology*, Vol. 60, No. 3, pp. 324–330, 2006.

83. MAXWELL, J. C., "MAXWELL, James Clerk. A treatise on electricity and magnetism. Vol. I. Oxford: Clarenton Press Series, 1873. Preface, pV-XIV.", , 1873.

84. Ashkin, A., "Forces of a single-beam gradient laser trap on a dielectric sphere in the ray optics regime", *Biophysical journal*, Vol. 61, No. 2, pp. 569–582, 1992.

85. Harada, Y. and T. Asakura, "Radiation forces on a dielectric sphere in the Rayleigh scattering regime", *Optics communications*, Vol. 124, No. 5-6, pp. 529–541, 1996.

86. Tlusty, T., A. Meller and R. Bar-Ziv, "Optical gradient forces of strongly localized fields", *Physical review letters*, Vol. 81, No. 8, p. 1738, 1998.

87. Laing, R. W., A. P. Warrington, J. Graham, J. Britton, F. Hines and M. Brada, "Efficacy and toxicity of fractionated stereotactic radiotherapy in the treatment of recurrent gliomas (phase I/II study)", *Radiotherapy and Oncology*, Vol. 27, No. 1, pp. 22–29, 1993.

88. Koong, A. C., Q. T. Le, A. Ho, B. Fong, G. Fisher, C. Cho, J. Ford, J. Poen, I. C. Gibbs, V. K. Mehta *et al.*, "Phase I study of stereotactic radiosurgery in patients with locally advanced pancreatic cancer", *International Journal of Radiation Oncology* Biology* Physics*, Vol. 58, No. 4, pp. 1017–1021, 2004.

89. Tannock, I. F., *The basic science of oncology*, McGraw-Hill, 2005.

90. Corre, I., C. Niaudet and F. Paris, "Plasma membrane signaling induced by ionizing radiation", *Mutation Research/Reviews in Mutation Research*, Vol. 704, No. 1-3, pp. 61–67, 2010.

91. Murphy, E. and D. A. Eisner, "Regulation of intracellular and mitochondrial sodium in health and disease", *Circulation research*, Vol. 104, No. 3, pp. 292–303, 2009.

92. Rose, A. M. and R. Valdes, "Understanding the sodium pump and its relevance to disease.", *Clinical Chemistry*, Vol. 40, No. 9, pp. 1674–1685, 1994.

93. Skou, J. C. and M. Esmann, "The na, k-atpase", *Journal of bioenergetics and biomembranes*, Vol. 24, No. 3, pp. 249–261, 1992.

94. Minta, A. and R. Y. Tsien, "Fluorescent indicators for cytosolic sodium.", *Journal of Biological Chemistry*, Vol. 264, No. 32, pp. 19449–19457, 1989.

95. Garcia, R. A., C. P. Vanelli, O. d. S. Pereira Junior and J. O. d. A. Corrêa, "Comparative analysis for strength serum sodium and potassium in three different methods: Flame photometry, ion-selective electrode (ISE) and colorimetric enzymatic", *Journal of Clinical Laboratory Analysis*, Vol. 32, No. 9, p. e22594, 2018.

96. Amorino, G. P. and M. H. Fox, "Intracellular Na+ measurements using sodium green tetraacetate with flow cytometry", *Cytometry: The Journal of the International Society for Analytical Cytology*, Vol. 21, No. 3, pp. 248–256, 1995.

97. Hansen, L. L., J. Rasmussen, E. Friche and J. W. Jaroszewski, "Method for determination of intracellular sodium in perfused cancer cells by 23Na nuclear magnetic resonance spectroscopy", *Analytical biochemistry*, Vol. 214, No. 2, pp. 506–510, 1993.

98. van der Veen, J., P. Van Gelderen, J. Creyghton and W. Bovee, "Diffusion in red blood cell suspensions: separation of the intracellular and extracellular NMR sodium signal", *Magnetic resonance in medicine*, Vol. 29, No. 4, pp. 571–574, 1993.

99. Madelin, G. and R. R. Regatte, "Biomedical applications of sodium MRI in vivo", *Journal of Magnetic Resonance Imaging*, Vol. 38, No. 3, pp. 511–529, 2013.

100. Briggs, A., *An introduction to scanning acoustic microscopy*, 1985.

101. Raum, K., K. Kempf, H. J. Hein, J. Schubert and P. Maurer, "Preservation of microelastic properties of dentin and tooth enamel in vitro—a scanning acoustic microscopy study", *dental materials*, Vol. 23, No. 10, pp. 1221–1228, 2007.

102. Irie, S., K. Inoue, K. Yoshida, J. Mamou, K. Kobayashi, H. Maruyama and T. Yamaguchi, "Speed of sound in diseased liver observed by scanning acoustic microscopy with 80 MHz and 250 MHz", *The Journal of the Acoustical Society of America*, Vol. 139, No. 1, pp. 512–519, 2016.

103. Ito, K., K. Yoshida, H. Maruyama, J. Mamou and T. Yamaguchi, "Acoustic impedance analysis with high-frequency ultrasound for identification of fatty acid species in the liver", *Ultrasound in medicine & biology*, Vol. 43, No. 3, pp. 700–711, 2017.

104. Saijo, Y., M. Tanaka, H. Okawai and F. Dunn, "The ultrasonic properties of gastric cancer tissues obtained with a scanning acoustic microscope system", *Ultrasound in medicine & biology*, Vol. 17, No. 7, pp. 709–714, 1991.

105. Kundu, T., J. Bereiter-Hahn and I. Karl, "Cell property determination from the acoustic microscope generated voltage versus frequency curves", *Biophysical journal*, Vol. 78, No. 5, pp. 2270–2279, 2000.

106. Zhao, X., R. Akhtar, N. Nijenhuis, S. J. Wilkinson, L. Murphy, C. Ballestrem,

M. J. Sherratt, R. E. Watson and B. Derby, "Multi-layer phase analysis: quantifying the elastic properties of soft tissues and live cells with ultra-high-frequency scanning acoustic microscopy", *IEEE transactions on ultrasonics, ferroelectrics, and frequency control*, Vol. 59, No. 4, pp. 610–620, 2012.

107. Miura, K., H. Nasu and S. Yamamoto, "Scanning acoustic microscopy for characterization of neoplastic and inflammatory lesions of lymph nodes", *Scientific reports*, Vol. 3, p. 1255, 2013.

108. Miura, K. and S. Yamamoto, "A scanning acoustic microscope discriminates cancer cells in fluid", *Scientific reports*, Vol. 5, p. 15243, 2015.

109. Soon, T. T. K., T. W. Chean, H. Yamada, K. Takahashi, N. Hozumi, K. Kobayashi and S. Yoshida, "Effects of anticancer drugs on glia–glioma brain tumor model characterized by acoustic impedance microscopy", *Japanese Journal of Applied Physics*, Vol. 56, No. 7S1, p. 07JF15, 2017.

110. Cook, J. R., R. R. Bouchard and S. Y. Emelianov, "Tissue-mimicking phantoms for photoacoustic and ultrasonic imaging", *Biomedical optics express*, Vol. 2, No. 11, pp. 3193–3206, 2011.

111. Lee, S., H. Lee, I. Lee and C. Tseng, "Ink diffusion in water", *European journal of physics*, Vol. 25, No. 2, p. 331, 2004.

112. Crank, J. *et al.*, *The mathematics of diffusion*, Oxford university press, 1979.

113. Hamamura, M. J., L. T. Muftuler, O. Birgul and O. Nalcioglu, "Measurement of ion diffusion using magnetic resonance electrical impedance tomography", *Physics in Medicine & Biology*, Vol. 51, No. 11, p. 2753, 2006.

114. Barr, R. J., G. M. White, J. P. Jones, L. B. Shaw and P. A. Ross, "Scanning acoustic microscopy of neoplastic and inflammatory cutaneous tissue specimens", *Journal of investigative dermatology*, Vol. 96, No. 1, pp. 38–42, 1991.

115. Kobayashi, K., S. Yoshida, Y. Saijo and N. Hozumi, "Acoustic impedance microscopy for biological tissue characterization", *Ultrasonics*, Vol. 54, No. 7, pp. 1922–1928, 2014.

116. Zell, K., J. Sperl, M. Vogel, R. Niessner and C. Haisch, "Acoustical properties of selected tissue phantom materials for ultrasound imaging", *Physics in Medicine & Biology*, Vol. 52, No. 20, p. N475, 2007.

117. Cameron, I., N. Smith, T. Pool and R. Sparks, "Intracellular concentration of sodium and other elements as related to mitogenesis and oncogenesis in vivo", *Cancer research*, Vol. 40, No. 5, pp. 1493–1500, 1980.

118. Ouwerkerk, R., K. B. Bleich, J. S. Gillen, M. G. Pomper and P. A. Bottomley, "Tissue sodium concentration in human brain tumors as measured with 23Na MR imaging", *Radiology*, Vol. 227, No. 2, pp. 529–537, 2003.

119. Kline, R. P., E. X. Wu, D. P. Petrylak, M. Szabolcs, P. O. Alderson, M. L. Weisfeldt, P. Cannon and J. Katz, "Rapid in vivo monitoring of chemotherapeutic response using weighted sodium magnetic resonance imaging", *Clinical cancer research*, Vol. 6, No. 6, pp. 2146–2156, 2000.

120. Babsky, A. M., H. Zhang, S. K. Hekmatyar, G. D. Hutchins and N. Bansal, "Monitoring chemotherapeutic response in RIF-1 tumors by single-quantum and triple-quantum-filtered 23Na MRI, 1H diffusion-weighted MRI and PET imaging", *Magnetic resonance imaging*, Vol. 25, No. 7, pp. 1015–1023, 2007.

121. Schepkin, V. D., B. D. Ross, T. L. Chenevert, A. Rehemtulla, S. Sharma, M. Kumar and J. Stojanovska, "Sodium magnetic resonance imaging of chemotherapeutic response in a rat glioma", *Magnetic Resonance in Medicine: An Official Journal of the International Society for Magnetic Resonance in Medicine*, Vol. 53, No. 1, pp. 85–92, 2005.

122. Fanelli, D., A. McKane, G. Pompili, B. Tiribilli, M. Vassalli and T. Biancalani, "Diffusion of two molecular species in a crowded environment: theory and experiments", *Physical biology*, Vol. 10, No. 4, p. 045008, 2013.

123. Bhatnagar, D., D. Joshi, A. Kumar and C. Jain, "Direct acoustic impedance measurements of dimethyl sulphoxide with benzene, carbon tetrachloride and methanol liquid mixtures", , 2010.

124. Muhr, A. H. and J. M. Blanshard, "Diffusion in gels", *Polymer*, Vol. 23, No. 7, pp. 1012–1026, 1982.

125. Schantz, E. J. and M. A. Lauffer, "Diffusion measurements in agar gel", *Biochemistry*, Vol. 1, No. 4, pp. 658–663, 1962.

126. Shibuya, K., C. D. Mathers, C. Boschi-Pinto, A. D. Lopez and C. J. Murray, "Global and regional estimates of cancer mortality and incidence by site: II. Results for the global burden of disease 2000", *BMC cancer*, Vol. 2, No. 1, p. 37, 2002.

127. Moore, S., M. C. Burke, M. R. Fenlon and A. Banerjee, "The role of the general dental practitioner in managing the oral care of head and neck oncology patients", *Dental update*, Vol. 39, No. 10, pp. 694–702, 2012.

128. Jham, B. C. and A. R. da Silva Freire, "Oral complications of radiotherapy in the head and neck", *Brazilian Journal of Otorhinolaryngology*, Vol. 72, No. 5, pp. 704–708, 2006.

129. Lieshout, H. and C. Bots, "The effect of radiotherapy on dental hard tissue—a systematic review", *Clinical oral investigations*, Vol. 18, No. 1, pp. 17–24, 2014.

130. Aguiar, G. P., B. C. Jham, C. S. Magalhães, L. G. Sensi and A. R. Freire, "A review of the biological and clinical aspects of radiation caries", *J Contemp Dent Pract*, Vol. 10, No. 4, pp. 83–89, 2009.

131. Kielbassa, A., E. Hellwig and H. Meyer-Lueckel, "Effects of irradiation on in situ remineralization of human and bovine enamel demineralized in vitro", *Caries research*, Vol. 40, No. 2, pp. 130–135, 2006.

132. Silva, A. R. S., F. A. Alves, S. B. Berger, M. Giannini, M. F. Goes and M. A. Lopes, "Radiation-related caries and early restoration failure in head and neck cancer patients. A polarized light microscopy and scanning electron microscopy study", *Supportive care in cancer*, Vol. 18, No. 1, p. 83, 2010.

133. Hegde, M. N., N. D. Hegde, G. Sanjeev, G. Priya, S. Attavar *et al.*, "Techniques to analyze the effects of radiation therapy on enamel and dentin-a review", *Journal of Health and Allied Sciences NU*, Vol. 6, No. 04, pp. 71–78, 2016.

134. Markitziu, A., I. Gedalia, J. Rajstein, R. Grajover, O. Yarshanski and Z. Weshler, "In vitro irradiation effects on hardness and solubility of human enamel and dentin pretreated with fluoride.", *Clinical preventive dentistry*, Vol. 8, No. 4, pp. 4–7, 1986.

135. Pioch, T., D. Golfels and H. J. Staehle, "An experimental study of the stability of irradiated teeth in the region of the dentinoenamel junction", *Dental Traumatology*, Vol. 8, No. 6, pp. 241–244, 1992.

136. Chun, K. J., H. Choi and J. Lee, "Comparison of mechanical property and role between enamel and dentin in the human teeth", *Journal of dental biomechanics*, Vol. 5, 2014.

137. Halgaš, R., J. Dusza, J. Kaiferova, L. Kovacsova and N. Markovska, "Nanoindentation testing of human enamel and dentin", *Ceramics–Silikáty*, Vol. 57, No. 2, pp. 92–99, 2013.

138. Azinović, Z., J. Keros, D. Buković and A. Azinović, "SEM analysis of tooth enamel", *Collegium antropologicum*, Vol. 27, No. 1, pp. 381–386, 2003.

139. Marzuki, A. and S. Masudi, "Confocal laser scanning microscopy study of dentinal tubules in dental caries stained with alizarin red", *Archives of Orofacial Sciences*, Vol. 3, No. 1, pp. 2–6, 2008.

140. Lee, D. P., L. C. Espejo-Trung, M. R. L. Simionato, F. de Abreu Alves, M. D. Novelli and M. A. A. de Cerqueira Luz, "The effects of ionizing radiation on the development of human caries lesions in vitro", *Clinical and Laboratorial Research in Dentistry*, Vol. 20, No. 1, pp. 46–53, 2014.

141. Poyton, H., "The effects of radiation on teeth", *Oral Surgery, Oral Medicine, Oral Pathology*, Vol. 26, No. 5, pp. 639–646, 1968.

142. Fränzel, W., R. Gerlach, H.-J. Hein and H.-G. Schaller, "Effect of tumor therapeutic irradiation on the mechanical properties of teeth tissue", *Zeitschrift für Medizinische Physik*, Vol. 16, No. 2, pp. 148–154, 2006.

143. Knychalska-Karwan, Z., R. Pawlicki and T. Karwan, "Structural and microanalytical changes in dentition after radiotherapy applied in cases of tumour in the oral cavity region.", *Folia histochemica et cytobiologica*, Vol. 26, No. 1, pp. 25–32, 1988.

144. Lenhard, M., T. Pioch, V. Rudat and H. Staehle, "Fracture toughness of human enamel after irradiation", *J Dent Res*, Vol. 73, p. 978, 1994.

145. Gardner, T., J. Elliott, Z. Sklar and G. Briggs, "Acoustic microscope study of the elastic properties of fluorapatite and hydroxyapatite, tooth enamel and bone", *Journal of biomechanics*, Vol. 25, No. 11, pp. 1265–1277, 1992.

146. Hasegawa, K., C. Turner, R. R. Recker, E. Wu and D. Burr, "Elastic properties of osteoporotic bone measured by scanning acoustic microscopy", *Bone*, Vol. 16, No. 1, pp. 85–90, 1995.

147. Culjat, M., R. S. Singh, D. Yoon and E. R. Brown, "Imaging of human tooth

enamel using ultrasound", *IEEE transactions on medical imaging*, Vol. 22, No. 4, pp. 526–529, 2003.

148. Demirkan, I., G. Yaprak, C. Ceylan, E. Algul, M. Parlak, M. B. Unlu and B. Bilen, "Acoustic impedance measurement of radiotherapy-induced effect on the human tooth by 320 MHz scanning acoustic microscopy", *Imaging, Manipulation, and Analysis of Biomolecules, Cells, and Tissues XVII*, Vol. 10881, p. 108811S, International Society for Optics and Photonics, 2019.

149. Andreo, P., M. S. Huq, M. Westermark, H. Song, A. Tilikidis, L. DeWerd and K. Shortt, "Protocols for the dosimetry of high-energy photon and electron beams: a comparison of the IAEA TRS-398 and previous international Codes of Practice", *Physics in Medicine & Biology*, Vol. 47, No. 17, p. 3033, 2002.

150. Al-Nawas, B., K. Grötz, E. Rose, H. Duschner, P. Kann and W. Wagner, "Using ultrasound transmission velocity to analyse the mechanical properties of teeth after in vitro, in situ, and in vivo irradiation", *Clinical oral investigations*, Vol. 4, No. 3, pp. 168–172, 2000.

151. Gonçalves, L. M. N., R. G. Palma-Dibb, F. W. G. Paula-Silva, H. F. de Oliveira, P. Nelson-Filho, L. A. B. da Silva and A. M. de Queiroz, "Radiation therapy alters microhardness and microstructure of enamel and dentin of permanent human teeth", *Journal of dentistry*, Vol. 42, No. 8, pp. 986–992, 2014.

152. de Siqueira Mellara, T., R. G. Palma-Dibb, H. F. de Oliveira, F. W. G. Paula-Silva, P. Nelson-Filho, R. A. B. da Silva, L. A. B. da Silva and A. M. de Queiroz, "The effect of radiation therapy on the mechanical and morphological properties of the enamel and dentin of deciduous teeth—an in vitro study", *Radiation Oncology*, Vol. 9, No. 1, p. 30, 2014.

153. Mjör, I. A., "Dentin permeability: the basis for understanding pulp reactions and adhesive technology", *Brazilian dental journal*, Vol. 20, No. 1, pp. 3–16, 2009.

154. Cole, T. and A. H. Silver, "Production of hydrogen atoms in teeth by X-irradiation", *Nature*, Vol. 200, No. 4907, pp. 700–701, 1963.

155. Umegaki, K., A. Sugisawa, S. J. Shin, K. Yamada and M. Sano, "Different onsets of oxidative damage to DNA and lipids in bone marrow and liver in rats given total body irradiation", *Free Radical Biology and Medicine*, Vol. 31, No. 9, pp. 1066–1074, 2001.

156. Georgakilas, A. G., "Processing of DNA damage clusters in human cells: current status of knowledge", *Molecular BioSystems*, Vol. 4, No. 1, pp. 30–35, 2008.

157. Georgakilas, A. G., P. O'Neill and R. D. Stewart, "Induction and repair of clustered DNA lesions: what do we know so far?", *Radiation research*, Vol. 180, No. 1, pp. 100–109, 2013.

158. Wang, Y., L. Liu, S. K. Pazhanisamy, H. Li, A. Meng and D. Zhou, "Total body irradiation causes residual bone marrow injury by induction of persistent oxidative stress in murine hematopoietic stem cells", *Free Radical Biology and Medicine*, Vol. 48, No. 2, pp. 348–356, 2010.

159. Nomura, T., T. Hongyo, H. Nakajima, L. Y. Li, M. Syaifudin, S. Adachi, H. Ryo, R. Baskar, K. Fukuda, Y. Oka *et al.*, "Differential radiation sensitivity to morphological, functional and molecular changes of human thyroid tissues and bone marrow cells maintained in SCID mice", *Mutation Research/Genetic Toxicology and Environmental Mutagenesis*, Vol. 657, No. 1, pp. 68–76, 2008.

160. Gavara, N. and R. S. Chadwick, "Determination of the elastic moduli of thin samples and adherent cells using conical atomic force microscope tips", *Nature nanotechnology*, Vol. 7, No. 11, p. 733, 2012.

161. Coates, P. J., S. A. Lorimore and E. G. Wright, "Damaging and protective cell signalling in the untargeted effects of ionizing radiation", *Mutation Re-*

search/Fundamental and Molecular Mechanisms of Mutagenesis, Vol. 568, No. 1, pp. 5–20, 2004.

162. Liumbruno, G., F. Bennardello, A. Lattanzio, P. Piccoli and G. Rossetti, "Recommendations for the transfusion of red blood cells", *Blood Transfusion*, Vol. 7, No. 1, p. 49, 2009.

163. Brugnara, C. and W. Churchill, "Effect of irradiation on red cell cation content and transport", *Transfusion*, Vol. 32, No. 3, pp. 246–252, 1992.

164. Dinning, G., R. Doughty, M. Reid and H. Lloyd, "Potassium concentrations in irradiated blood.", *BMJ: British Medical Journal*, Vol. 303, No. 6810, p. 1110, 1991.

165. Chapman, J., R. Finney, K. Forman, P. Kelsey, S. Knowles, J. Napier, P. Phillips, R. Mitchell, M. Murphy, A. Waters *et al.*, "Guidelines on gamma irradiation of blood components for the prevention of transfusion-associated graft-versus-host disease", *Transfusion Medicine*, Vol. 6, No. 3, pp. 261–271, 1996.

166. Rivet, C., A. Baxter and G. Rock, "Potassium levels in irradiated blood", *Transfusion*, Vol. 29, No. 2, pp. 185–185, 1989.

167. Agarwal, P., V. Ray, N. Choudhury and R. Chaudhary, "Effect of pre-storage gamma irradiation on red blood cells", *Indian Journal of Medical Research*, Vol. 122, No. 5, p. 385, 2005.

168. Jin, M., H. Jeon, H. J. Jung, B. Kim, S. S. Shin, J. J. Choi, J. K. Lee, C.-Y. Kang and S. Kim, "Enhancement of repopulation and hematopoiesis of bone marrow cells in irradiated mice by oral administration of PG101, a water-soluble extract from Lentinus lepideus", *Experimental biology and medicine*, Vol. 228, No. 6, pp. 759–766, 2003.

169. Li, W., G. Wang, J. Cui, L. Xue and L. Cai, "Low-dose radiation (LDR) induces

hematopoietic hormesis: LDR-induced mobilization of hematopoietic progenitor cells into peripheral blood circulation", *Experimental hematology*, Vol. 32, No. 11, pp. 1088–1096, 2004.

170. Peslak, S. A., J. Wenger, J. C. Bemis, P. D. Kingsley, J. M. Frame, A. D. Koniski, Y. Chen, J. P. Williams, K. E. McGrath, S. D. Dertinger *et al.*, "Sublethal radiation injury uncovers a functional transition during erythroid maturation", *Experimental hematology*, Vol. 39, No. 4, pp. 434–445, 2011.

171. Moroni, M., T. B. Elliott, N. E. Deutz, C. H. Olsen, R. Owens, C. Christensen, E. D. Lombardini and M. H. Whitnall, "Accelerated hematopoietic syndrome after radiation doses bridging hematopoietic (H-ARS) and gastrointestinal (GI-ARS) acute radiation syndrome: early hematological changes and systemic inflammatory response syndrome in minipig", *International journal of radiation biology*, Vol. 90, No. 5, pp. 363–372, 2014.

172. Xu, W., R. Mezencev, B. Kim, L. Wang, J. McDonald and T. Sulchek, "Cell stiffness is a biomarker of the metastatic potential of ovarian cancer cells", *PloS one*, Vol. 7, No. 10, 2012.

173. Tomaiuolo, G., "Biomechanical properties of red blood cells in health and disease towards microfluidics", *Biomicrofluidics*, Vol. 8, No. 5, p. 051501, 2014.

174. Weng, H., X. Guo, J. Papoin, J. Wang, R. Coppel, N. Mohandas and X. An, "Interaction of Plasmodium falciparum knob-associated histidine-rich protein (KAHRP) with erythrocyte ankyrin R is required for its attachment to the erythrocyte membrane", *Biochimica et Biophysica Acta (BBA)-Biomembranes*, Vol. 1838, No. 1, pp. 185–192, 2014.

175. Buys, A. V., M.-J. Van Rooy, P. Soma, D. Van Papendorp, B. Lipinski and E. Pretorius, "Changes in red blood cell membrane structure in type 2 diabetes: a scanning electron and atomic force microscopy study", *Cardiovascular diabetol-*

ogy, Vol. 12, No. 1, p. 25, 2013.

176. Maciaszek, J. L. and G. Lykotrafitis, "Sickle cell trait human erythrocytes are significantly stiffer than normal", *Journal of biomechanics*, Vol. 44, No. 4, pp. 657–661, 2011.

177. An, X. and N. Mohandas, "Red cell membrane and malaria", *Transfusion clinique et biologique*, Vol. 17, No. 3, pp. 197–199, 2010.

178. Katira, P., M. H. Zaman and R. T. Bonnecaze, "How changes in cell mechanical properties induce cancerous behavior", *Physical review letters*, Vol. 108, No. 2, p. 028103, 2012.

179. Park, H. J., R. J. Griffin, S. Hui, S. H. Levitt and C. W. Song, "Radiation-induced vascular damage in tumors: implications of vascular damage in ablative hypofractionated radiotherapy (SBRT and SRS)", *Radiation research*, Vol. 177, No. 3, pp. 311–327, 2012.

180. Garaj-Vrhovac, V., G. Gajski, S. Pažanin, A. Šarolić, A.-M. Domijan, D. Flajs and M. Peraica, "Assessment of cytogenetic damage and oxidative stress in personnel occupationally exposed to the pulsed microwave radiation of marine radar equipment", *International Journal of hygiene and environmental health*, Vol. 214, No. 1, pp. 59–65, 2011.

181. Lara, P. C., J. J. López-Peñalver, V. de Araújo Farias, M. C. Ruiz-Ruiz, F. J. Oliver and J. M. R. de Almodóvar, "Direct and bystander radiation effects: A biophysical model and clinical perspectives", *Cancer letters*, Vol. 356, No. 1, pp. 5–16, 2015.

182. Felder, S. and E. L. Elson, "Mechanics of fibroblast locomotion: quantitative analysis of forces and motions at the leading lamellas of fibroblasts.", *The Journal of cell biology*, Vol. 111, No. 6, pp. 2513–2526, 1990.

183. Daily, B., E. L. Elson and G. I. Zahalak, "Cell poking. Determination of the elastic area compressibility modulus of the erythrocyte membrane", *Biophysical journal*, Vol. 45, No. 4, pp. 671–682, 1984.

184. Radmacher, M., M. Fritz, C. M. Kacher, J. P. Cleveland and P. K. Hansma, "Measuring the viscoelastic properties of human platelets with the atomic force microscope", , 1996.

185. Dao, M., C. T. Lim and S. Suresh, "Mechanics of the human red blood cell deformed by optical tweezers", *Journal of the Mechanics and Physics of Solids*, Vol. 51, No. 11-12, pp. 2259–2280, 2003.

186. Chen, J., B. Fabry, E. L. Schiffrin and N. Wang, "Twisting integrin receptors increases endothelin-1 gene expression in endothelial cells", *American Journal of Physiology-Cell Physiology*, Vol. 280, No. 6, pp. C1475–C1484, 2001.

187. MacKay, J. L. and S. Kumar, "Measuring the elastic properties of living cells with atomic force microscopy indentation", *Cell Imaging Techniques*, pp. 313–329, Springer, 2012.

188. Liao, G.-B., P. B. Bareil, Y. Sheng and A. Chiou, "One-dimensional jumping optical tweezers for optical stretching of bi-concave human red blood cells", *Optics Express*, Vol. 16, No. 3, pp. 1996–2004, 2008.

189. Henon, S., G. Lenormand, A. Richert and F. Gallet, "A new determination of the shear modulus of the human erythrocyte membrane using optical tweezers", *Biophysical journal*, Vol. 76, No. 2, pp. 1145–1151, 1999.

190. Rancourt-Grenier, S., M.-T. Wei, J.-J. Bai, A. Chiou, P. P. Bareil, P.-L. Duval and Y. Sheng, "Dynamic deformation of red blood cell in dual-trap optical tweezers", *Optics express*, Vol. 18, No. 10, pp. 10462–10472, 2010.

191. Agrawal, R., T. Smart, J. Nobre-Cardoso, C. Richards, R. Bhatnagar, A. Tufail,

D. Shima, P. H. Jones and C. Pavesio, "Assessment of red blood cell deformability in type 2 diabetes mellitus and diabetic retinopathy by dual optical tweezers stretching technique", *Scientific reports*, Vol. 6, p. 15873, 2016.

192. Zhang, Z. W. and B. Neu, "Role of macromolecular depletion in red blood cell adhesion", *Biophysical journal*, Vol. 97, No. 4, pp. 1031–1037, 2009.

193. De Luca, A. C., G. Rusciano, R. Ciancia, V. Martinelli, G. Pesce, B. Rotoli, L. Selvaggi and A. Sasso, "Spectroscopical and mechanical characterization of normal and thalassemic red blood cells by Raman tweezers", *Optics express*, Vol. 16, No. 11, pp. 7943–7957, 2008.

194. Heinrich, V., K. Ritchie, N. Mohandas and E. Evans, "Elastic thickness compressibilty of the red cell membrane", *Biophysical Journal*, Vol. 81, No. 3, pp. 1452–1463, 2001.

195. Švelc, T. and S. Svetina, "Stress-free state of the red blood cell membrane and the deformation of its skeleton", *Cellular & molecular biology letters*, Vol. 17, No. 2, pp. 217–227, 2012.

196. Haghparast, S. M. A., T. Kihara, Y. Shimizu, S. Yuba and J. Miyake, "Actin-based biomechanical features of suspended normal and cancer cells", *Journal of bioscience and bioengineering*, Vol. 116, No. 3, pp. 380–385, 2013.

197. Haimovitz-Friedman, A., C.-C. Kan, D. Ehleiter, R. S. Persaud, M. Mcloughlin, Z. Fuks and R. N. Kolesnick, "Ionizing radiation acts on cellular membranes to generate ceramide and initiate apoptosis.", *The Journal of experimental medicine*, Vol. 180, No. 2, pp. 525–535, 1994.

198. Zhang, B., B. Liu, H. Zhang and J. Wang, "Erythrocyte stiffness during morphological remodeling induced by carbon ion radiation", *PLoS One*, Vol. 9, No. 11, 2014.

199. Spyratou, E., M. Dilvoi, G. Patatoukas, K. Platoni, M. Makropoulou and E. P. Efstathopoulos, "Probing the effects of ionizing radiation on young's modulus of human erythrocytes cytoskeleton using atomic force microscopy", *Journal of medical physics*, Vol. 44, No. 2, p. 113, 2019.

200. Sanzari, J. K., X. S. Wan, G. S. Krigsfeld, A. J. Wroe, D. S. Gridley and A. R. Kennedy, "The effects of gamma and proton radiation exposure on hematopoietic cell counts in the ferret model", *Gravitational and space research: publication of the American Society for Gravitational and Space Research*, Vol. 1, No. 1, p. 79, 2013.

201. Huisjes, R., A. Bogdanova, W. W. van Solinge, R. M. Schiffelers, L. Kaestner and R. Van Wijk, "Squeezing for life–properties of red blood cell deformability", *Frontiers in physiology*, Vol. 9, p. 656, 2018.